

EXAMINATION OF TISSUE MICROSTRUCTURE, CONTRAST ENHANCEMENT AND
NEURAL ACTIVITY IN THE BRAIN SLICE MODEL USING MAGNETIC RESONANCE
MICROSCOPY

By

JEREMY JOSEPH FLINT

A DISSERTATION PRESENTED TO THE GRADUATE SCHOOL
OF THE UNIVERSITY OF FLORIDA IN PARTIAL FULFILLMENT
OF THE REQUIREMENTS FOR THE DEGREE OF
DOCTOR OF PHILOSOPHY

UNIVERSITY OF FLORIDA

2009

© 2009 Jeremy Joseph Flint

To my Mom, without whose boundless love and sacrifice this would not have been possible

ACKNOWLEDGMENTS

I would like to start by thanking my Ph.D. advisor Dr. Stephen Blackband for allowing me to be a part of his laboratory. He is as generous and understanding a person as I have ever met, and I feel tremendously lucky and privileged to have worked for him. I would like to thank Dr. Brian Pike and Dr. Erik Johnson for teaching me everything I know about the practical application of biological science. Their stewardship through my undergraduate work was responsible for my introduction to research and the skills they taught are still helping me today. I would like to thank Dr. John Forder for our discussions related to iron sources in tissues and for help in conceptualizing our latest microperfusion rig design. He has been an outstanding mentor and has offered me advice on everything from engineering to my trigger pull. I would like to thank Dr. Michael King for letting me borrow both his equipment and his seemingly limitless knowledge of histological science. I would like to thank Dr. Glenn Walter for his efforts spent teaching me about MR scan analysis. The last mentor I would like to thank is Dr. Ioannis Constantinidis for his help and counsel during my initial forays into MR imaging. We were all saddened by his passing and although I regret not being able to thank him personally, he is certainly no less deserving of my gratitude.

I would like to thank all of the former postdocs I worked with in Dr. Blackband's lab—Drs. Timothy Shepherd, Jonathan Bui, Peter Thelwall, Samuel Grant, and Kyle Padgett. They were responsible for teaching me everything I know about operating an imaging spectrometer which is itself a testament to their commitment and patience. The members of AMRIS' support staff including Barbara Beck, Daniel Plant, James Rocca, Kelly Jenkins, and Xeve Silver also deserve my thanks for their tireless work keeping the research equipment in order and the facility running smoothly. I would like to offer a special thanks to Dr. Melvin Clark for his assistance in calculating the power output of numerous RF amplifiers in the AMRIS facility. His

troubleshooting skills were invaluable during testing of the prototype microcoils. I would like to thank Dr. Brian Hansen for his collaboration on the slice activity experiments and help with designing prototype versions of the tissue-retention apparatus employed in our MRM studies. He also deserves thanks for performing our MATLAB-based DTI and DTT analysis. Also, I would like to offer a special thanks to Dr. Hansen's mentor—Dr. Peter Vestergaard-Poulsen—for his past and continuing support of my research as well as his facilitation of our labs collaborative efforts. They have been fruitful for me both professionally and personally. I would like to thank my fellow graduate student Choong-Heon Lee for his company during many long, coffee-fueled imaging sessions. I would like to thank Dr. Gerry Shaw for discussions relating to cell sizes in different organisms as well as alerting me to the availability of porcine and bovine tissues from UF Animal Processing. I would like to thank Drs. Charles Massin, Daniel Schmidig, and Michael Fey for their efforts designing and fabricating the microsurface coils used in our experiments. I would like to thank Dr. Thomas Mareci for providing the spherical coordinates for the 21-direction tensor protocol. Also, I would like to thank Drs. Steven Roper and Huan Xin for their helpful discussions relating to the slice activity study.

From my family, I would like to thank my mother Franca Flint and my wife Sara Flint. They are both very supportive and loving people who have been with me through good times and bad, but never stopped believing in me.

Lastly, I would like to thank the CFIN, NHMFL, NCRR, and the UF McKnight Brain Institute for financial and institutional support provided throughout the tenure of my graduate work.

TABLE OF CONTENTS

	<u>page</u>
ACKNOWLEDGMENTS	4
LIST OF TABLES	10
LIST OF FIGURES	11
ABSTRACT	15
CHAPTER	
1 BACKGROUND AND SIGNIFICANCE.....	17
Introduction.....	17
Magnetic Resonance Microscopy of Excised Tissue: Microcoils and the Slice Model.....	18
Diffusion-Weighted Magnetic Resonance Imaging	20
Diffusion Tensor Imaging and Tractography	22
Contrast Agents	24
2 PRELIMINARY MAGNETIC RESONANCE MICROSCOPY STUDIES OF NEURAL STRUCTURE IN THE CENTRAL NERVOUS SYSTEMS OF RATS AND MICE	27
Introduction.....	27
Methods	28
Prototype Microsurface Coil Characterization.....	28
Calculation of Diffusion-Limited and Bandwidth-Limited Resolution	28
Imaging of Fixed Tissue Slices: Preliminary Data.....	29
Tissue Histology: Preliminary Data	31
Results.....	31
Prototype Microsurface Coil Characterization.....	31
Calculation of Diffusion-Limited and Bandwidth-Limited Resolution	31
Imaging of Fixed Tissue Slices: Preliminary Data.....	32
Tissue Histology: Preliminary Data	32
Discussion.....	33
Coil Characterization.....	33
Imaging of Fixed Tissue Slices: Preliminary Data.....	34
Tissue Histology: Preliminary Data	36
3 MAGNETIC RESONANCE MICROSCOPY OF SINGLE MAMALIAN NEURONS AND TRACTOGRAPHY OF INDIVIDUAL AXON BUNDLES	46
Introduction.....	46
Methods	49
Alterations to Histology and MR Protocols	49

Transcardial Perfusion Fixation Protocol.....	49
Staining for Iron Deposition in Immersion and Perfusion Fixed Mouse Striatum.....	50
MRM of Laminar Cell Layers in the Rat Hippocampus	51
Calculation of Diffusion-Limited and Bandwidth-Limited Resolution	52
MRM of the Ventral Horn in the Rat and Pig Spinal Cord	52
Results.....	54
Alterations to Histology and MR Protocols	54
Staining for Iron Deposition in Immersion and Perfusion Fixed Mouse Striatum.....	55
MRM of Laminar Cell Layers in the Rat Hippocampus	55
Calculation of Diffusion-Limited and Bandwidth-Limited Resolution	55
MRM of the Ventral Horn in the Rat and Pig Spinal Cord	56
Discussion.....	57
Age-Dependent Iron Deposition in the Basal Ganglia.....	57
MRM of Laminar Cell Layers in the Rat Hippocampus	58
MRM of the Ventral Horn in the Rat and Pig Spinal Cord	59
4 MAGNETIC RESONANCE IMAGING OF MANGANESE UPTAKE AND NEURONAL ACTIVITY IN THE LIVE HIPPOCAMPAL SLICE MODEL.....	79
Introduction.....	79
Use of Manganese as a Contrast Agent in the Live-Slice Model of Rat Hippocampus	79
Diffusion-Weighted MRI of Neuronal Activity in the Live Hippocampal Slice Model	80
Methods	83
Use of Manganese as a Contrast Agent in the Live-Slice Model of Rat Hippocampus	83
Live hippocampal slice preparation	83
T ₁ -weighted MRI experiments	84
Data analysis of manganese-treated hippocampal slices.....	84
Diffusion-Weighted MRI of Neuronal Activity in the Live Hippocampal Slice Model	84
Live hippocampal slice preparation	84
Diffusion-weighted MRI experiments	85
Data analysis of activity experiments.....	86
Results.....	88
Use of Manganese as a Contrast Agent in the Live-Slice Model of Rat Hippocampus	88
Diffusion-Weighted MRI of Neuronal Activity in the Live Hippocampal Slice Model	89
Slice stability experiments	89
Potassium-induced neural activation and inhibition via MK-801.....	89
Magnetic Resonance Microscopy of kainate-induced neural activation.....	90
Kainate-induced neural activation and inhibition via CNQX	91
Kainate-induced neural activation with MK-801 pretreatment.....	91
Discussion.....	92

	Use of Manganese as a Contrast Agent in the Live-Slice Model of Rat Hippocampus	92
	Diffusion-Weighted MRI of Neuronal Activity in the Live Hippocampal Slice Model	93
5	DESIGN AND FABRICATION OF A MICROPERFUSION APPARATUS TO AID IN MAGNETIC RESONANCE MICROSCOPY OF LIVE TISSUE SLICES	114
	Introduction.....	114
	Design Considerations	114
	Methods	118
	Fabrication of a MR-Compatible, Microperfusion Rig for Conducting Live-Slice MRM.....	118
	Tissue retention apparatus	118
	Perfusion well and lines	119
	Paraffin sealing gasket	120
	Testing Perfusate Conditions in the Operational Microperfusion Rig	121
	Live-Slice Imaging of the CA1 region in Rat Hippocampus: A Pilot Study	122
	Live-slice preparation and perfusion rig assembly	122
	Magnetic resonance microscopy of the CA1 region in live hippocampal slices ..	124
	Results.....	125
	Testing Perfusate Conditions in the Operational Microperfusion Rig	125
	Live-Slice Imaging of the Pyramidal Cell Layer in Rat Hippocampus: A Pilot Study	126
	Discussion.....	126
	Fabrication of a MR-Compatible, Microperfusion Rig for Conducting Live-Slice MRM.....	126
	Live-Slice Imaging of the CA1 region in Rat Hippocampus: A Pilot Study	128
6	CONCLUSIONS AND FUTURE DIRECTIONS	143
	Identification of Hypointense Microstructures in Striatal MRM Images	143
	Clinical Relevance of MRM in Biological Tissues	144
	Interpretation of Diffusion Data in Biological Tissues.....	145
	Diffusion Data and Tissue Compartmentation	145
	Diffusion Data and Functional Imaging	147
	Future Directions	149
	Fabrication of a Helmholtz-Pair Style Microcoil Array.....	149
	Visualization of Perikerya, Axon Bundles, and Neural Activity Using Diffusion-Weighted MRM: Implications for Tissue Engineering	151
	Diffusion-Weighted fMRI	154
	APPENDIX: SPHERICAL COORDINATES FOR DIFFUSION GRADIENT DIRECTIONS USED IN DIFFUSION TENSOR IMAGING EXPERIMENTS	157

LIST OF REFERENCES158
BIOGRAPHICAL SKETCH171

LIST OF TABLES

<u>Table</u>		<u>page</u>
2-1	Signal to noise ratios calculated from images acquired on PBS phantoms with second-generation prototype surface microcoils	39
3-1	Estimated T_1 , T_2 , and apparent diffusion coefficient values for tissue laminae in the CA1 region of fixed rat hippocampus.....	71
4-1	Results of the biexponential analysis performed on normalized data from the live hippocampal slice experiment employing MK-801 pretreatment followed by kainate activation.....	113
5-1	Results of experiments chronicling pH, osmolality, and percent dissolved oxygen measurements of ACSF in the operational microperfusion rig.	137
5-2	Synopsis of the second series of experiments measuring pH taken at different locations in the microperfusion rig during operation.....	138
5-3	Results of the third set of experiments attempting to produce the desired perfusate conditions at the perfusate well.....	139

LIST OF FIGURES

<u>Figure</u>	<u>page</u>
2-1 Photographs of the 500 μ m surface microcoil developed by Bruker, Switzerland (Z76409).....	38
2-2 T ₂ -weighted 3D gradient echo image of rat striatum illustrating descending white matter tracts surrounded by gray matter.....	40
2-3 T ₂ -weighted 3D gradient echo images of a descending white matter tract and microstructures located in striatal gray matter.....	41
2-4 3D gradient echo image illustrating air bubbles trapped between the tissue sample and the coil face.....	42
2-5 3D gradient echo image (7.81 μ m isotropic resolution) taken in the rat striatum illustrating a tissue structure generating hypointense signal.....	43
2-6 Histological image of a Nissl-stained striatal cryosection (25 μ m slice thickness) taken at 400X magnification.....	44
2-7. Comparison of hypointense microstructures seen in our T ₂ *-weighted images and Nissl-stained neuronal cell bodies in the rat striatum.....	45
3-1 Nissl-stained rat hippocampus (100 μ m thick) illustrating laminar organization of cellular populations in slices taken perpendicular to the septo-temporal axis.....	62
3-2 Nissl-stained section of the rat spinal cord taken from the cervical enlargement illustrating microstructural elements along the boundary of the ventral horn.....	63
3-3 Direct correlation of descending white matter tracts in MRM and Nissl-stained histology images of the striatum.....	64
3-4 Schematic illustration depicting the combined protocol elements necessary to obtain MRM images with separate and distinguishable cell bodies.....	65
3-5 Staining for ferric and ferrous iron in the aged mouse striatum.....	66
3-6 High magnification (200X) image of cell bodies in the immersion fixed, aged (>2yr) CD1 mouse striatum following Perls staining for ferric iron.....	67
3-7 Diffusion-weighted spin echo image of the granule cell layer, hilum, and molecular layer in the dentate gyrus of the rat hippocampus imaged with the 200 μ m diameter microsurface coil.....	68

3-8	Spin echo image of the pyramidal cell layer, stratum oriens, and stratum radiatum in the CA1 region of the rat hippocampus taken with the 200 μ m diameter microsurface coil.....	69
3-9	Diffusion-weighted spin echo image of the pyramidal cell layer, stratum oriens, and stratum radiatum in the CA1 region of the rat hippocampus taken with the 50 μ m diameter microsurface coil.....	70
3-10	3D gradient echo image taken in the ventral horn of the rat from a cross section originating in the cervical spinal cord enlargement.....	72
3-11	Direct correlation of mammalian cell bodies in MRM and histology images.....	73
3-12	Direct correlation of mammalian cell morphology in MRM and histology images.....	74
3-13	Image illustrating MR signal heterogeneity within the cell body of a single alpha-motor neuron.....	75
3-14	ADC, diffusion orientation, and tractography maps generated from 21-direction HARDI acquisitions of a transverse spinal cord slice from the cervical enlargement of a rat with accompanying correlative histology.....	76
3-15	Series of Nissl-stained histology images of a fixed, transverse section from the lumbar enlargement of a rat spinal cord including overlays featuring DTI and DTM analysis.....	77
3-16	Diffusion-weighted MRM images of the spinal cord's ventral horn in the pig including ADC maps with diffusion orientation overlays.....	78
4-1	T ₁ -weighted image of a hippocampal slice from the 1000 μ M manganese treatment group.....	97
4-2	Mean signal to noise ratios for all manganese treatment groups (n = 5) reported as percent of control.....	98
4-3	T ₁ -weighted images from the live hippocampal slice protocol following a 1h bath application of manganese and a 24h wash in hypotonic ddH ₂ O containing no manganese.....	99
4-4	T ₁ -weighted image of a representative hippocampal slice from the 100 μ M manganese treatment group.....	100
4-5	Difference maps from rat hippocampal slices employed during our stability experiments overlaid on corresponding diffusion-weighted MR images.....	101
4-6	Plot of raw signal versus diffusion weighting for ROIs drawn in oxygenated ACSF perfusate and live-slice hippocampal tissue.....	102

4-7	Difference maps overlaid on corresponding diffusion-weighted MR images illustrating diffusion signal changes in rat hippocampal slices following exposure to elevated potassium ion concentration.....	103
4-8	Difference maps overlaid on corresponding diffusion-weighted MR images illustrating diffusion signal changes in rat hippocampal slices upon exposure to elevated potassium ion concentration following pretreatment with MK-801..	104
4-9	Bar graph representing the mean difference in signal to noise ratios between untreated rat hippocampal slices (n = 8) and those treated with the non-competitive NMDA receptor antagonist MK-801 (n = 10)..	105
4-10	Magnetic resonance microscopy of rat hippocampal slices treated with kainate to induce neural activity.....	106
4-11	Difference maps overlaid on corresponding diffusion-weighted MR images illustrating diffusion signal changes in rat hippocampal slices following exposure to kainate.....	107
4-12	Diffusion signal decay curves from live hippocampal slice (n = 6) experiment showing signal changes as a function of diffusion weighting before and after activation with kainate.....	108
4-13	Difference maps overlaid on corresponding diffusion-weighted MR images illustrating the relative lack of diffusion signal changes in rat hippocampal slices pre-treated with CNQX (6-cyano-7-nitroquinoxaline-2,3-dione) after kainate exposure.....	109
4-14	Difference maps overlaid on corresponding diffusion-weighted MR images illustrating the robust diffusion-signal increases after kainate exposure.....	110
4-15	Diffusion signal decay curves from live hippocampal slice (n = 6) experiment in which tissue was pretreated with MK-801 showing signal changes as a function of diffusion weighting before and after activation with kainate..	111
4-16	Diffusion signal decay curves in live hippocampal slice (n = 6) experiment generated from ROIs exhibiting the greatest magnitude of diffusion signal change before and after activation with kainate in MK-801 pretreated tissue.....	112
5-1	A schematic drawing of the components which comprise the tissue retention apparatus used in both fixed-sample and live-slice imaging experiments employing the microsurface coils.....	133
5-2	A schematic drawing of the microperfusion well component with PTFE perfusion lines extending from the well's top.....	134
5-3	Schematic drawing of a wax gasket used to seal the microperfusion rig during live-slice experiments.....	135

5-4	An exploded diagram of the microperfusion rig illustrating the order of assembly during our live-slice experiments.....	136
5-5	Mean values of T_1 and T_2 estimated from variable TR and variable TE live-slice experiment data (n = 6) respectively.....	140
5-6	Diffusion signal decay curves from live hippocampal slice (n = 5) experiments showing signal changes in CA1 tissue layers as a function of diffusion weighting.....	141
5-7	An exploded diagram illustrating the improved microperfusion rig design.....	142

Abstract of Dissertation Presented to the Graduate School
of the University of Florida in Partial Fulfillment of the
Requirements for the Degree of Doctor of Philosophy

EXAMINATION OF TISSUE MICROSTRUCTURE, CONTRAST ENHANCEMENT AND
NEURAL ACTIVITY IN THE BRAIN SLICE MODEL USING MAGNETIC RESONANCE
MICROSCOPY

By

Jeremy Joseph Flint

August 2009

Chair: Lucia Notterpek

Major: Medical Sciences--Neuroscience

This dissertation describes acute and fixed slice experiments conducted on neural tissue of rats and mice for the purposes of examining tissue microstructure and function using magnetic resonance microscopy. Structural studies employed a series of radiofrequency, microsurface coils in conjunction with novel slice-imaging techniques. These experiments achieved unprecedented levels of resolution in magnetic resonance imaging experiments of nervous system tissue and represent the first instances in which individual mammalian cells and axon bundles of the spinal cord were visualized directly using magnetic resonance techniques. Alpha-motor neurons in the ventral horn of the rat spinal cord were imaged with diffusion-weighted scan protocols by using tissue sections thinner than the slice thickness employed in the scan geometry. Combining these techniques allowed us to achieve a thinner effective slice in our images than could otherwise be obtained using our system hardware and scan protocol. Interestingly, our data suggests a higher intracellular than extracellular apparent diffusion coefficient refuting much of the literature regarding the effects of tissue compartmentation on diffusion signal. Imaging of axonal projections in the ventral horn was achieved using the microcoils to collect twenty-one direction HARDI acquisitions followed by tensor analysis and

diffusion tensor tractography. The presence of single cells and axons in our MR images were confirmed by comparing them to light microscopy images following histological analysis.

Our acute slice studies featured magnetic resonance microscopy in experiments exploring the utility of using manganese to increase signal and contrast in T_1 -weighted images and using diffusion-weighted imaging to detect signal changes associated with neural activity. The manganese doping experiments demonstrated concentrations appropriate for increasing signal or contrast through the shortening of T_1 relaxation or T_2 decay respectively. Experiments in which we induced neural firing in live slices resulted in cellular swelling which was detectible as a shift in diffusion properties.

The last series of experiments focused on combining the resolution of our structural studies with the ability to perform perturbation of living tissue slices. To this end, we designed and fabricated a microperfusion rig compatible with our imaging system hardware and the microsurface coils.

CHAPTER 1 BACKGROUND AND SIGNIFICANCE

Introduction

This dissertation is composed of experiments utilizing various magnetic resonance imaging (MRI) and histological techniques in order to better characterize the origins of signal in neurological tissues and describe physiological changes related to activity in these tissues. In order to unambiguously describe these properties, resolutions which attain or exceed the level of cellular structure are required. For this reason, we have employed excised tissue protocols coupled with high-field magnets and small-diameter microsurface coils in order to perform magnetic resonance microscopy (MRM). Using this technique allowed us to achieve the highest resolution scans of neural tissue to date and visualize tissue structures never before seen in MR images (Chapters 2 and 3). While these preliminary studies were instrumental in providing MR data on tissue morphology at the cellular level, they lacked the ability to describe tissue physiology because hardware design necessitated they be performed on fixed samples. The second series of experiments focused on measuring manganese uptake and neural activation in living tissue slices (Chapter 4). These studies provided data about physiological events occurring in the hippocampus, but could not achieve resolutions as high as those in our first series of experiments. The desire to collect physiological data from live tissue at resolutions approaching the cellular level lead to the design and fabrication of a microperfusion rig that could be used in conjunction with microsurface coils (Chapter 5). The following chapter is not meant to serve as an exhaustive review of the topics discussed, but rather as a basic overview of the methodologies relevant to this research.

Magnetic Resonance Microscopy of Excised Tissue: Microcoils and the Slice Model

While investigators have used slice isolation to study the morphological characteristics of tissue for hundreds of years, examining slice preparations of living tissue to yield physiological data is a technique developed only within the last century. This method of experimentation came about largely due to early attempts at quantifying the metabolic activity of various biological tissues (Krebs, 1981). Similar preparations were used in the middle of the twentieth century that employed electrophysiological and pharmacological techniques to measure the physical principals governing multiple aspects of membrane potential and neurotransmitter release respectively (Li and McIlwain, 1957; Sattin and Rall, 1970). Clearly, much of our knowledge regarding the intricate cellular processes necessary for physiological functioning is owed to research conducted using isolated tissue models.

In the late twentieth century, the slice model has been applied to newer and more advanced methods of research. Its role in MRI affords investigators the ability to observe layers of deep tissue strata at resolutions far greater than those garnered using otherwise similar *in vivo* protocols. These areas of research which focus on imaging portions of excised tissue have given rise to the field known as magnetic resonance microscopy. Just as with techniques employing light microscopy, this subfield of MRI specializes in resolving structures too small to be seen with the naked eye and, though roughly defined, it generally includes any MRI experiment conducted at in-plane resolutions of 100 μ m or less (Tyszka et al., 2005). The field of MRM—which is a relatively recent development—has been made possible thanks to large increases in available MR signal that can be traded for higher spatial resolutions in images. These signal increases have, in turn, been made possible thanks to the design and construction of more powerful superconducting magnet systems and smaller diameter radiofrequency microcoils.

Because signal intensity varies in an inverse-linear relationship to coil diameter, significant increases in the signal to noise ratio (SNR) are achieved when employing ever-smaller radiofrequency coils. The first true microcoils were used in nuclear magnetic resonance (NMR) spectroscopy rather than imaging experiments and were designed to aid in the analysis of volume-limited samples (Odelblad, 1966). More recently, thanks to advances in microfabrication techniques and the use of magnetic susceptibility matching medium, investigators have been able to apply spectroscopic analysis to samples in the nano-liter volume range (Olson et al., 1995). Such experiments generally involve insertion of the sample into a capillary tube which is then placed inside a solenoid-style microcoil: a linear, tube-shaped coil design employing multiple windings of an individual copper wire. Utilizing the most advanced MRI equipment available including ultra-high field spectrometers and small-diameter, solenoid microcoils, investigators have produced MR images and measured compartment-specific properties of single, excised *Aplysia* neurons and *Xenopus* oocytes (Aguayo et al., 1986; Hsu et al., 1996; Schoeniger et al., 1994). While this experimental design has been employed successfully in studies of both liquids and tissues, insertion of intact, unadulterated specimens into such narrow sample chambers can prove problematic. One potential complication of such practices includes the confounding of DWI data due to specimen compression (Drew et al., 2004; Leddy and Guilak, 2008). The use of surface coils is one way to remedy these problems, but this design exhibits its own limitations. Foremost is the surface coil's characteristic of inhomogeneity. In this case, signal output decreases rapidly as the distance from the coil increases. Regardless of design, the area contained within excitation profiles of all such microsurface coils is extremely limited; however, the possibility of generating amounts of signal sufficient enough to allow for resolution of micro-structural detail more than justifies their use. Moreover, the continued development of high-

resolution MR equipment coupled with improvements in scan protocol and contrast-agent design has facilitated the move towards reaching the theoretical $1\mu\text{m}$ to $2\mu\text{m}$ resolution limit of MRI (Ahn and Cho, 1991; Callaghan, 1991; Callaghan and Eccles, 1988; Cho et al., 1988). This is an extraordinary time in the development of MRI technology as resolutions in the stated range are needed to clearly resolve mammalian cells. The wide variety of imaging modalities available through MRI coupled with the vast increases in resolution offered by MRM ensure these techniques will remain at the forefront of medical imaging research as well as go on to advance methods of MR-driven clinical diagnosis.

Diffusion-Weighted Magnetic Resonance Imaging

One of the most powerful MRI techniques available—especially from a clinical standpoint—is the ability to quantify water diffusion. Diffusion-weighted imaging (DWI) is a powerful diagnostic tool because so many disease states can be recognized through imbalances in localized water homeostasis. Among other applications, DWI offers the ability to detect focal ischemic stroke (Minematsu et al., 1992; Moseley et al., 1990b), epilepsy (Zhong et al., 1993), and Creutzfeldt-Jakob disease (Kallenberg et al., 2006) as well as differentiate between multiple tumor types (Quadery and Okamoto, 2003; Rumboldt et al., 2006). The versatility of DWI stems from its unique ability to detect water restriction. Based on experimental observations that the apparent diffusion coefficient (ADC) is greater in free water than in tissue, researchers have examined and proposed multiple explanations for this phenomenon. While it cannot be said that there is a general consensus as to all the determinants of restriction and their relative effects, much has been discovered concerning the root causes of ADC variation. For example, the level of restriction exhibited by separate divisions of biological water—the primary cause of DWI contrast—is the result of differences in the microenvironments of water molecules. Barriers such

as cell or organelle membranes prevent isotropic diffusion and are thought to result in increased signal intensity on diffusion-weighted images. Other populations of water are restricted not by membranes, but rather because they are chemically bound to larger macromolecules such as lipids and proteins that are far more static than unbound water. Contrary to the previously described conditions, so-called free-water molecules exhibit relatively non-restricted diffusion properties. Because of dephasing attributed to the movement of water molecules between diffusion gradient pulses, free-water protons generate no signal in highly diffusion-weighted images unless they encounter restrictive barriers. To complicate the interpretation of restriction data in biological samples even further, there is continuous exchange between the different populations of water molecules. Also of note, these exchange rates can vary widely over time and location based on diverse factors such as membrane permeability, intermolecular forces, and temperature (Hufnagel et al., 2003; Thelwall et al., 2006; Vajda et al., 2004). Because it is uncertain how and to what extent structural and molecular characteristics affect the DWI contrast mechanism, alternate methods of analysis that offer increased resolution are needed to address this problem. Some recent experiments have focused on measuring the diffusion properties of separate tissue sub-populations in an effort to characterize different cell types under various external perturbations (Shepherd et al., 2006a). While diffusion tensor imaging (DTI) has helped elucidate the diffusion properties of tissue in general—and, when used for diffusion tensor tractography (DTT), white matter structure in particular (Mori and Zhang, 2006)—much of this previous work was performed at resolutions tens or hundreds of times less than those needed to resolve cellular structure. Such data are subject to error as a result of partial volume averaging effects and, as a consequence of this limitation, may not accurately represent the true diffusion properties and structures of tissues. Notably, as sub-populations of cells become increasingly

smaller and more difficult to segment, this error is magnified and reflected in the finalized, processed diffusion data. Excessive volume averaging is not a trivial issue in terms of studying central nervous system (CNS) pathologies such as Parkinson's and amyotrophic lateral sclerosis where tissue damage occurs in groupings of highly specialized neuronal projections (Armon 2008; Singh et al., 2007). This is also true of pathologies such as Alzheimer's disease where tissue damage is insidious to the extent of making diagnosis prior to the onset of disease symptomology all but impossible (Gouras, 2001). Employment of high-resolution MRM techniques in acquiring diffusion data holds promise for eliminating experimental error due to volume-averaging and, in turn, providing a more accurate representation of diffusion properties in tissues. Lastly, given that a subpopulation of water molecules undergoes compartmental change associated with the ion flux during generation of the action potential, diffusion-weighted scan protocols have the potential to be used as a novel means of performing functional MRI studies.

Diffusion Tensor Imaging and Tractography

Of all the potential uses of diffusion-weighted imaging methods, tensor imaging and its application to tractography is arguably the most important DWI method in terms of delineating the microstructural organization of neural tissues. This is due to DTT's ability to delineate the spatial location of white-matter tracts thanks to the high degree of anisotropy exhibited by these structures. The potential for determining the spatial characteristics of white matter tracts in the brain was discussed immediately following the initial observation that white matter exhibits high degrees of anisotropy in diffusion-weighted MR images (Moseley et al., 1990a). This conclusion was based on the observation that the MR signal in diffusion-weighted images of white matter changes depending on the diffusion-sensitizing gradient direction employed thus offering a means of determining fiber orientation based on the preferential orientation or water diffusion.

The first means of representing the orientation of anisotropic diffusion behavior within an image voxel involved a method known as diffusion tensor imaging (Basser et al., 1994). In the simplest case, the tensor consists of a three by three square matrix of vector quantities in which the three diagonal components represent diffusivities calculated along the x, y, and z axes while the off-diagonal components represent the correlations of diffusivity between orthogonal axes. The diagonal components are eigenvectors—each associated with a particular eigenvalue—that represent three-dimensional spatial variations in diffusivity. The eigenvector associated with the largest eigenvalue represents the orientation with the highest diffusivity and is thus denoted the primary eigenvector. In the case of highly anisotropic diffusion as seen in white matter, the magnitude of this vector is far greater than those of the other eigenvectors and can be represented as the long axis of an ellipsoid calculated from the tensor (Basser, 1995). Because diffusivity is higher along the length of a white-matter tract than orthogonal to it, the primary eigenvector is representative of the average orientation of these fibers within a voxel. This correlation forms the basis of using DTI methods to describe the spatial orientations of white-matter tracts within neural tissues.

While compilation of a diffusion tensor map can serve the purpose of representing voxel-specific diffusivity in three dimensions, delineation of white-matter tracts requires subsequent analysis known as diffusion tensor tractography (Mori et al., 1999). By performing additional analysis on diffusion tensor data, this method offers a means of determining the likelihood of intervoxel connectivity based on the thresholding of criteria such as fractional anisotropy and the angle of incidence between the primary eigenvectors of adjacent voxels (Jones et al., 1999). Because the determination of these criteria can be somewhat arbitrary since they are set by the analyzer rather than being inherent properties of the tissue under investigation, validation of the

tract predictions made by numerous DTT methods is still an area of active research. Some groups depend on the morphology of well established, macroscopic white-matter structures such as the corpus callosum and arcuate fasciculus for validation (Barrick et al., 2009). Other groups have employed manganese as an MR-detectible, tract-tracing element thus generating data about the continuity and spatial positioning of tracts which can then be correlated with DTT data as a means of validation (Lin et al., 2001; Yamada et al., 2008). Independent of the specific methodologies used, DTT validation techniques in biological samples have thus far been reliant on the most substantial of white matter structures. This has led to a situation in which there is little doubt of DTT's ability to correctly predict connectivity in large, dense areas of white matter but less certainty in its accuracy as the bundled tracts arborize and become more diffuse. What's more, there is not yet a reliable method for predicting the physical limits of DTT's predictive accuracy. For these reasons, it is essential that the development of more advanced validation methods for tractography data continues.

Contrast Agents

One of the most recent advances in the field of MRI involves the use of exogenous agents employed to increase the signal or contrast generated from tissue. The increased signal can be used in a variety of ways including increased spatial resolution or shorter scan times while contrast changes can help resolve otherwise unseen structures. Many techniques have been developed to take advantage of specific contrast agents. The use of hyperpolarized gasses has improved imaging of the respiratory system by reducing susceptibility artifacts caused by air within the lungs (Johnson et al., 1997). Also, researchers have incorporated super-paramagnetic iron oxide particles into cultured cells as a means of tracking them with MRI following implantation (Foster-Gareau et al., 2003; Heyn et al., 2006; Shapiro et al., 2006). Manganese is another such paramagnetic substance that has received widespread attention in MRI research

since its contrast-enhancing properties were first described (Jackson et al., 1985; Koenig and Brown, 1985; Wolf et al., 1985). Aside from enhancing contrast, manganese has been shown to be a useful tool in neuronal tract tracing studies thanks to its ability to be taken up by voltage-gated calcium channels (Narita et al., 1990). Indeed, its identity as a similarly-proportioned divalent cation allows manganese to act in biological processes more commonly reserved for calcium ions and, therefore, offers the potential for MRI investigation of calcium-dependent events. For example, muscle contraction is a well-researched biological process known to be dependent on calcium for the linking of myosin heads to their corresponding actin filaments (Davies, 1963). Numerous studies have been conducted indicating that manganese ions act as calcium surrogates in such reactions (Nasu, 1995; Nasu and Baba, 1997). Although less research has been directed at elucidating the mechanisms of calcium-dependent processes that do not relate to muscle contraction, the role that calcium plays in triggering apoptotic cell death has been well established (Bellomo, 1992; Mattson and Chan, 2003), and studies have shown that manganese can activate the cellular machinery responsible for inducing apoptotic cell death (Gonzalez et al., 2008). The highly-regulated nature of biological calcium ensures that even small changes in its relative levels are readily sensed by cells, and has ensured its niche in the signaling cascades of various physiological processes. Although calcium cannot be measured directly through MRI analysis, manganese offers a potential means of visualizing these processes indirectly. Its relatively fast rate of tissue infusion coupled with its slow rate of release makes it a perfect match for high-resolution MRI protocol requiring quick preparation times followed by prolonged imaging periods.

Unfortunately, for all its potential usefulness, manganese is a somewhat unlikely choice as a contrast agent for use in MRI experiments on biological tissues. This is because one of the

greatest benefits of MRI—namely, its non-invasiveness—is compromised in experiments employing manganese due to its neurotoxic properties (Crossgrove and Zheng, 2004; Dobson et al., 2004). Arguably, despite its toxic properties, utilizing manganese as a contrast agent may still afford less risk than imaging modalities requiring the use of ionizing radiation. Also, all contrast agents by definition carry some degree of invasiveness due to the requirement that they be introduced to the organism being studied as an exogenous substance. As with many useful chemical agents that exhibit negative side effects, the most crucial elements of using manganese for medical purposes must include establishing acceptable dosage limits and conducting case-specific risk-benefit analysis. Regardless of its limited clinical utility, the incredible potential of manganese to help elucidate calcium-dependent biological processes makes it an ideal contrast agent for use in MRI research.

CHAPTER 2
PRELIMINARY MAGNETIC RESONANCE MICROSCOPY STUDIES OF NEURAL
STRUCTURE IN THE CENTRAL NERVOUS SYSTEMS OF RATS AND MICE

Introduction

Because of the resolution limitations inherent to previous generations of MR scanners, little is known about specific mechanisms which influence the MR signal at the cellular level. Elucidating these mechanisms is the key to being able to accurately describe physiological processes via MR. Moreover, studies which have focused on identifying and quantifying these mechanisms must often rely on mathematical models or non-mammalian organisms to describe and generate data respectively. While methods such as these are the current standard in scientific research, fundamental assumptions must be made when models are employed and many available today lack suitable options for validation. Since developing the techniques necessary to achieve what Aguayo coined “the NMR imaging microscope”, MRM has evolved into an independent field of MRI research (Aguayo et al., 1986). Studies which use MRM to examine biological tissues have tremendous potential to influence the future of diagnostic medicine. This is due in part to the fact that MRI is already an established and acceptable method of noninvasive imaging in the clinic, but more so because disease states often manifest at the cellular level long before a diagnosable symptomatology develops in the patient. Because early diagnosis and access to treatment are paramount in achieving a favorable disease prognosis, diagnostic methods that are capable of detecting pathologies at their earliest stages are those which are most likely to benefit patient outcome (Domenighetti, 2007; Greenlee et al., 2001). Unfortunately, due to technological limitations, no method of noninvasive diagnostic medicine which resolves structure at the cellular level currently exists. If diseases which manifest at the cellular level are to be accurately and reliably diagnosed via MRI prior to the advent of MR technology that would allow for direct, *in vivo* observation of cellular structure, a thorough understanding of how tissue

structure influences the NMR signal will be required. With this goal in mind, we set out to obtain MRM images in the rat and mouse CNS that could be used to characterize the NMR properties of tissue microstructure.

Methods

Prototype Microsurface Coil Characterization

Prior to using microcoils (Figure 2-1) for the generation of experimental data, phosphate-buffered saline (PBS; 137mM NaCl, 2.7mM KCl, 10mM Na₂HPO₄, and 1.8mM KH₂PO₄; pH 7.4 at 300mOsm) phantoms were imaged using standard, spin echo pulse sequences (TR = 2000ms, TE = 7ms) in an effort to characterize the prototype surface coils and ensure functional soundness. Orthogonal slice selection was employed in two separate imaging experiments for each coil so as to generate images parallel as well as perpendicular to the coil face. In conjunction with a 50W amplifier, attenuation settings for RF power in these scans were roughly 70db, 65db, 60db and 50db for the 50μm, 100μm, 200μm, and 500μm coils respectively. Following imaging of the phantoms, regions of interest (ROIs) were selected from areas exhibiting high signal intensity (ROI_1) and areas outside the coils excitation profile (ROI_2). The signal to noise ratio (SNR) was then calculated for each image using the equation;

$$SNR_{ROI} = (S_{Avg} - N_{Avg}) / N_{Std} \quad (2-1)$$

Where SNR_{ROI} is the signal to noise ratio of ROI_1 selected for analysis, S_{Avg} is the mean signal within ROI_1, N_{Avg} is the mean noise within ROI_2, and N_{Std} is the standard deviation of the noise in ROI_2.

Calculation of Diffusion-Limited and Bandwidth-Limited Resolution

In order to insure the nominal resolutions reported in our MRM experiments were not exceeded by resolution-limiting factors such as diffusion occurring during gradient pulses or the bandwidth employed, these resolution limits were calculated using methods described by

Ciobanu and Cho respectively (Cho et al., 1990; Ciobanu et al., 2003). The resolution limit due to the bandwidth was calculated using the equation;

$$\text{Lim(B)} = \pi / (\gamma \times G \times \text{Acq}) \quad (2-2)$$

Where Lim(B) is the resolution limit due to the bandwidth, γ is the gyromagnetic ratio of hydrogen, G is the strength of the read gradient, and Acq is the acquisition time. The resolution limit due to diffusion during frequency encoding was calculated using the equation;

$$\text{Lim(F)} = ((2.8 \times D) / (\gamma \times G))^{1/3} \quad (2-3)$$

Where Lim(F) is the resolution limit due to diffusion during frequency encoding, D is the apparent diffusion coefficient, γ is the gyromagnetic ratio of hydrogen, and G is the strength of the frequency encoding gradient. The resolution limit due to diffusion during phase encoding was calculated using the equation;

$$\text{Lim(P)} = ((1.8 \times D) / (\gamma \times G))^{1/3} \quad (2-4)$$

Where Lim(P) is the resolution limit due to diffusion during phase encoding, D is the apparent diffusion coefficient, γ is the gyromagnetic ratio of hydrogen, and G is the strength of the phase encoding gradient.

Imaging of Fixed Tissue Slices: Preliminary Data

All animal procedures described in this document complied with guidelines set forth in the National Academies of Sciences' *Guide for the Care and Use of Laboratory Animals* and were approved by the University of Florida IACUC. Male CD1 mice (50g) and Sprague Dawley Rats (150g) were anesthetized by inhalation of isoflurane gas over a period of four minutes until unconscious. To ensure insensitivity to pain, the absence of righting, toe-pinch, and ocular reflexes was confirmed prior to euthanization by decapitation. Following euthanization, the brain was removed by gross dissection and placed onto a piece of filter paper (Whatman, 1004-110)

taped to the stage of a McIlwain tissue chopper in order to prevent shifting during the cutting procedure. The brain was then rapidly cut into sagittal slices (500 μ m) that were immersion fixed in PBS containing 4% formaldehyde for a period no shorter than 24h. Prior to imaging, a brain slice taken approximately 2mm to 3mm laterally from midline and containing an appreciable amount of striatal tissue was selected and a 4mm by 4mm square of striatum was excised by hand in order to accommodate placement into the microcoils sample well. The striatum was first selected as a suitable neural tissue for preliminary testing due to its high degree of uniform, microscopic heterogeneity. Prior to the development of a tissue retention apparatus (Chapter 5) employing sagittal slices of striatum ensured that, regardless of tissue position within the well, both gray matter—primarily medium spiny neurons and microglia—and white matter—descending tracts of the striatum—fell within the coils excitation profile. This tissue (4mm x 4mm x 500 μ m) was then washed overnight in PBS adjusted to physiological conditions in order to remove fixative. Washed samples were placed inside the sample well of the 200 μ m diameter microsurface coil (Bruker Switzerland, Z76412), immersed in PBS, and covered by a 9mm x 9mm square of PCR film (ABgene, AB-0558). This film served the dual purpose of preventing both sample movement and evaporation of the surrounding PBS during imaging. Data were acquired on a 600MHz vertical spectrometer (Oxford) interfaced to a Bruker console. Three dimensional gradient echo images were acquired at isotropic resolutions ranging from 4.7 μ m to 9.4 μ m. Repetition times ranged from 150ms to 300ms, and echo times ranged from 10ms to 20ms. Acquisition times ranged from roughly 3h to 22h depending primarily on the resolution and averaging employed. Processed images were smoothed using the linear or quadratic filter algorithms available as part of the ParaVision processing toolkit (Bruker, ParaVision 3.1).

Tissue Histology: Preliminary Data

Following imaging, tissue slices were immersed overnight in PBS containing 30% sucrose as a means of cryoprotection prior to sectioning. Slices were then placed in cryosectioning medium (Richard-Allan, 6502) and snap-frozen in a bath of methanol and dry ice. Tissue was cut into 25 μ m increments (Microm, HM 505 E Cryostat), and affixed to poly-L-coated microscope slides. After allowing tissue slices to adhere overnight, slides were Nissl stained (0.5% Cresyl Violet, 0.3% Glacial Acetic Acid, 99.2% ddH₂O) for a period of 3min to 4min, destained (0.3% Glacial Acetic Acid, 99.7 % ddH₂O) for a period of 1min to 2min, wet mounted (National Diagnostics, HS-103), and photographed at 200X or 400X magnification using a digital camera (QImaging, Retiga 4000R Fast 1394 Color) attached to a Zeiss microscope (Axioplan 2, Zeiss) and processed with software (QCapture Pro 6.0) available from QImaging.

Results

Prototype Microsurface Coil Characterization

Signal to noise ratio calculations for four second-generation microsurface coils of diameter 500 μ m, 200 μ m, 100 μ m, and 50 μ m (Bruker Switzerland, Z76409, Z76412, Z76415, and Z76418 respectively) are summarized in table 2-1. All but one coil—the 100 μ m—exhibited the expected behavior of increasing SNR with decreasing coil diameter; however, increases in SNR did not conform to the expected inverse linear relationship to coil diameter.

Calculation of Diffusion-Limited and Bandwidth-Limited Resolution

For the scan parameters employed in our MRM images of the mouse striatum ($G_{\text{phase}} = 1803.77\text{mT/m}$, $G_{\text{read}} = 1951.62\text{mT/m}$, acquisition time = 2.56ms) when using an apparent diffusion coefficient (1.0 $\mu\text{m}^2/\text{ms}$) representative of diffusion rates equal to or exceeding the

uppermost values expected for healthy neural tissues, the resolution limits due to the bandwidth, diffusion during frequency encoding, and diffusion during phase encoding were calculated to be 2.35 μm , 3.23 μm , and 2.86 μm respectively. These values were well under our lowest nominal resolution (4.7 μm) for this series of scans indicating that no adjustments to the reported digital resolution were necessary.

Imaging of Fixed Tissue Slices: Preliminary Data

While conducting preliminary tests on the prototype version of the 200 μm diameter microsurface coil, several structures were described during the course of imaging formaldehyde-fixed tissue slices from the rat and mouse striatum and hippocampus. The first tissue contrast obtained on our MR images was between white and gray matter populations of the striatum (Figure 2-2). Shortly thereafter, images containing tissue contrast belonging to microstructures of unknown origin were taken in the striatum (Figure 2-3). The microstructures measured 10 μm to 15 μm in diameter and exhibited hypointense signal in our primarily T_2^* -weighted images. Unlike the continuous, linear formations of the striatal white matter tracts, these structures were discrete and thus contributed to a punctate appearance in the striatal gray matter. Microbubbles trapped between the coil face and tissue in the microcoils sample well were also imaged at this time (Figure 2-4). Lastly, a separate group of linear structures expressing low signal intensity was visualized (Figure 2-5). These differed structurally from the white matter tracts described previously in that they exhibited blebbing.

Tissue Histology: Preliminary Data

Nissl staining and subsequent light microscopy revealed tissue structures expected to be present in the rodent striatum. Nissl-stained cell bodies of medium spiny neurons and descending white matter tracts were visualized (Figures 2-6 and 2-7, A). The morphological characteristics

and distribution pattern of cell bodies in the striatum were found to be similar to those exhibited by the microstructures seen in our T_2^* -weighted, 3D gradient echo MR images (Figure 2-7). Despite the similarities described, no example of direct correlative histology was achieved during this period of study.

Discussion

Coil Characterization

The sub-optimal increases in SNR described in the results from our microcoil testing experiment can be attributed to excessive caution being exercised during imaging experiments. Because the coils were designed with no fail-safe mechanism to prevent hardware damage due to large radiofrequency (RF) power deposition, emphasis—especially during the earliest experimental phase—was placed on preservation of the coil rather than achieving the largest permissible SNR value. Although some coils were supplied with documentation describing operational limits for the RF power used, this was not true of all microcoils. As such, measurements of the output power supplied by the 50W amplifiers during specific imaging experiments were conducted and this information used to extrapolate the operational limits of the other coils. Complicating this procedure was the fact that these measurements applied only to the pulse sequence parameters that were in effect during our original measurements of power output. Also, the attenuators for the RF power supply operate on a logarithmic decibel scale making fractional scaling of power usage—i.e. switching from an arbitrary power setting to half or twice that amount—quite simple while making exact calculation of the power output rather difficult. Because of these factors, a certain level of ambiguity in selecting the appropriate RF power output was always present. Despite these difficulties, all coils tested were able to produce sufficient signal. The 100 μ m diameter coil; however, did not generate SNR values between that of the 50 μ m and 200 μ m coils as would be expected, but instead underperformed the 200 μ m coil.

The only insight into this result being a note made in the experimental log stating that, for this particular experiment, an appropriate match and tune of the coil was never achieved prior to imaging. This factor could account for the lower than expected SNR exhibited by the coil. As such, the 100 μm coil was excluded from use for all subsequent experiments. Lastly, the large disparity between SNR measurements taken parallel and perpendicular to the coil face may be explained by variations in the surface coil's excitation profile due to RF inhomogeneities. Because signal decreases rapidly with distance from the coil face, images taken parallel to the coil's face were lacking in signal from the spatial region where the highest signal is generated: i.e. from the water protons closest to the coil. This effect was reversed in the case where the image slice was taken orthogonal to the coil face as the plane of the image slice passed through the coil face itself.

Imaging of Fixed Tissue Slices: Preliminary Data

Imaging of fixed striatal slices in the mouse and rat provided us with an early means of validating that the prototype microsurface coils could be used to generate T_2^* contrast in neural tissue allowing for the differentiation between white and gray matter. Imaging of the hypointense, discrete microstructures present throughout the striatal gray matter was an unforeseen development.

At first, due to their small size—10 μm to 15 μm in diameter—and the grainy appearance of our high-resolution images, these areas of low signal were assumed to be background noise. However, following optimization of the pulse program for tissue contrast, it was noted that—unlike the behavior exhibited by random noise—the structures were of a consistent size, were present in images acquired from multiple striatum samples, and—most importantly—exhibited a reproducible pattern of spatial localization in separate images acquired from the same sample

(Figure 2-2). Clearly, these signal voids were attributable to some microstructural sample element of unknown origin.

After ruling out noise artifacts, the possibility that these low signal regions could have been due to susceptibility artifact caused by gas was considered; however, this hypothesis was quickly discounted. Even though both were known to manifest as signal voids on T_2^* -weighted images, the dissimilar morphological features between the two provided convincing evidence that the microstructures were not air bubbles. First, the microstructures appeared throughout the volume of the 3D data set rather than as a surface phenomenon which would be observed in the case of air bubbles. Because gas pockets are not commonly found within healthy mammalian neural tissue, it is highly unlikely we would have detected microbubbles in the magnitude seen in our MR images. Also, because of a frequency shift effect, susceptibility artifacts caused by gasses exhibit high intensity signal in the region surrounding the signal void (Figure 2-3). The microstructures, while surrounded by areas of higher signal intensity, did not exhibit this characteristic effect which occurs at liquid to gas interfaces in MRI.

Next, the possibility that iron was causing these signal voids was considered. Because the animal subject from which striatal tissue was taken had not been exsanguinated prior to imaging, there was the distinct possibility that the iron component of the haemoglobin molecule within the blood was responsible (Schalekamp et al., 1975). Although this scenario was possible, it was considered unlikely since the microstructures differed morphologically from structures presumed to be vasculature (Figure 2-4). However, lacking unambiguous structural validation for the contrast described in figure 2-4, we could not rule out this possibility. As iron has been shown to collect in numerous brain regions in an age-dependent manner including cells of the basal ganglia (Benkovic and Connor, 1993; Roskams and Connor, 1994; Focht et al., 1997) as well as

cause susceptibility artifacts in MR images (Milton et al., 1991; Yamada et al., 2002) this was considered the most likely origin of the signal contrast. The mice used in our preliminary experiments were aged animals and could presumably have exhibited varying levels of iron deposition in their striatal tissue. Perhaps most importantly—unlike the previous example—this scenario offered an explanation of the MR tissue morphology as the iron would be sequestered inside the bodies of cells rather than in the vasculature: thus leading to the discrete, round structures described rather than linear, continuous structures one would expect from blood vessels.

Tissue Histology: Preliminary Data

Although we were successful at performing cryosectioning, Nissl staining, and microscopy on fixed tissue slices, achieving direct correlative evidence between MR and microscopy images of tissue microstructure did not occur at this time. There were numerous reasons for this outcome associated with the histology protocol. First, due to characteristics associated with the use of a surface coil, MR images were universally acquired on the most superficial layer of the tissue slice. These superficial tissue layers are frequently lost during cryosectioning due to their proximity to the interface between tissue and sectioning medium. Also, matching the sectioning plane during slicing to the imaging plane achieved during MR scanning was not possible. This variation, even when slight, resulted in slice angle differences between the MR data and cryostat tissue sections. Lastly, because tissue thickness of the initial frozen tissue section—being comprised of both tissue and sectioning medium in proportions which summed to the selected cryosection thickness—could not be controlled, the tissue structures contained in individual cryosections differed from those contained in the one-voxel-thick slices of MRI data. This was true even when the selected cryosection thickness and imaging voxel thickness were the same value. Collectively, the limitations described resulted in different portions of the striatal tissue

slice being represented in the light and MR microscopy data making direct correlation impossible.

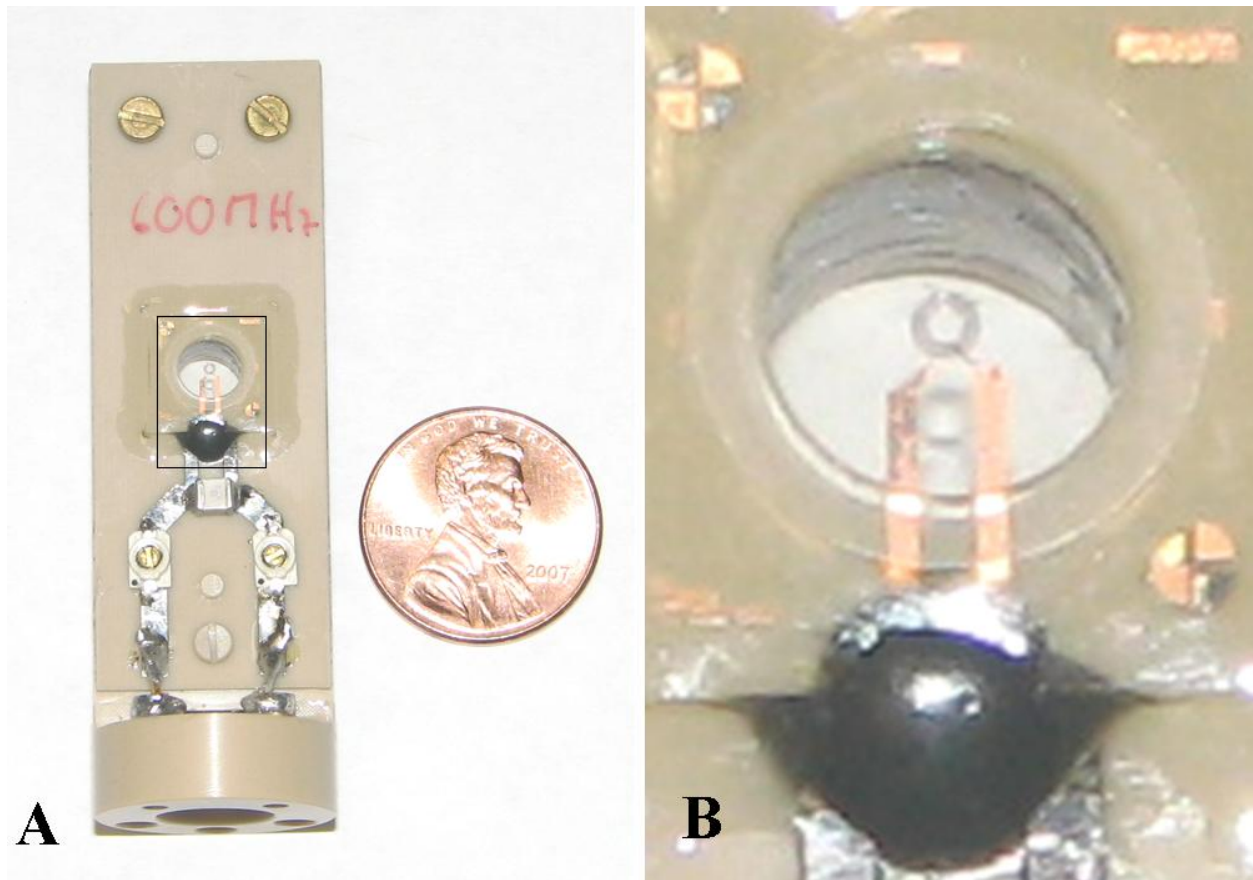


Figure 2-1. Photographs of the 500µm surface microcoil developed by Bruker, Switzerland (Z76409). A) Picture showing the coil next to a U.S. penny for scale. B) Magnified picture of the box insert from (A) showing the four-turn surface coil which sits in a 5mm diameter, 500µm deep tissue well. The well's surface is coated with a biocompatible polyxylylene polymer that protects the coil from wear. Microsurface coils of 200µm and 50µm diameter were also used during the course of the present study.

Table 2-1. Signal to noise ratios calculated from images acquired on PBS phantoms with second-generation prototype surface microcoils.

Coil Diameter	500 μ m	200 μ m	100 μ m	50 μ m
Calculated SNR (Image Orthogonal to Coil Face)	225.18	270.27	207.46	311.20
Calculated SNR (Image Parallel to Coil Face)	15.20	31.60	18.00	43.50

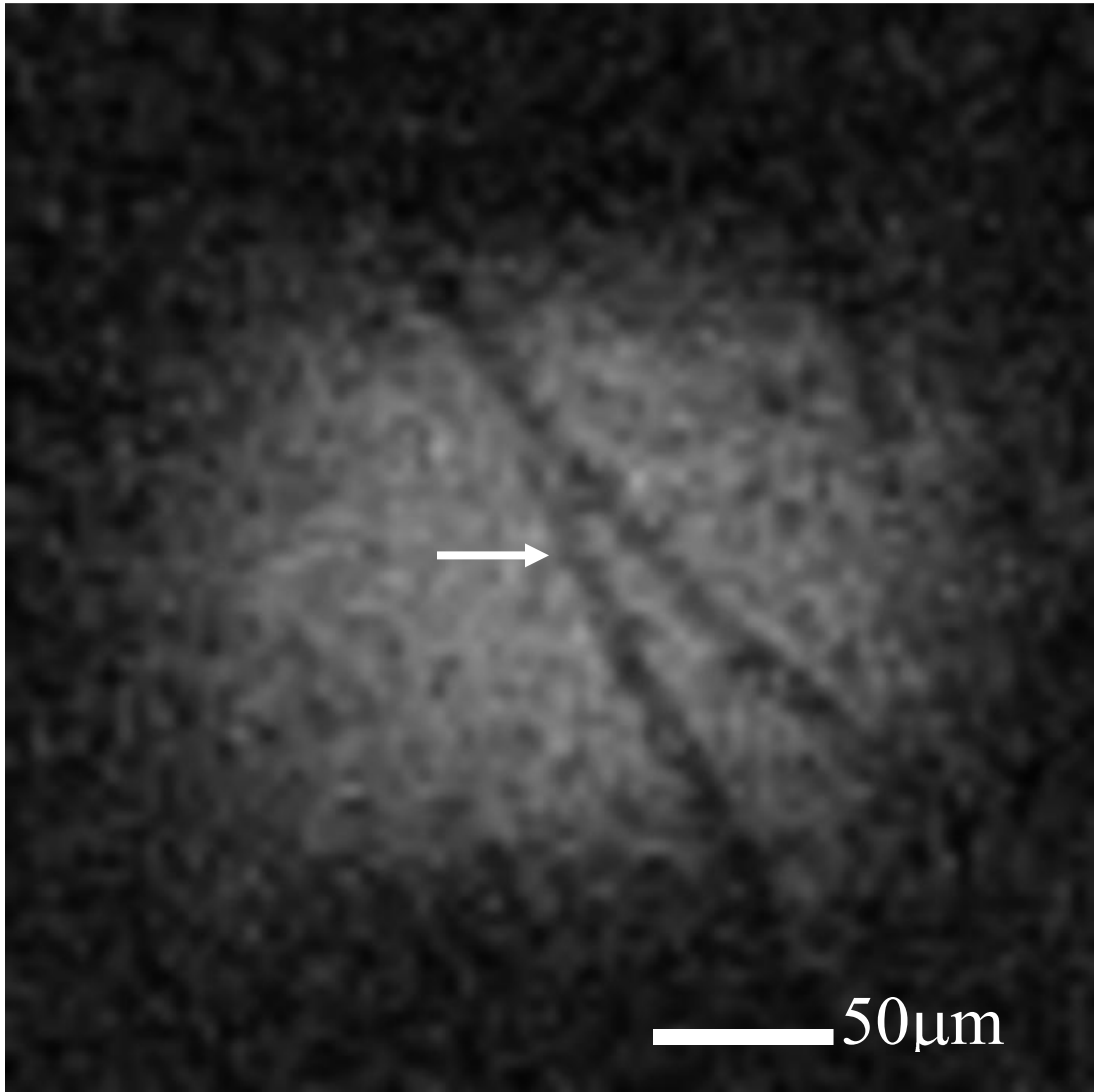


Figure 2-2. T₂-weighted 3D gradient echo image of rat striatum illustrating descending white matter tracts (arrow) surrounded by gray matter (remaining field). Imaging parameters: matrix = 128³, spectral width = 20KHz, pulse angle = 30°, TR = 150ms, TE = 20ms, FOV = 0.10cm × 0.10cm × 0.05cm, Avg = 32, voxel element = 238 fL.

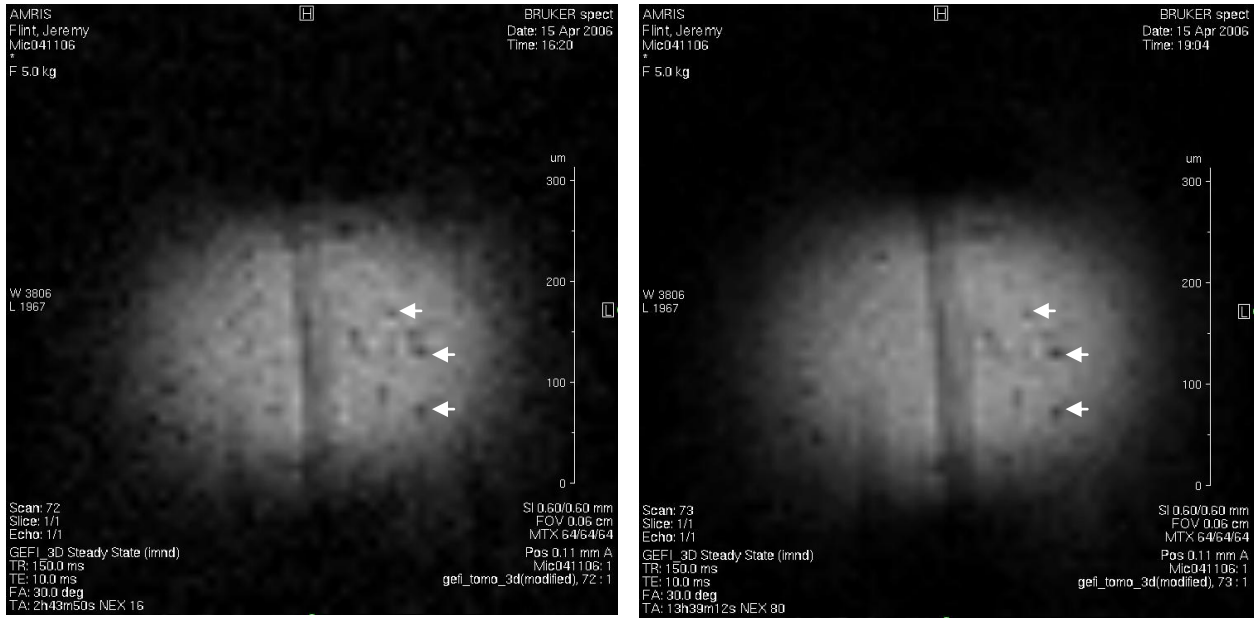


Figure 2-3. T₂-weighted 3D gradient echo images of a descending white matter tract (center) and microstructures (arrows) located in striatal gray matter. The described microstructures are visible in subsequent MR scans and correlate morphologically and spatially between scans. Imaging parameters: pulse angle = 30°, TR = 150ms, TE = 10ms, resolution = 9.375μm isotropic.

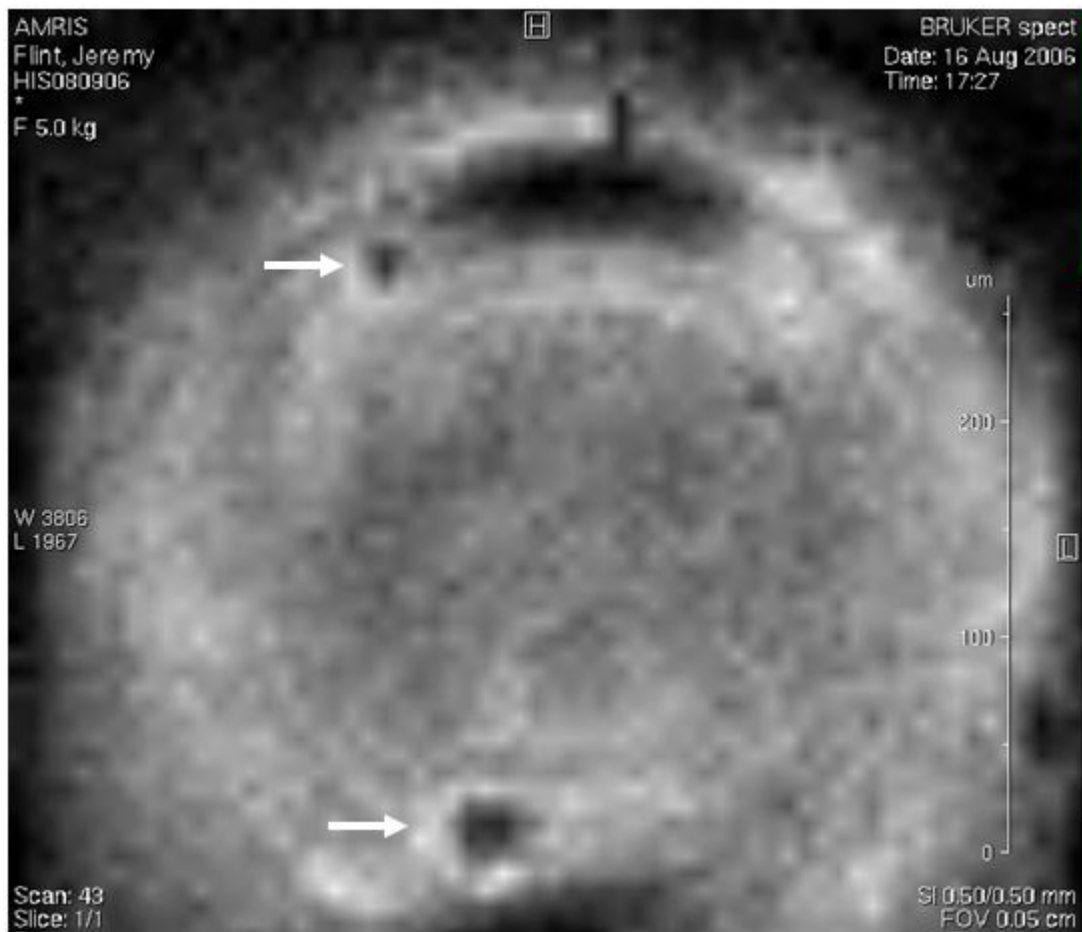


Figure 2-4. 3D gradient echo image illustrating air bubbles (arrows) trapped between the tissue sample and the coil face. Proximity to the coil face is evident due to the circular banding pattern present caused by individual turns of the four-turn coil.

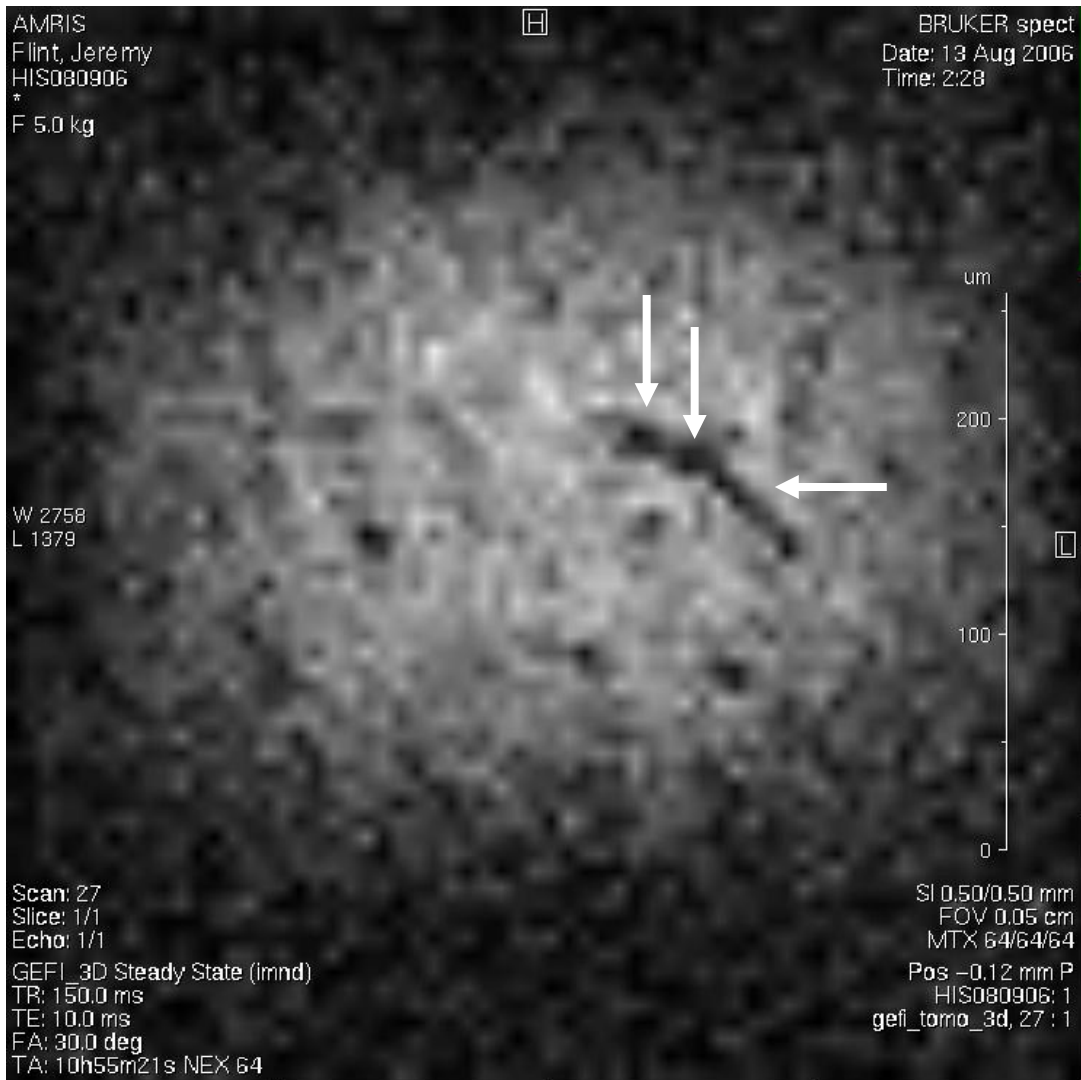


Figure 2-5. 3D gradient echo image ($7.81\mu\text{m}$ isotropic resolution) taken in the rat striatum illustrating a tissue structure (horizontal arrow) generating hypointense signal. The roughly linear structure exhibits blebbing as evidenced by areas of increased width (vertical arrows) along its central axis.

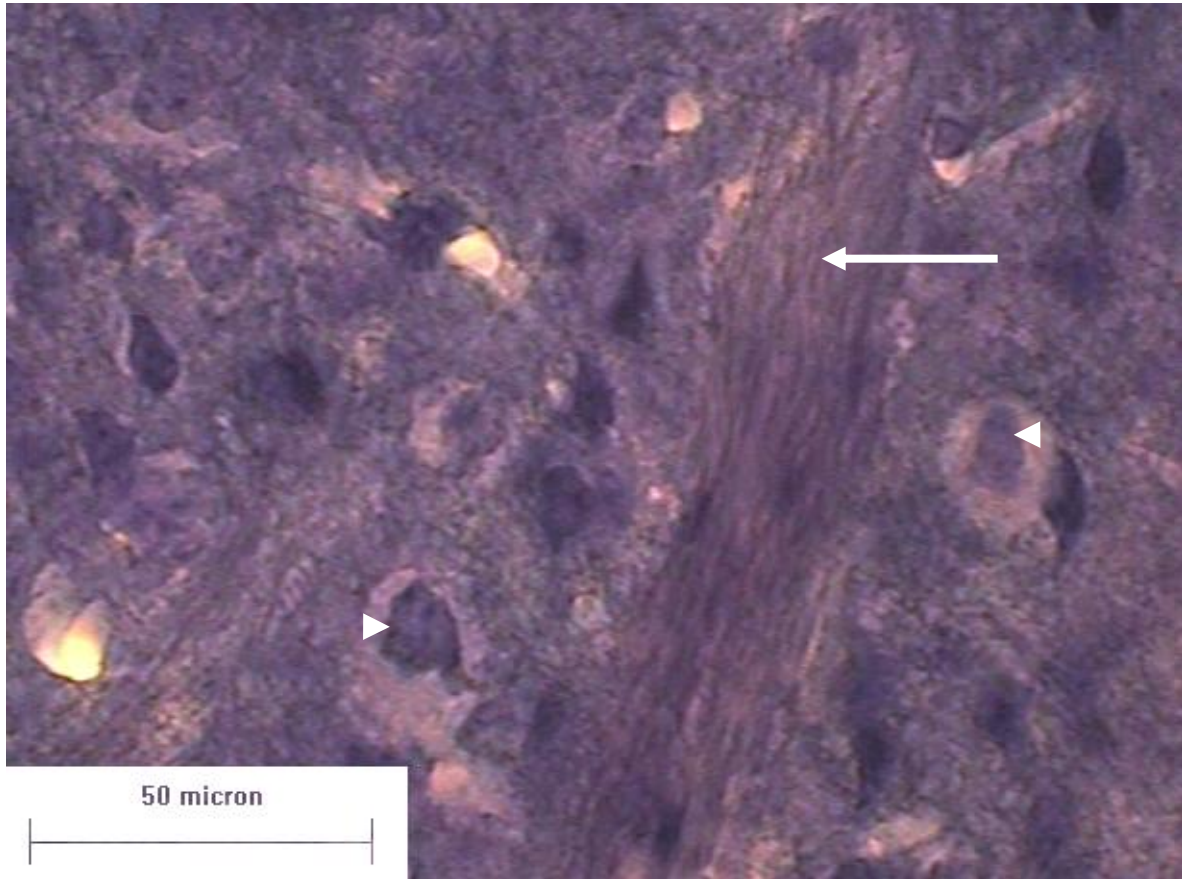


Figure 2-6. Histological image of a Nissl-stained striatal cryosection (25 μ m slice thickness) taken at 400X magnification. Microstructures visible in the slice include Nissl-stained cell bodies of medium spiny neurons (arrow heads) and a white matter tract (arrow).

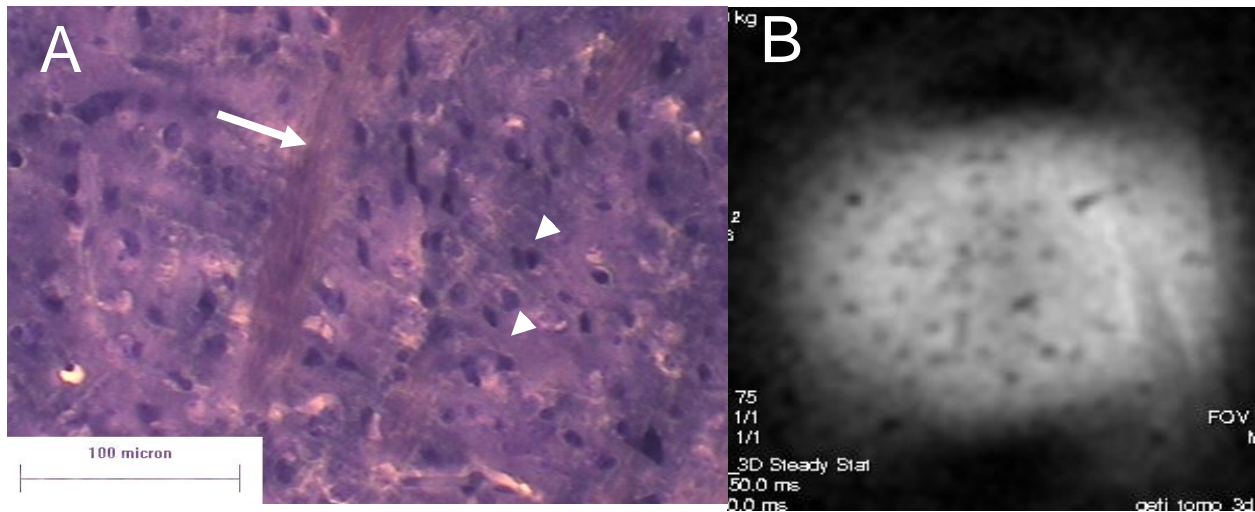


Figure 2-7. Comparison of hypointense microstructures seen in our T_2 -weighted images and Nissl-stained neuronal cell bodies in the rat striatum. A) Histological image of a Nissl-stained striatal cryosection ($25\mu\text{m}$ slice thickness) taken at 200X magnification. A descending white matter tract (arrow) and cell bodies (arrowheads) are visible. B) 3D gradient echo image ($4.7\mu\text{m}$ isotropic resolution) with discrete microstructures. Although the data are not correlative, the structures are similar in morphology and distribution to cell bodies of medium spiny neurons in the striatum.

CHAPTER 3
MAGNETIC RESONANCE MICROSCOPY OF SINGLE MAMMALIAN NEURONS AND
TRACTOGRAPHY OF INDIVIDUAL AXON BUNDLES

Introduction

After ruling out the possibility of image artifact in our preliminary MRM studies, it was decided that the structural origin of the hypointense signal regions in the striatum should be investigated. Based on the morphological evidence, we were trying to identify microstructural tissue elements located in the striatum that are ubiquitous throughout the gray matter. These structures are discrete in that they show no obvious pattern of connectivity, roughly spherical in shape, and on the order of 10 μ m to 15 μ m in diameter. The spherical nature of the structures offers strong evidence in support of the hypothesis that cell bodies are somehow involved with defining the morphological boundaries of the signal contrast. In other words, it is possible that the observed contrast is due to inherent contrast differences between cell bodies and the tissues that surround them, but it is just as likely that a compound sequestered within the cell bodies is the source of this contrast. Previous studies employing confocal microscopy taken at 1 μ m-step increments through fixed rat striatum describe the perikarya of medium spiny neurons as being roughly the same diameter as the microstructures in our MRM images of the striatum (Arvidsson et al., 2002). Studies employing immunohistochemical analysis to observe microglia and oligodendrocytes—both of which are known to reside in striatal tissue—report cell body dimensions roughly similar in size and shape to the structures observed in our preliminary data (Yasuda et al., 2007; Redondo et al., 2007). Taking into account our previous findings, we hypothesize that the tissue structures in our MR images are most likely cell bodies and that the observed contrast is most likely due to age-dependent iron deposition. Because histology is still the benchmark method for analysis of tissue morphology, we have continued to attempt

correlative analysis of our MRI datasets to histological slices; however, changes were made to the protocols in hopes of improving the chances for obtaining a direct correlation. First, performing histological cryosectioning following MRM experiments was abandoned in favor of a protocol that includes vibratome tissue sectioning prior to either MR or optical imaging sessions. This change aimed to better preserve the quality of tissue microstructure in the slices by avoiding freeze-thaw cycles that are known to disrupt membrane integrity and could confound diffusion measurements in our MR experiments (Acker and McGann, 2000; Parker, 2004). More importantly, the new protocol was expected to eliminate difficulties with image correlation because sectioning the tissue prior to experimentation would ensure that the exact same microstructural tissue elements are represented in both imaging datasets. Also, Perls and Turnbull's blue stain protocols were incorporated in hopes of localizing potential iron deposits in striatal tissue (Carthew et al., 1993; Phuttharak et al., 2005; Wang et al., 2002). A perfusion fixation protocol including exsanguination prior to the introduction of formaldehyde was employed in later experiments to remove blood haemoglobin as a potential source of susceptibility contrast. Furthermore, because cell bodies in the striatum are so small as to be at the very limit of our structural resolution capabilities, other cellular populations were considered for MR analysis. Cell bodies arranged in a laminar fashion—such as those seen in the granule and pyramidal cell layers of hippocampal slices cut perpendicular to the septo-temporal axis—were selected for this purpose. One advantage offered by these regions includes high cell body density which allows for visualization of the cell layer under a dissecting microscope thus aiding sample placement. Another advantage includes tissue homogeneity in the dimension of the slice perpendicular to the coil face. This property enables shortened scan times due to the ability to decrease through-plane resolution values while minimizing partial volume averaging of different

tissue types. Also, alpha-motor neurons located in the ventral horn of the spinal cord have been selected for investigation. While their size—approximately 50 μ m in diameter—makes them among the largest mammalian cell bodies and therefore the most likely to be resolved by contemporary MRI techniques, it is their proximity to the tissue boundary between white and gray matter in the spinal cord that increases the likelihood of garnering a direct correlation between MRM and light microscope images. Because white and gray matter can be distinguished easily using both histological and MRI techniques, the inclusion of both tissue types should make image coregistration far less ambiguous. In addition to the changes made to our histology protocol and the inclusion of hippocampus and spinal cord to our tissue microstructure studies, diffusion-weighted scan protocols were added to our MRM experiments in an attempt to capitalize on the predicted contrast differences between intracellular and extracellular tissue compartments. Also, diffusion tensor imaging (DTI) was employed in the case of our spinal cord images in an attempt—through tractographic analysis—to delineate myelinated fiber tracts within the slice. While numerous investigators have proposed multi-compartment models to describe the non-monoexponential diffusion signal decay observed in biological tissues, no MR images depicting contrast differences between tissue compartments in mammalian tissue have yet been collected due to resolution limitations (Li et al., 1998; Stanisiz et al., 1997; 1998; Szafer et al., 1995a,b). Based on known histological characteristics of the tissues under investigation and our ability to attain ultra-high resolution MRM images, this work represents—to our knowledge—the first MRM study with the potential to resolve and examine mammalian cellular structure.

Methods

Alterations to Histology and MR Protocols

The histological protocol was essentially unchanged from that which was previously presented (Chapter 2) save for the fact that cryosectioning was abandoned in favor of cutting tissue with a vibratome as a means of better preserving tissue microstructure. The only other significant change involved swapping the order of procedural steps so that tissue was cut into its final slice dimensions prior to MRM or light microscopy imaging. Also, changes to the MR scan protocols included employing diffusion-weighted and diffusion tensor imaging in an attempt to create tissue contrast between cell bodies and their surrounding tissues and generate ultra-high resolution diffusion and tensor data in spinal cord sections respectively.

Transcardial Perfusion Fixation Protocol

Adult, male Sprague Dawley rats (150g) and CD1 mice (50g) were anesthetized via isoflurane inhalation until unconscious and unresponsive to reflexive testing as described previously (Chapter 2). Anesthesia was maintained at 2.5% isoflurane in an oxygen carrier gas throughout the fixation procedure. First, animals were placed in a supine position and an incision was made into the abdominal cavity along the dextro-sinistral axis. Next, access to the heart was achieved by making bilateral incisions from the lateral most ends of the first incision rostrally through the diaphragm and ribcage extending to the top of the thoracic cavity. Following removal of the pericardium, a fourth incision was made into the left ventricle near the interventricular septum. For perfusion fixation of rats, a straight, 16 gauge, ball-tipped gavage needle (FNS-16-3, Kent Scientific) connected to a 1/4" O.D. 1/8" I.D. perfusion line (EW-064008-47, Cole-Parmer) attached to a peristaltic pump (Masterflex® L/S® model 7550-20, Cole-Parmer) was inserted into the incision and advanced through the aortic semilunar valve until the needle tip was visible through the wall of the aortic arch. The needle was then secured

in place using a curved, bulldog-style Johns Hopkins surgical clamp (RS-7441, Roboz). All perfusion lines were primed with injectable saline (2B1322, Baxter Healthcare Corp.) prior to needle placement to avoid introduction of bubbles into the circulatory system. Perfusion of approximately 300ml injectable saline was then initiated at a rate of 75.0ml/min. Immediately after beginning perfusion, a final incision was made in the right atrium to permit exsanguination. Perfusion of saline continued until exsanguination was complete as evidenced by the absence of color from right atrial effluent. Lastly, approximately 300ml of PBS (pH 7.4) containing 4% formaldehyde was perfused through the subject at the same rate prior to gross dissection of the brain and spinal cord. In mice, perfusion fixation was achieved using the same surgical procedure, but saline (60ml) and fixative (60ml) were administered by hand using a straight, 18 gauge ball-tipped gavage needle (FNS-18-2, Kent Scientific) attached to a 60ml syringe (Becton Dickson, 309654).

Staining for Iron Deposition in Immersion and Perfusion Fixed Mouse Striatum

Fixed brains (4% formaldehyde) from aged (>2yr) CD1 mice were bisected along the longitudinal fissure and affixed to a specimen block (10076, Ted Pella Inc.) along the cut surface using Loctite ® 404 tissue adhesive (10035, Ted Pella Inc.). The block and tissue were placed in the specimen bath of a Lancer series 1000 vibratome (8885-054018, Ted Pella) containing PBS adjusted to physiological pH and osmolality (pH = 7.4, osmolality = 300mOsm). Serial sections containing striatal tissue (50µm thick) were collected and stored in fixative prior to histological analysis. Sections of rat spleen were collected in a similar fashion and used as a positive control. To test for the presence of ferric iron, the Perls staining method was employed. Slices were placed in a working solution of 5% potassium ferrocyanide and 5% hydrochloric acid in distilled water for 30min. To test for the presence of ferrous iron, a Turnbull's blue reaction was used.

Slices were placed in a working solution of 1% potassium ferricyanide and 0.5% hydrochloric acid in distilled water overnight (approximately 17h). Following staining, slices were briefly rinsed (ddH₂O) and wet mounted ((41.25% saline (0.9% NaCl with 0.02% sodium azide), 51.5% glycerol, 7.25% gelatin)). Light microscopy images were collected at magnifications of 40X and 200X using an Olympus BH-2 microscope interfaced with a KP-D581 Hitachi digital color camera and processed using software (Image-Pro Plus, V 6.2.1) available from Media Cybernetics.

MRM of Laminar Cell Layers in the Rat Hippocampus

Excised brains from perfusion-fixed, male, Sprague Dawley rats (150g) were dissected into three blocks by making two coronal cuts orthogonal to sagittal and horizontal axes roughly underlying bregma and lambda cranial fissures. Rostral and caudal most brain sections were discarded and the caudal-most face of the medial portion was affixed to a specimen block (10076, Ted Pella Inc.) using Loctite ® 404 tissue adhesive (10035, Ted Pella Inc.). The block and tissue were placed in the specimen bath of a Lancer series 1000 vibratome (8885-054018, Ted Pella) containing PBS adjusted to physiological pH and osmolality (pH = 7.4, osmolality = 300mOsm). Serial sections were collected at 500µm increments. Following sectioning, hippocampi were excised and portions including the entorhinal cortex, subiculum, and fimbria removed by gross dissection to aid in sample placement. Fixed samples were permitted to wash in PBS overnight as a means of reducing formaldehyde in the tissue. After washing, slices were placed in the tissue well of the 200µm or 50µm diameter microsurface coil and oriented with the aid of a dissecting microscope (OPMI 1-FC, Carl Zeiss) such that the pyramidal cell layer of the CA1 region or the granule cell layer of the dentate gyrus overlaid the diameter of the microsurface coil (Figure 3-1). Prior to imaging, the sample was immersed in PBS and sealed in

place using PCR film as described previously (Chapter 2). Spin echo and diffusion-weighted spin echo scans were obtained. Scan series including variable TR (2500, 1000, 500, and 300ms), TE (27.1, 30, 36, 40, and 50ms), and diffusion-weighted ((b = 0 (39 effective), 100, 300, 500, 1000, 2000, 4000, 5000, 6000, 8000, 10,000, 15,000, and 30,000s/mm²)) sequences were also obtained in the CA1 region of the rat hippocampus as a means of calculating T₁, T₂, and ADC values for the pyramidal cell layer and adjacent tissues. This was achieved by using a non-linear least squares fit (Marquardt, 1963) to the equation;

$$S = PD(1 - e^{-TR/T_1})e^{-TE/T_2}e^{-bD} \quad (3-1)$$

Where S is the MR signal taking into account T₁, T₂, and diffusion weighting, PD is the proton density signal, TR and TE are the repetition and echo times respectively, b is the diffusion weighting, and D is the apparent diffusion coefficient.

Calculation of Diffusion-Limited and Bandwidth-Limited Resolution

Limits on image resolution due to the bandwidth, and diffusion during both frequency and phase encoding were calculated for MRM images of both the rat and pig spinal cords using equations 2-2, 2-3, and 2-4 as described previously (Chapter 2).

MRM of the Ventral Horn in the Rat and Pig Spinal Cord

Cords were exposed by spinal laminectomy and tissue from both cervical and lumbar enlargements removed by gross dissection. Transverse sections of perfusion-fixed (rat) or immersion-fixed (pig) cord (4% formaldehyde) were cut in increments ranging from 25μm to 100μm using a vibratome and washed overnight in PBS as described previously (Chapter 3). Portions of the ventral horn were excised and areas containing alpha-motor neurons as well as the boundary between gray and white matter placed directly over the coil face (500μm diameter) with the aid of a dissecting microscope (Figure 3-2). The 50μm surface coil was also used to

collect a 3D gradient echo image of an individual cell body. Due to the fact that the sample well depth (500 μm) exceeded the depth of the tissue slice (25 μm to 300 μm), a tissue retention device developed for the microperfusion system (Chapter 5) was employed to prevent the tissue from shifting and ensure the structures of interest stayed within the coil's excitation profile. The separate pieces of this device which consisted of a nylon mesh insert and nylon retention ring were soaked in PBS overnight prior to use in an attempt to eliminate air bubbles which otherwise tended to become trapped on their surface. After securing the sample in place and adding additional PBS, the tissue well was sealed with PCR film. Diffusion-weighted, spin echo images and 21-direction HARDI acquisitions of rat spinal cord (TR = 2000ms, TE = 36.1ms, $b_{(DWI)} = 4025\text{s/mm}^2$ or 2000s/mm^2 , $b_{(HARDI)} = 3750\text{s/mm}^2$, $\Delta = 17\text{ms}$, $\delta = 6\text{ms}$, geometric slice = 80 μm , resolution = 15.6 μm in-plane, HARDI Avg $b(0) = 60$, HARDI Avg $b(3750) = 30$, DWI scan time = 7h7min or 4h, HARDI acquisition scan time = 49h) along with 21-direction HARDI acquisitions of pig spinal cord (TR = 2000ms, TE = 30.1ms, $\Delta = 17\text{ms}$, $\delta = 6\text{ms}$, $b = 1800\text{s/mm}^2$, tissue slice = 100 μm , resolution = 15.625 μm in-plane, Avg = 10, HARDI acquisition scan time = 15h36min) were acquired using the Oxford 600MHz spectrometer. Mean diffusivity and diffusion orientation maps were generated using MATLAB (The Math Works Inc.) analytical software. Briefly, the diffusion tensor was obtained from a non-linear least squares fit (Marquardt, 1963) to the equation;

$$S/S_0 = \exp(-\bar{b} \cdot \bar{D}) \quad (3-2)$$

Where S is the diffusion-weighted signal, S_0 is the signal without diffusion weighting, \bar{b} is the b-value matrix, and \bar{D} is the diffusion tensor. Eigenvalues (λ_1 , λ_2 and λ_3) and their eigenvectors were then calculated from the diffusion tensor. Next, the apparent diffusion coefficient was calculated using the equation;

$$ADC = (\lambda_1 + \lambda_2 + \lambda_3)/3 \quad (3-3)$$

Where ADC is the apparent diffusion coefficient, and λ_1 , λ_2 , and λ_3 are the calculated eigenvalues of the tensor (\bar{D}). The mean diffusivity map was generated by displaying color-coded, pixel-wise ADC calculations. For our diffusion orientation maps, the in-plane diffusion directions were visualized by plotting the x and y components of the primary eigenvector in each pixel. Diffusion tensor tractography was performed using an adjunct software package (DTI Tools, Freiburg University Hospital, Germany) developed for use with MATLAB. This software uses a method known as fiber assignment by continuous tracking (FACT): a deterministic DTT algorithm (Mori et al., 1999). The criteria for voxel connectivity required angles of incidence between adjacent primary eigenvectors to be less than or equal to 80° . Predicted tracts spanning less than six voxels were excluded from the finalized DTT maps. Thresholding techniques based on calculated fractional anisotropy values which are commonly employed as exclusionary criteria were not used in our analysis. Following MR imaging, slices were Nissl stained and photographed as described previously (Chapter 1) to provide correlative histological data.

Results

Alterations to Histology and MR Protocols

Tissue sectioning prior to image analysis yielded the first directly correlative data between MR and light microscopy images. Descending white matter tracts in the striatum were visualized separately in both 3D gradient echo MRM images and Nissl-stained histology images (Figure 3-3). Slight variation in the positioning of individual tracts is evident between the images due to differences in tissue compression between experiments as well as differences— $16\mu\text{m}$ as compared to $50\mu\text{m}$ —in through-plane tissue depth. While Nissl-stained cell bodies are clearly visible in the histology image, no corresponding tissue structures are evident in the MR image.

Alterations to the histology protocol coupled with changes to the MR protocol which involved employing diffusion-weighted scans also made possible the imaging of tissue structures which possess dimensions smaller than the thinnest permissible geometric slice (Figure 3-4).

Staining for Iron Deposition in Immersion and Perfusion Fixed Mouse Striatum

At low magnification (40X), Perls and Turnbull's blue staining did not reveal obvious deposits of ferric or ferrous iron in our formaldehyde-fixed striatal sections regardless of the fixation protocol employed (Figure 3-5). In the highest magnification images collected (200X), striatal cell bodies are clearly visible but no iron precipitate within the boundaries of the cell bodies can be seen (Figure 3-6). It is possible however that light staining exists in immersion fixed samples which localizes to areas of vasculature. As all tissue regions under investigation are known to contain varying amounts of iron and iron-containing molecules, we must conclude that these basal levels were not sufficient to elicit a positive response from our staining protocols.

MRM of Laminar Cell Layers in the Rat Hippocampus

Contrast between tissue laminae containing primarily cell bodies—the granule cell layer (Figure 3-7) and the pyramidal cell layer (Figures 3-8 and 3-9)—and laminae consisting mainly of axons, dendritic arbors, interneurons, and astrocytes is evident in both traditional spin echo and diffusion-weighted spin echo images. Portions of the hippocampal slice exhibiting these layers of tightly packed cell bodies appear hypointense as compared to adjacent tissue laminae. In the case of the hippocampus' CA1 region, calculated T_1 , T_2 , and ADC values for the stratum oriens, pyramidal cell layer, and stratum radiatum are summarized (Table 3-1).

Calculation of Diffusion-Limited and Bandwidth-Limited Resolution

For the scan parameters employed in our MRM images of the rat and pig spinal cords ($G_{\text{phase}} = 650.63\text{mT/m}$, $G_{\text{read}} = 591.49\text{mT/m}$, acquisition time = 5.12ms) when using an apparent diffusion coefficient ($1.0\mu\text{m}^2/\text{ms}$) representative of diffusion rates equal to or exceeding the

uppermost values expected for healthy neural tissues, the resolution limits due to the bandwidth, diffusion during frequency encoding, and diffusion during phase encoding were calculated to be $3.88\mu\text{m}$, $4.81\mu\text{m}$, and $4.02\mu\text{m}$ respectively. These values were well under our lowest nominal resolution ($7.8\mu\text{m}$) for these scans indicating that no adjustments to the reported digital resolution were necessary.

MRM of the Ventral Horn in the Rat and Pig Spinal Cord

Preliminary 3D gradient echo images (TR = 300ms, TE = 5ms, resolution = $8\mu\text{m}$ isotropic) taken in the rat spinal cord revealed a small number of discrete, hypointense tissue structures (Figure 3-10). While these structures exhibited similar contrast to the unidentified microstructural elements in our striatum images (Chapter 2) they differed significantly in that they were both more sparsely distributed and larger: $30\mu\text{m}$ to $50\mu\text{m}$ in diameter as compared to $10\mu\text{m}$ to $15\mu\text{m}$. In subsequent studies on the rat spinal cord which employed both thinner tissue slices ($25\mu\text{m}$ to $50\mu\text{m}$) and diffusion-weighted imaging protocols, alpha-motor neurons were visualized in our diffusion-weighted ($b = 4025\text{s/mm}^2$, $\Delta = 17\text{ms}$, $\delta = 6\text{ms}$, geometric slice thickness = $80\mu\text{m}$, res. = $7.8\mu\text{m}$ in-plane, acquisition time = 7h7min) MRM images (Figures 3-10, B and 3-11, B). These structures were positively identified by means of correlative histology (Figures 3-11, A/C/D and 3-12, A) using landmarks such as the white and gray matter tissue boundary, spatial positioning of the cell bodies and axon bundles, and morphological characteristics of the alpha-motor neurons' perikarya. Using the smallest diameter microsurface coil ($50\mu\text{m}$) an image of a single alpha-motor neuron cell body was collected (Figure 3-13). This image featured the highest isotropic resolution ($6\mu\text{m}$) obtained on an alpha-motor neuron during this study and, as such, is the only image which displayed heterogeneous signal contrast within the boundaries of the cell body. Analysis of 21-direction HARDI acquisition data of a fixed,

spinal cord slice from a rat cervical enlargement yielded mean diffusivity, diffusion orientation, and tractography maps that correlated well with microstructural elements within the tissue being investigated (Figure 3-14). The mean diffusivity map (Figure 3-14, B) illustrated higher rates of diffusion occurring within the perikarya of alpha-motor neurons—ADC values ranging between $0.8 \mu\text{m}^2/\text{ms}$ and $1.1 \mu\text{m}^2/\text{ms}$ —than those observed in the tissues surrounding them. Diffusion orientation and tractography maps illustrated highly anisotropic diffusion occurring within myelinated axon bundles and a high degree of intervoxel connectivity dependent on the continuity of these fiber tracts respectively (Figure 3-14, C/D). Similar results were observed—i.e. visualization of alpha-motor neurons and axon bundles—from fixed sections of rat spinal cord taken from the lumbar enlargement (Figure 3-15). Lastly, diffusion-weighted MRM images taken in the ventral horn of spinal cord enlargements from the pig (Figure 3-16) illustrate higher apparent diffusion rates occurring within alpha-motor neuron cell bodies than those seen in surrounding tissues.

Discussion

Age-Dependent Iron Deposition in the Basal Ganglia

Our histological staining protocols did not reveal the presence of iron within the cell bodies of formaldehyde-fixed striatum samples from aged mice. This observation suggests that if the hypointense signal is indeed localized within cellular structure, there should be an explanation for the MR signal contrast displayed that does not rely exclusively on the presence of iron sequestered within the cell body. Conversely, it is also possible that T2*-weighting in our MR images due to susceptibility effects was more sensitive to the presence of cellular iron than our tissue staining methods. While our histology suggests that iron sequestered in cells is not responsible for the signal voids in our striatal images, it is still possible that the hypointense signal regions displayed in our images resulted from iron present in haemoglobin as there does

appear to be light Perls staining within portions of the vasculature in immersion fixed samples. While we cannot rule out the possibility that vascular iron contributed to the signal contrast present within our striatal images, we believe that it is highly unlikely that the majority of hypointense signal regions are caused by iron-induced susceptibility artifacts. Morphological evidence suggests the structures under consideration are highly concentrated in the striatal tissue and, more importantly, of a relatively uniform shape and size: spheroids approximately 10 μ m to 15 μ m in diameter. Blood pools trapped in the striatal tissue appear to be more sparsely distributed and differ somewhat in size and shape depending on the structural characteristics of the vessels in which they became trapped. Because gradient echo imaging was employed in our preliminary MRM experiments, we would expect these structural differences—which are obvious even in histological images—to be increased several times in our MRM images due to the characteristic of gradient echo imaging to magnify the effects of localized magnetic field inhomogeneities. Therefore, if the described hypointense contrast were due exclusively to the iron contained within blood pools, we would expect the areas of hypointense signal to be far less uniform in size and shape as well as far less ubiquitous throughout the striatal tissue. Given these findings, our subsequent studies focused on identifying other potential sources for the observed signal contrast.

MRM of Laminar Cell Layers in the Rat Hippocampus

The results of our analysis on multiple layers of rat hippocampus repeatedly illustrate that MR contrast exists between laminae composed primarily of cell bodies and laminae composed of other cellular components such as axons, dendrites, interneurons, and astrocytes. Most importantly, the described contrast differences are apparent when employing diffusion based contrast mechanisms which can be used to study changes in the micro structural environment of

biological tissues as it relates to normal physiology or pathological processes. While the low through-plane resolution employed in our scan protocols coupled with the close proximity of cell bodies in the hippocampal laminae made visualization of individual cell bodies in these tissues impossible, our prescience of the hippocampal microstructure under investigation allowed us to tailor scan parameters to generate this contrast as well as reveal to us what image contrast to expect from single cells. These experiments also revealed that cell bodies are capable of exhibiting hypointense signal contrast in non diffusion-weighted images thus revealing the possibility that at least a portion of the microstructures observed in our striatal images could have cellular origins. In our experience, diffusion-weighted images generated the most reproducible image contrast between cells and surrounding tissue structures and cells in these images always appeared dark suggesting higher rates of intracellular diffusion. As such, subsequent experiments attempting visualization of individual alpha-motor neurons in the spinal cord employed diffusion-weighted and diffusion tensor scans almost exclusively.

MRM of the Ventral Horn in the Rat and Pig Spinal Cord

Diffusion-weighted MRM scans of the cervical or lumbar enlargement's ventral horn revealed that MR contrast exists between cell bodies and their surrounding tissues. These findings were demonstrated in both the rat and pig and reproduced in the rat to demonstrate that the reported contrast was not species or subject specific respectively. To our knowledge, this work represents the first instance in which mammalian cells were visualized using MRI technology. Also, it may be the first study to describe contrast heterogeneity within mammalian cells resulting from cytoplasmic and nuclear compartmentation; however, direct correlative evidence of this finding was not forthcoming. Some may argue that mammalian cells have been visualized with MRI before in studies employing various sizes and concentrations of iron-oxide particles incorporated into cells (Shapiro et al., 2004). Iron-oxide particles create susceptibility

artifacts in MR images which manifest as hypointense signal regions and, when incorporated into cells, can be very useful for cell localization and tracking; however, this technique does not constitute true cellular imaging because it offers no insight into the structural characteristics responsible for the origin of MR signal at the cellular level. Conversely, images provided in the present work are representative of the native MR contrast which exists naturally between cell bodies and the tissues that surround them. Having the ability to detect such contrast at or beyond the resolutions needed to resolve cellular tissue structure is not trivial in that a multitude of the most devastating neurological diseases manifest at the cellular level. Alzheimer's disease (AD), being one example, has been shown to have rates of clinical misdiagnosis as high as 12% and rates where AD was found to be only partially responsible for disease symptoms of an additional 22% (Foy et al., 2007). Even more relevant to the current study, amyotrophic lateral sclerosis (ALS)—primarily viewed as a neurodegenerative disease affecting motor neurons in the brain and spinal cord—is also difficult to accurately diagnose (Turner et al., 2009). Like all diseases of the central nervous system, AD and ALS do not lend themselves to diagnostic biopsy. Most importantly, both are diagnosed by observation of disease-specific symptomatology which occurs long after the initial stages of tissue degradation begin to take place. This means that, regardless of diagnostic accuracy, once a patient is diagnosed with a CNS disease such as AD or ALS, the period of time in which the most efficacious treatment may be administered—known as the therapeutic window—has long since passed. These observations highlight the current need for diagnostic protocols of CNS diseases that are noninvasive, accurate, and can produce positive results prior to the onset of irreversible tissue damage. While the methods used to obtain MRM images of cell bodies in this study cannot currently be used for diagnostic clinical medicine, they have demonstrated that tissue microstructure can be observed using native contrast MRM. It is

our hope that data from subsequent studies which focus more intently on how pathological changes occurring at the cellular level affect the MR signal can be extrapolated through ever more accurate models of tissue behavior as a means of detecting those same changes in scans conducted at clinical field strengths.

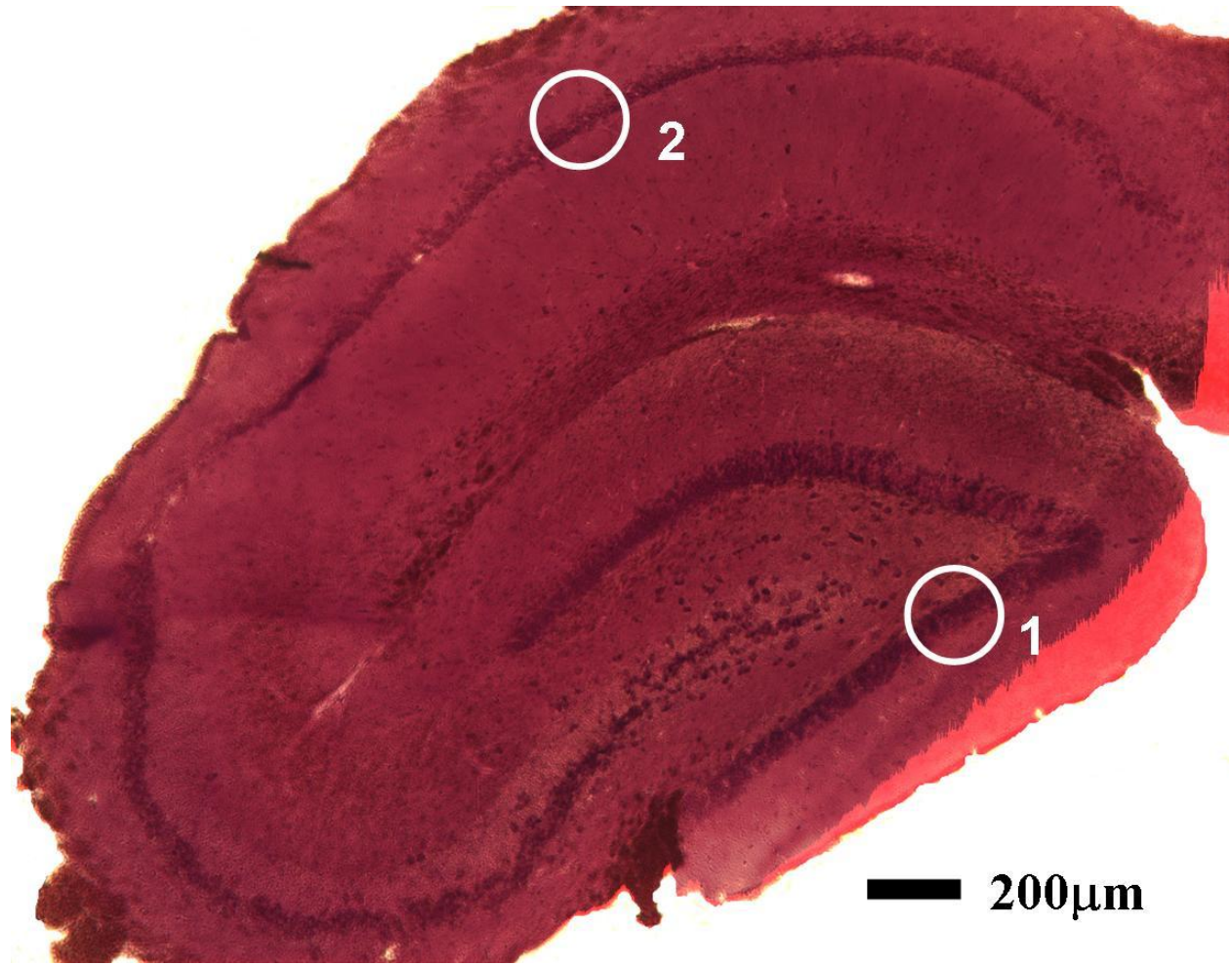


Figure 3-1. Nissl-stained rat hippocampus (100µm thick) illustrating laminar organization of cellular populations in slices taken perpendicular to the septo-temporal axis. White circles are representative of 200µm diameter microsurface coil placement during MR experiments in which the granule cell layer (1) and pyramidal cell layer (2) were imaged.

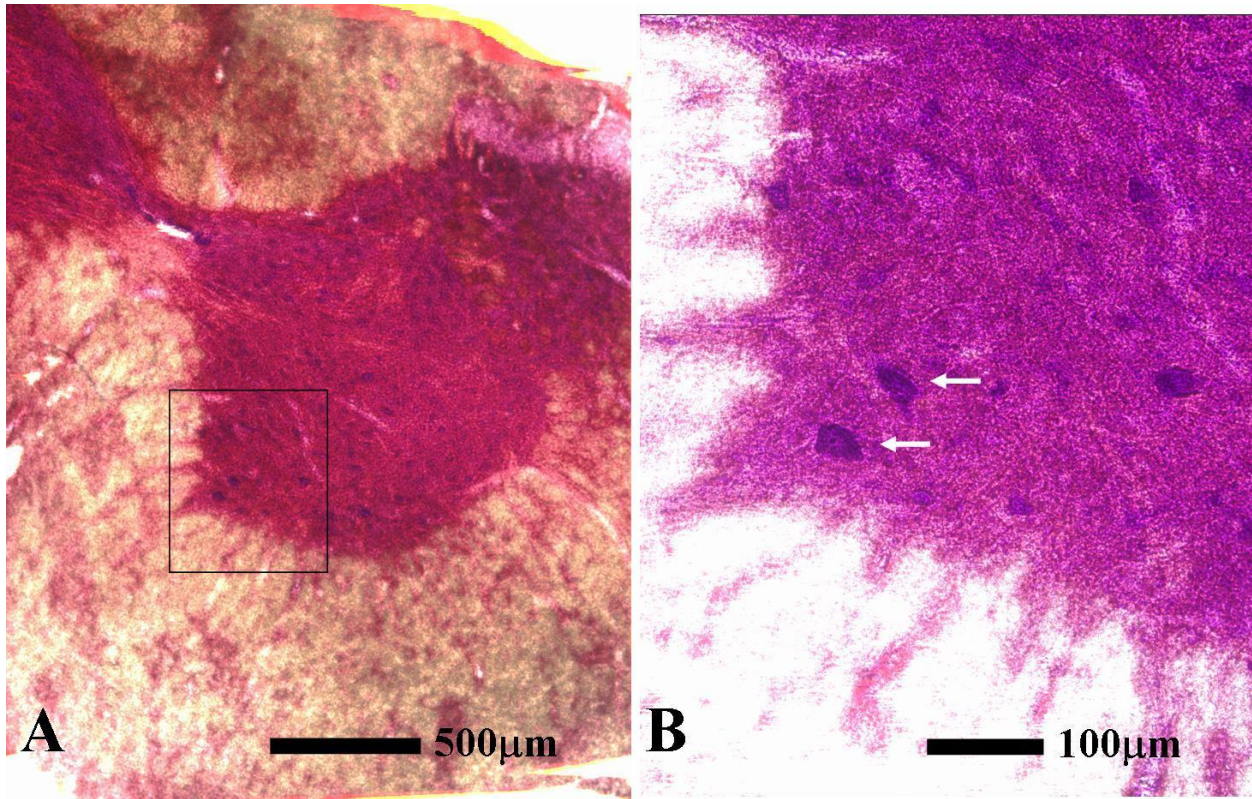


Figure 3-2. Nissl-stained section of the rat spinal cord taken from the cervical enlargement illustrating microstructural elements along the boundary of the ventral horn. A) Nissl-stained histology section (50µm thickness, 50X magnification) through the cervical spinal cord enlargement showing roughly half of this cross section's tissue structure. Gray matter is distinguishable by its elevated level of Nissl staining resulting in a darker appearance as compared to the surrounding white matter. B) Higher magnification (200X) image of the box insert pictured in (A). Cell bodies of alpha-motor neurons (arrows) are visualized at the base of the ventral horn in close proximity to the border between white and gray matter.

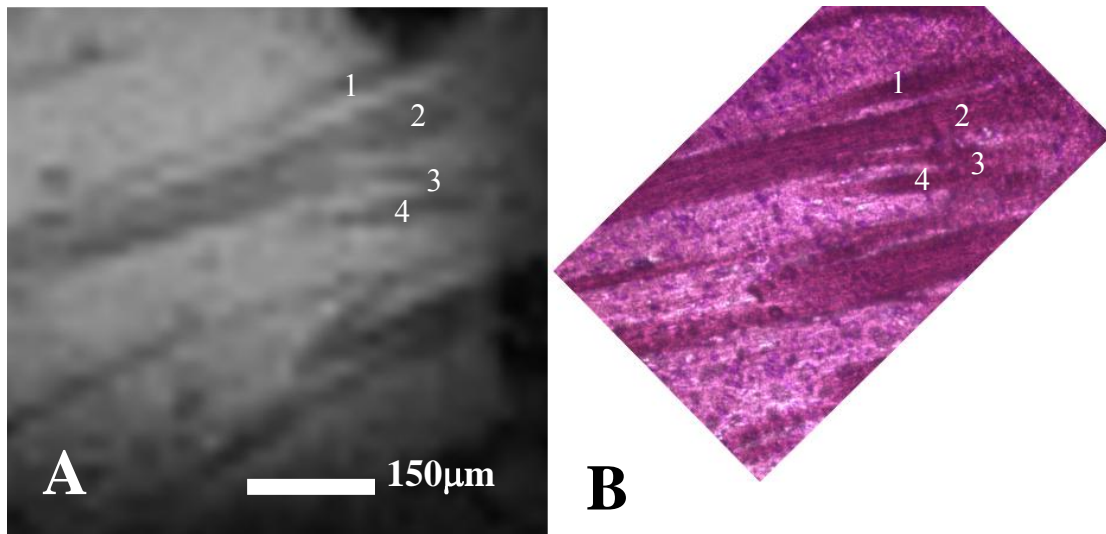


Figure 3-3. Direct correlation of descending white matter tracts in MRM and Nissl-stained histology images of the striatum. A) 3D gradient echo image (16µm isotropic resolution, TR = 300ms, TE = 10ms) taken in the rat striatum using the 500µm diameter microsurface coil. Individual white matter tracts consisting of bundled axons are labeled 1 through 4. B) Correlative, Nissl-stained cryosection (50µm thickness) of the same striatal slice containing the white matter tracts visualized in (A).

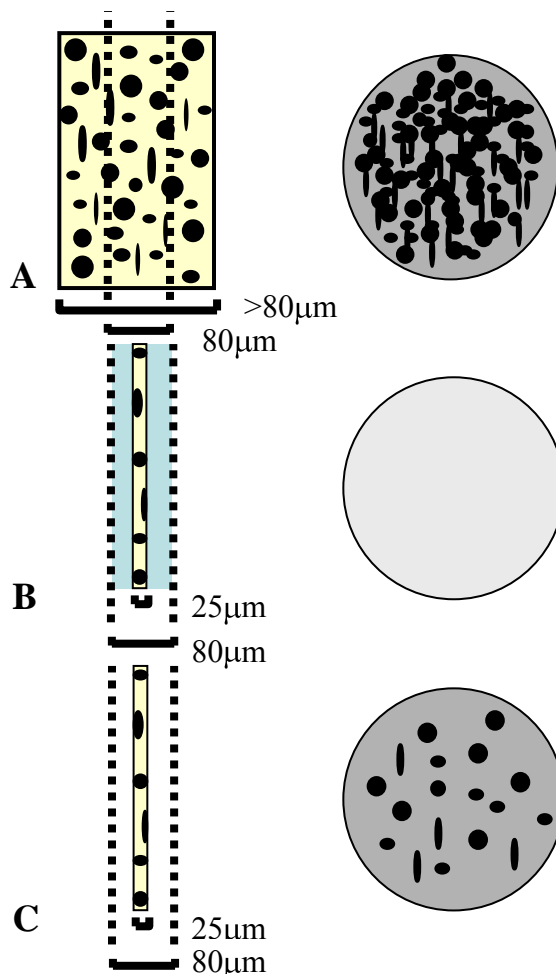


Figure 3-4. Schematic illustration depicting the combined protocol elements necessary to obtain MRM images with separate and distinguishable cell bodies. Tissue slices (yellow) which contain cell bodies (black dots) are viewed along their thinnest edge representative of the slice thickness employed. Dashed lines represent the thinnest geometric slice ($80\mu\text{m}$ = voxel depth) permissible using our diffusion-weighted scan protocol. Large circles represent MRM images generated with the scan conditions immediately preceding them. A) Diffusion-weighted scan protocol employing a tissue slice greater than the thinnest permissible geometric slice. Cell bodies which overlap in the horizontal plane of the page are subject to volume averaging resulting in an MRM image that contains overlapping, indistinguishable cells. B) Spin echo protocol absent of diffusion weighting which employs a tissue slice depth ($25\mu\text{m}$) equal to or less than the diameter of a single alpha-motor neuron cell body. While the reduced slice thickness ensures no overlap of cell bodies within imaging voxels, water protons in the PBS surrounding the tissue slice are not excluded leading to an MRM image dominated by water signal and devoid of tissue contrast. C) Protocol employing both elements—diffusion weighting and reduced slice thickness respectively—of (A) and (B). Water signal from the PBS surrounding the tissue slice is eliminated at high b-values ($b \geq 2000\text{s/mm}^2$) resulting in MRM images containing discrete cell bodies.

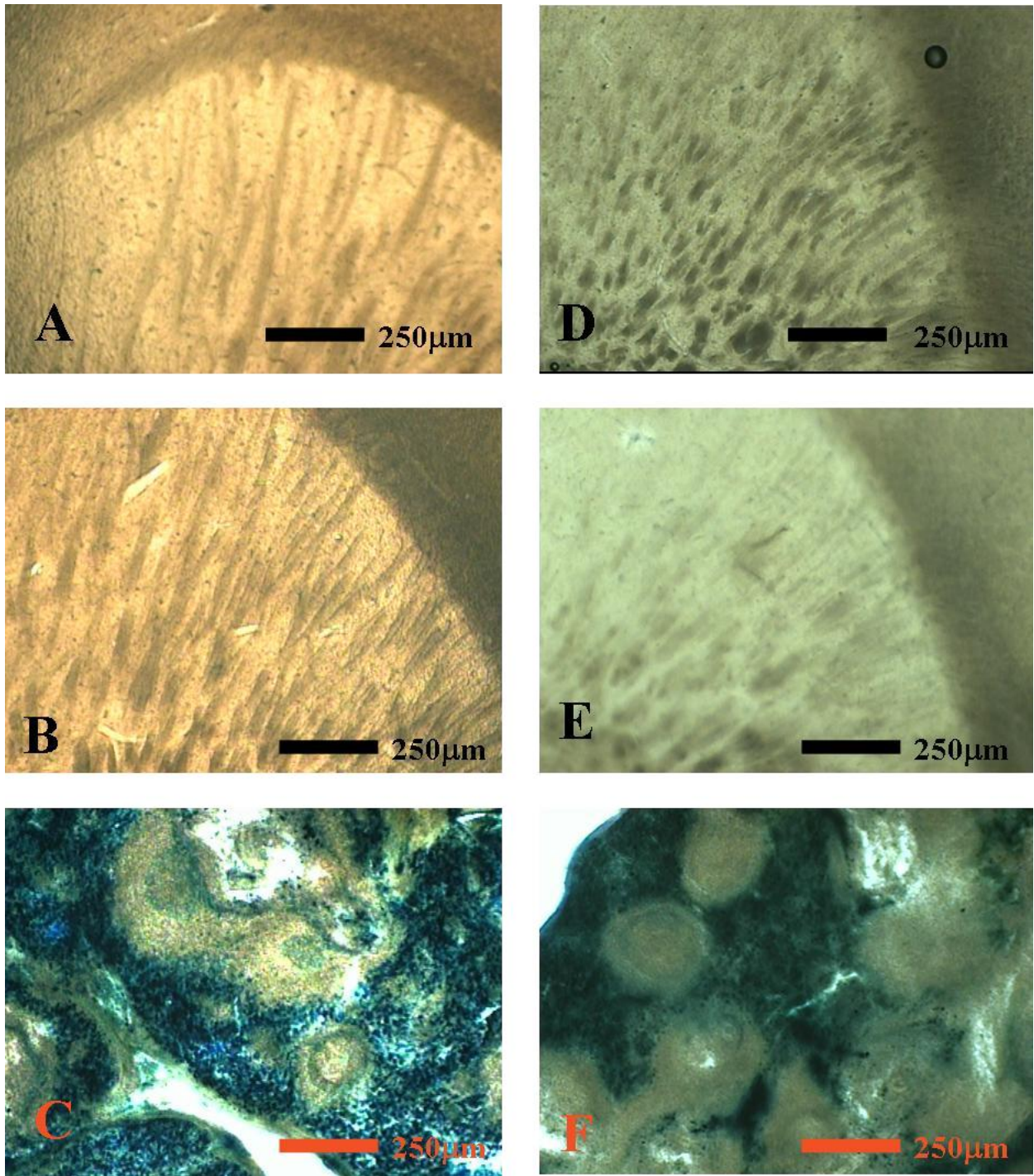


Figure 3-5. Staining for ferric and ferrous iron in the aged mouse striatum. Immersion fixed (panels A and D) and perfusion fixed (panels B and E) striatum from aged (>2yr) CD1 mice and immersion fixed spleen (panels C and F) from Sprague Dawley rats. Images demonstrate results of Turnbull's blue staining (panels A, B and C) for ferrous iron and Perls staining (panels D, E and F) for ferric iron. Both ferric and ferrous iron are present in the spleen (blue precipitate) used as positive controls but less evident in striatal tissues. Slices are 50 μ m thick taken at 40X magnification.

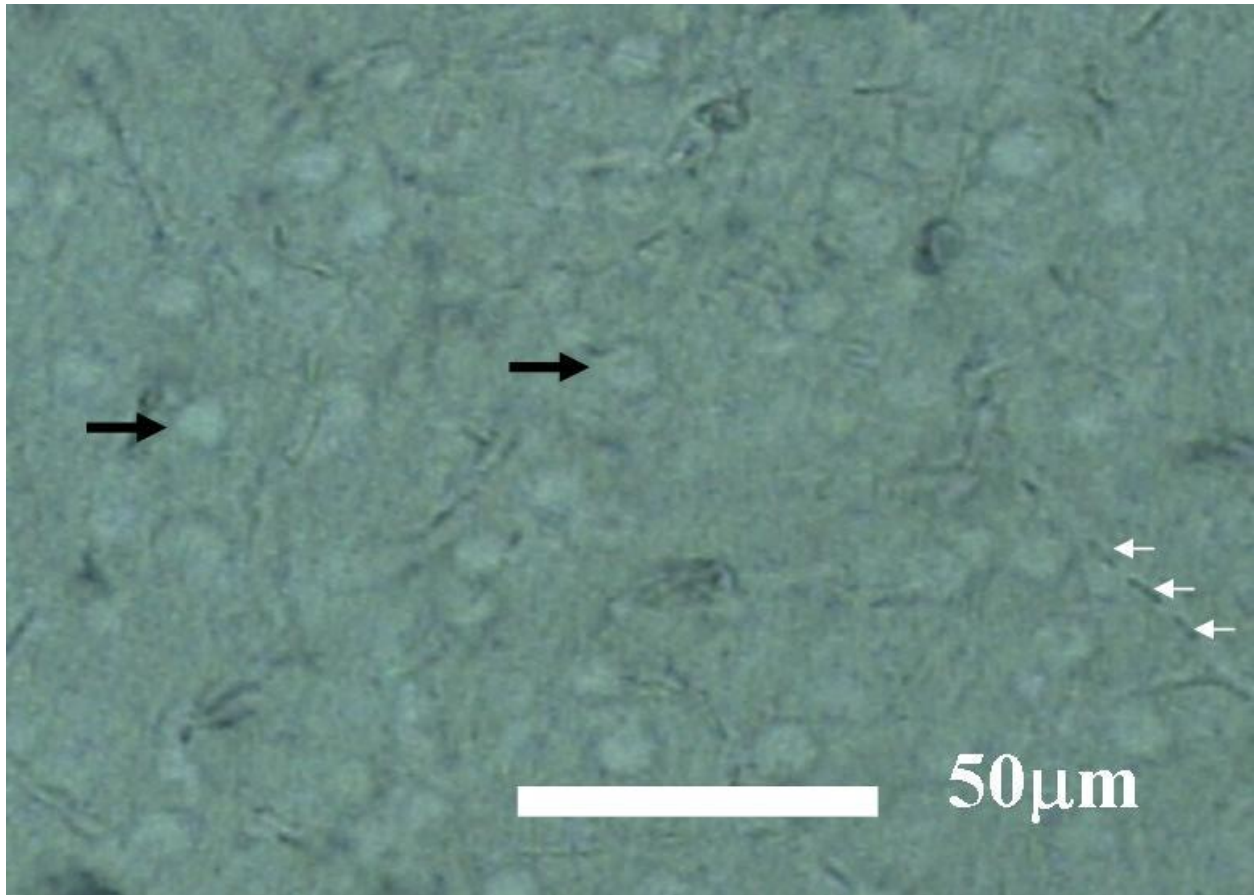


Figure 3-6. High magnification (200X) image of cell bodies (black arrows) in the immersion fixed, aged (>2yr) CD1 mouse striatum following Perls staining for ferric iron. Precipitate indicative of the presence of ferric iron is not evident within the boundaries of the cell bodies; however, light staining is present (white arrows) localized within the boundaries of vasculature.

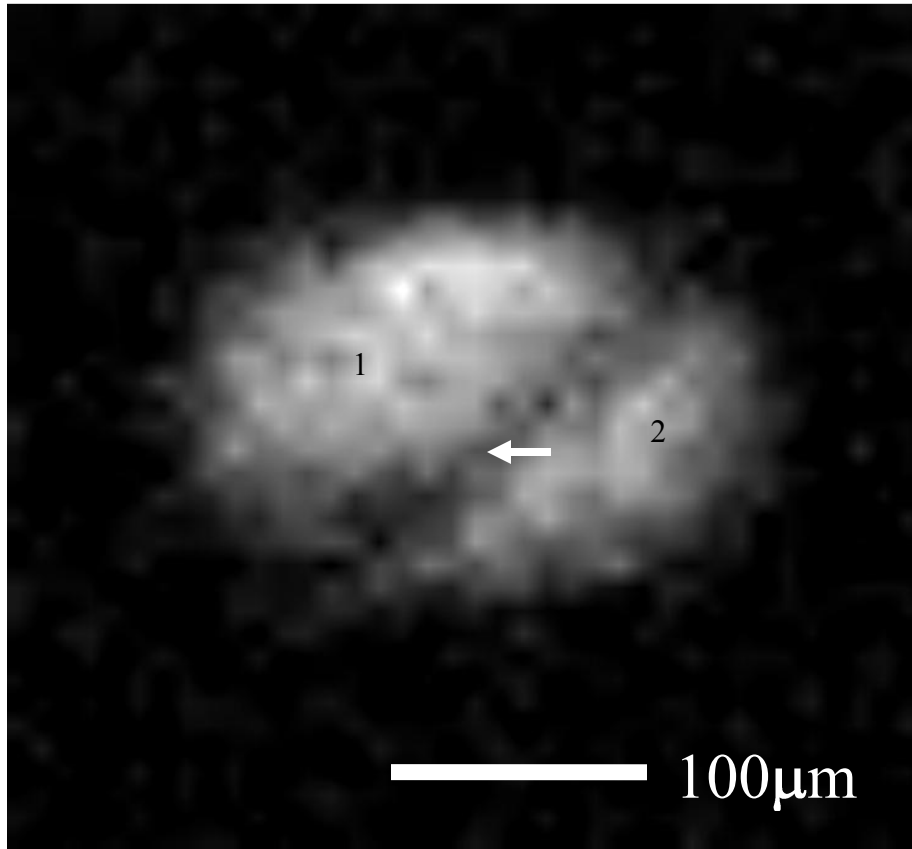


Figure 3-7. Diffusion-weighted spin echo image (TR = 500ms, TE = 26.1ms, $b = 3000\text{s/mm}^2$) of the granule cell layer (arrow), hilum (1), and molecular layer (2) in the dentate gyrus of the rat hippocampus (500µm slice thickness) imaged with the 200µm diameter microsurface coil. The cell layer containing perikarya of granule neurons appears dark in contrast to the surrounding tissues.

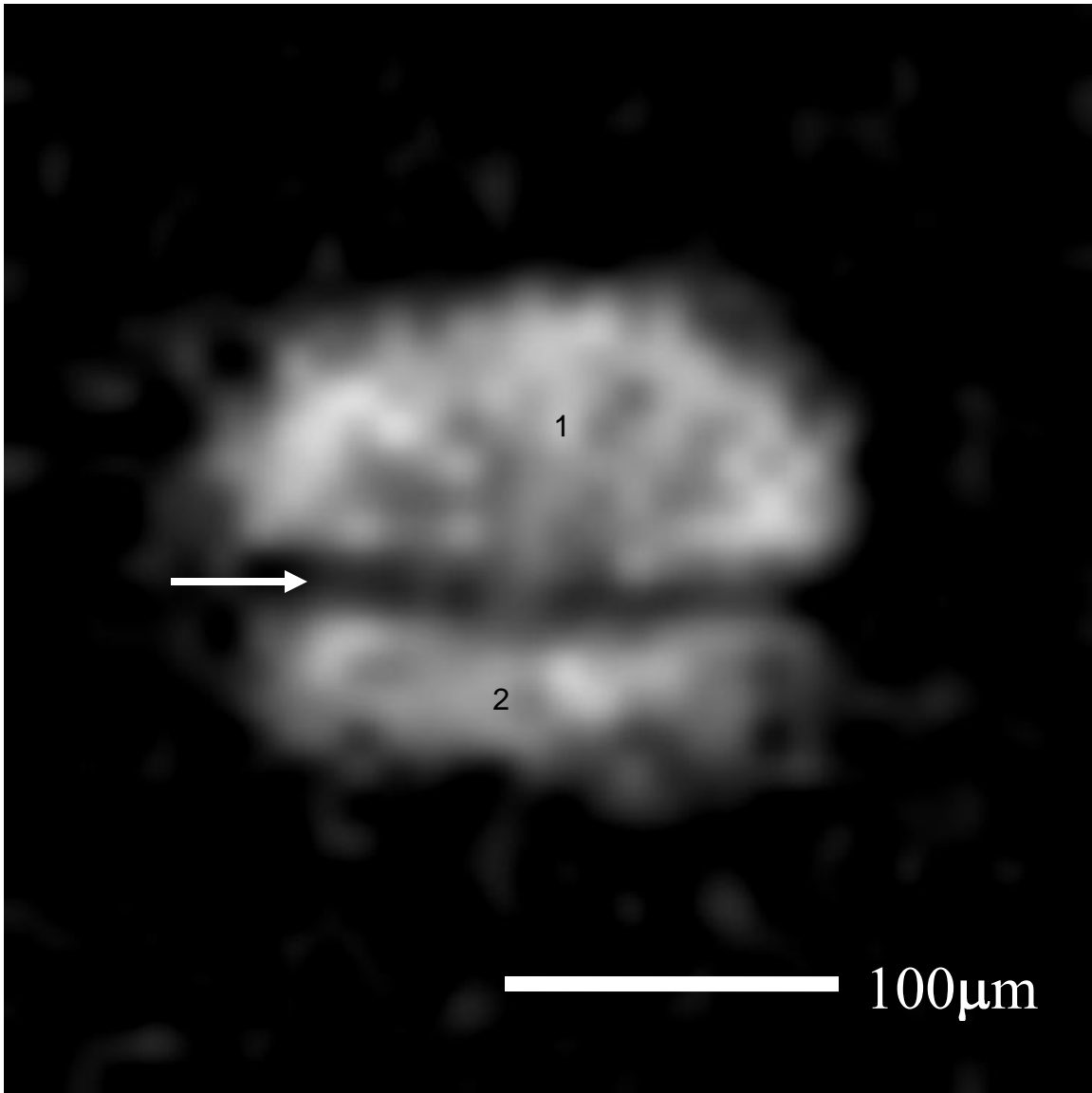


Figure 3-8. Spin echo image (TR = 150ms, TE = 10ms, 8 μ m isotropic resolution) of the pyramidal cell layer (arrow), stratum oriens (1), and stratum radiatum (2) in the CA1 region of the rat hippocampus taken with the 200 μ m diameter microsurface coil. The cell layer containing perikarya of pyramidal neurons appears dark in contrast to the surrounding tissues.

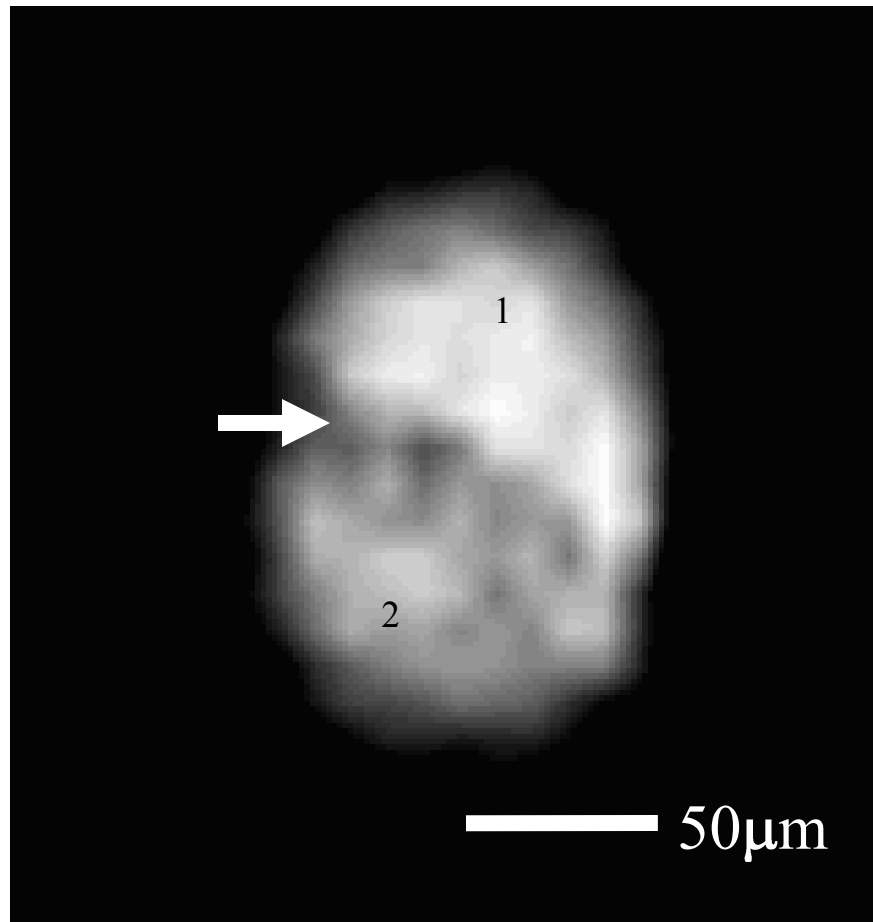


Figure 3-9. Diffusion-weighted spin echo image ($b = 1500\text{s/mm}^2$, resolution = $15.5\mu\text{m}$ in-plane) of the pyramidal cell layer (arrow), stratum oriens (1), and stratum radiatum (2) in the CA1 region of the rat hippocampus taken with the $50\mu\text{m}$ diameter microsurface coil. The cell layer containing perikarya of pyramidal neurons appears dark in contrast to the surrounding tissues.

Table 3-1. Estimated T₁, T₂, and apparent diffusion coefficient values for tissue laminae in the CA1 region of fixed rat hippocampus. Values based on spin echo scan protocols employing variable TR (2500, 1000, 500, and 300ms), TE (27.1, 30, 36, 40, and 50ms), and diffusion weighting ((b = 0 (39 effective), 100, 300, 500, 1000, 2000, 4000, 5000, 6000, 8000, 10,000, 15,000, and 30,000s/mm²)) scan parameters.

	Stratum Oriens	Pyramidal Cell Layer	Stratum Radiatum
T ₁ (ms)	934.0	579.0	755.0
T ₂ (ms)	93.6	19.7	111.0
ADC (x10 ⁻⁴ mm ² /s)	1.0	1.9	0.52

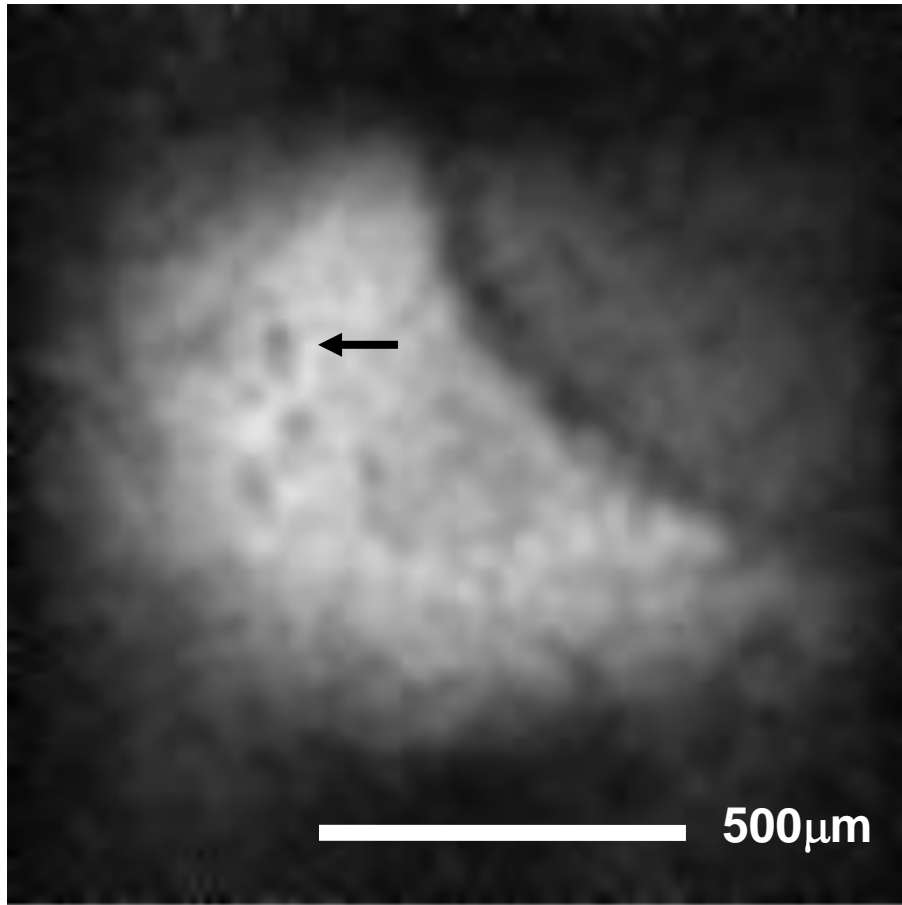


Figure 3-10. 3D gradient echo image (TR = 300ms, TE = 5ms, resolution = $8\mu\text{m}$ isotropic) taken in the ventral horn of the rat from a cross section originating in the cervical spinal cord enlargement. Although the border between white and gray matter is not visible in this image, hypointense structures (arrow) in an image area corresponding to the spinal cord gray matter are present. These structures are equivalent in size ($30\mu\text{m}$ to $50\mu\text{m}$) to perikarya of alpha-motor neurons.

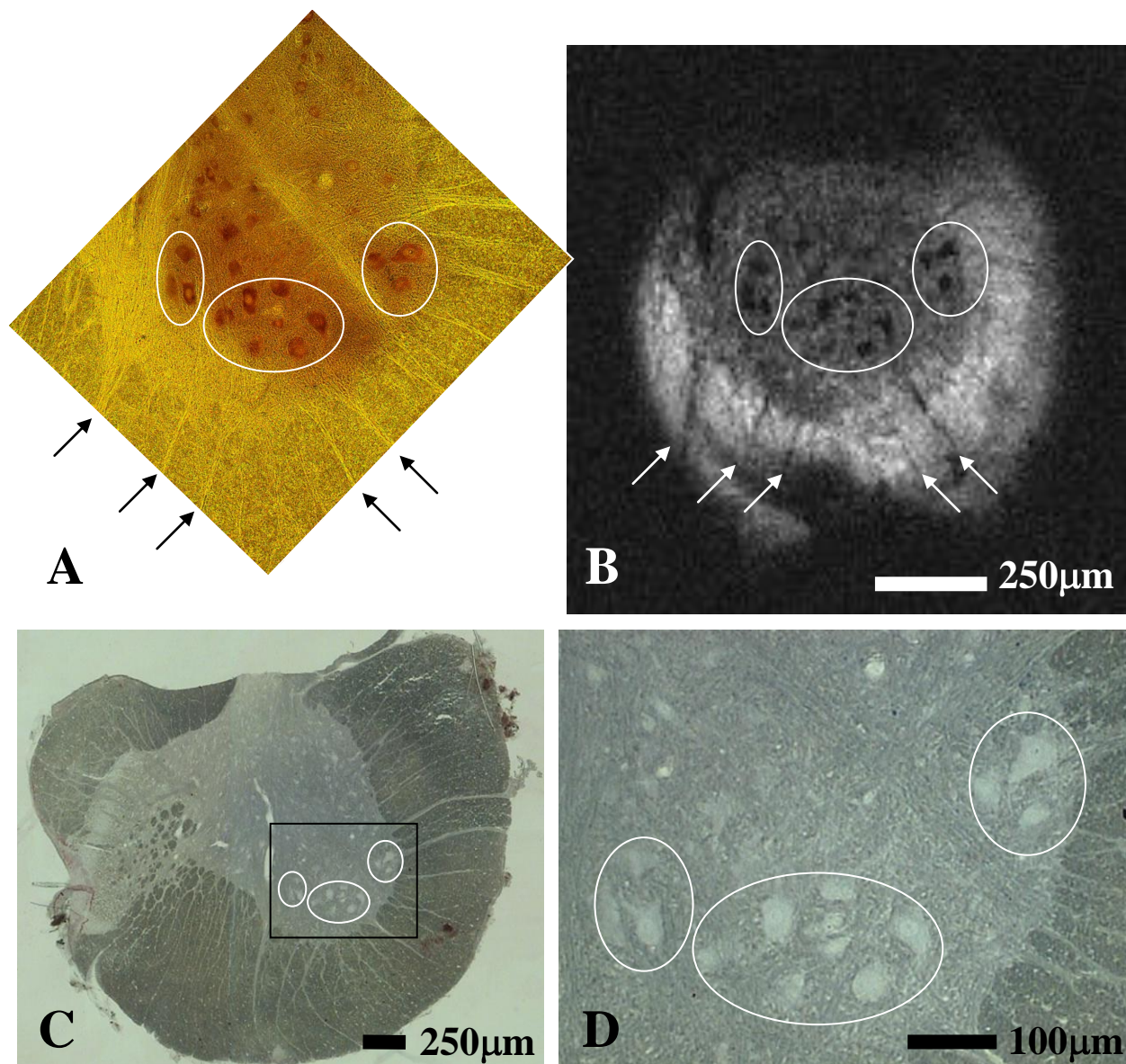


Figure 3-11. Direct correlation of mammalian cell bodies in MRM and histology images. A) Nissl-stained histological section (25µm thick, 100X magnification) illustrating three groupings (ellipses) of nucleated, alpha-motor neuron cell bodies in the ventral horn of the rat spinal cord. A false-color capture was used to enhance tissue contrast. Axon bundles (arrows) are also visible. B) Diffusion-weighted spin echo MRM scan (TR = 2000ms, TE = 36.1ms, b = 4025s/mm², Δ = 17ms, δ = 6ms, geometric slice = 80µm, resolution = 7.8µm in-plane, Avg = 50, scan time = 7h7min) of the same tissue slice imaged in (A). Structures including groups of hypointense perikarya of alpha-motor neurons (ellipses), the ventral horn's tissue boundary, and axon bundles (arrows) projecting into the spinal cord white matter are apparent. All tissue structures present in the histology image correspond unambiguously with structures visualized in the MRM image. C) True color (RGB) tiled histology image of the bisected spinal cord segment. D) Higher magnification image of the box insert in (C).

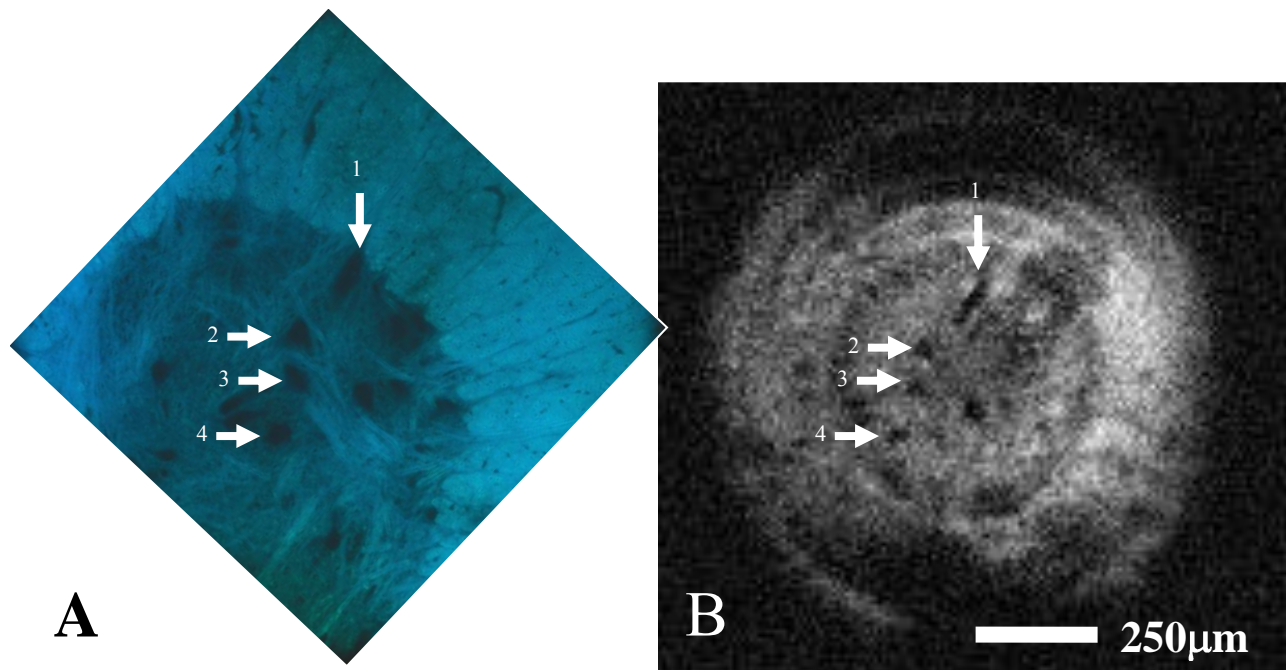


Figure 3-12. Direct correlation of mammalian cell morphology in MRM and histology images. A) Nissl-stained histological section (25 μ m thick, 100X magnification) illustrating multiple alpha-motor neuron cell bodies (numbered arrows) in the ventral horn of the rat spinal cord. A false-color capture was used to enhance tissue contrast. B) Diffusion-weighted spin echo MRM scan (TR = 2000ms, TE = 36.1 ms, b = 2000s/mm², Δ = 17ms, δ = 6ms, geometric slice = 80 μ m, resolution = 7.8 μ m in-plane, Avg = 28, scan time = 4h) of the same tissue slice imaged in (A). While the boundary between white and gray matter is unclear in the MRM data, cell bodies of alpha-motor neurons correlate spatially in both images. Of particular note is the morphological similarity of the cell bodies reproduced between images. The uppermost alpha-motor neuron (1) is rod shaped while the second labeled cell body (2) has a triangular shape.

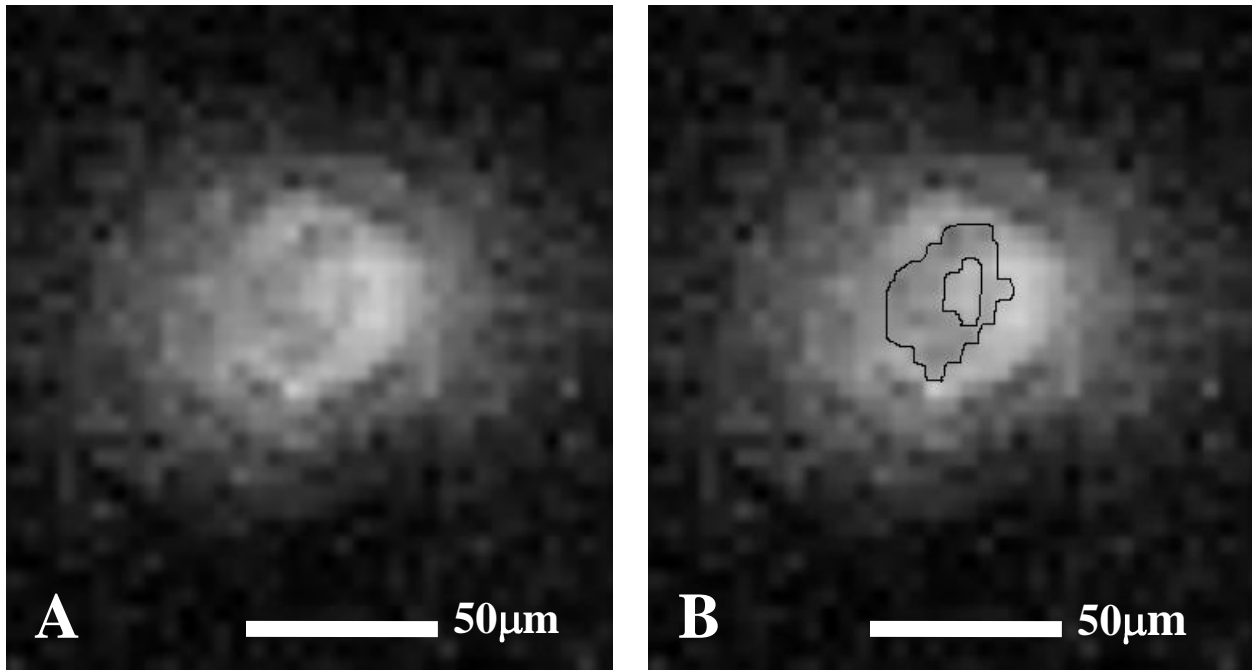


Figure 3-13. Image illustrating MR signal heterogeneity within the cell body of a single alpha-motor neuron. A) 3D gradient echo image (TR = 300ms, TE = 5ms, resolution = $6\mu\text{m}$ isotropic) taken in the rat spinal cord of an individual alpha-motor neuron's cell body acquired with the $50\mu\text{m}$ diameter microsurface coil. Note the heterogeneous nature of signal intensities contained within the boundaries of the perikarya. B) Hand segmented version of (A) in which the areas of differing contrast have been highlighted.

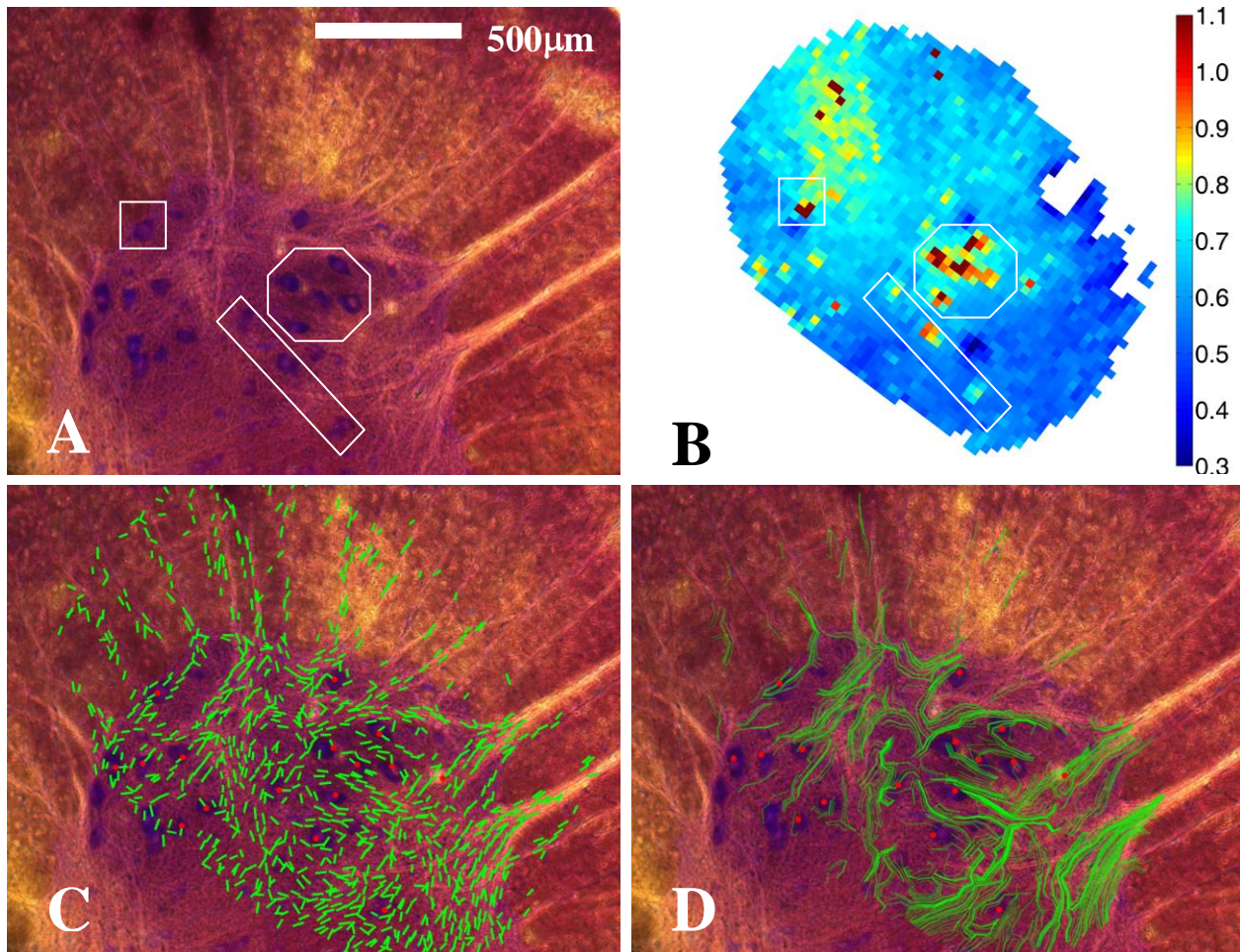


Figure 3-14. ADC, diffusion orientation, and tractography maps generated from 21-direction HARDI acquisitions ($TR = 2000\text{ms}$, $TE = 36.1\text{ms}$, $b = 3750\text{s/mm}^2$, $\Delta = 17\text{ms}$, $\delta = 6\text{ms}$, geometric slice = $80\mu\text{m}$, resolution = $15.6\mu\text{m}$ in-plane, Avg $b(0) = 60$, Avg $b(3750) = 30$, scan time = 49h) of a transverse spinal cord slice from the cervical enlargement of a rat with accompanying correlative histology. A) Nissl-stained histology section ($50\mu\text{m}$ thick) illustrating three groups (white polygons) of nucleated alpha-motor neurons (dark purple) in the ventral horn of the rat spinal cord. Axon bundles radiating from the gray to white matter are also clearly visible. B) Mean diffusivity map of the cell groupings pictured in (A). Perikarya of alpha-motor neurons exhibit higher apparent diffusion than surrounding tissues. The colorbar insert displays ADC calculations ($\mu\text{m}^2/\text{ms}$) for each pixel within the MRM DTI data. C) Graphical overlay of diffusion orientation map (green bars) on the histology image pictured in (A). The shortest vector components were removed from the orientation map for clarity. D) Graphical overlay of diffusion tensor tractography data (green tracts) calculated using the FACT algorithm on the histology image pictured in (A). Images in (C) and (D) were coregistered using the spatial coordinates of cell bodies (red dots) recorded from the mean diffusivity map in (B). The correlation between DTI data, DTT, and histology, while not flawless, is clearly evident upon viewing the graphic overlays from these experiments.

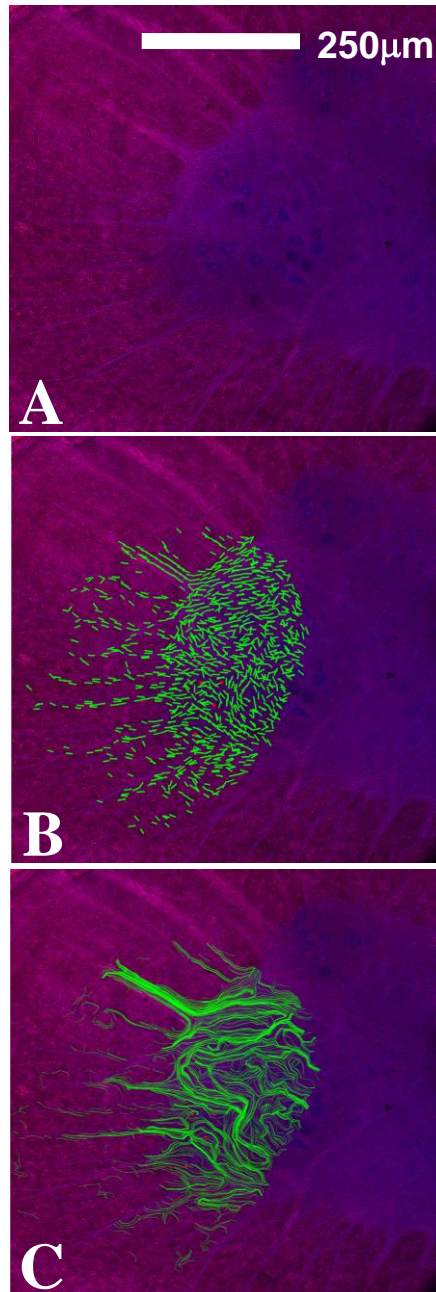


Figure 3-15. Series of Nissl-stained histology images of a fixed, transverse section from the lumbar enlargement of a rat spinal cord including overlays featuring DTI and DTM analysis. Scan parameters were equivalent to those listed in Figure 3-14. A) False-color histology image showing locations of alpha-motor neurons (dark purple) in the ventral horn and axonal projections. B) The diffusion orientation overlay (green bars). Bars represent the preferred axis of diffusion for each voxel as calculated from the DTI analysis. The shortest vector components were removed for clarity. C) The tractography overlay (green tracts) calculated using the FACT algorithm. Orientation and tractography maps show clear delineation of axon bundles. Cell positions (red dots) were used to obtain coregistration of the MRM and histology images.

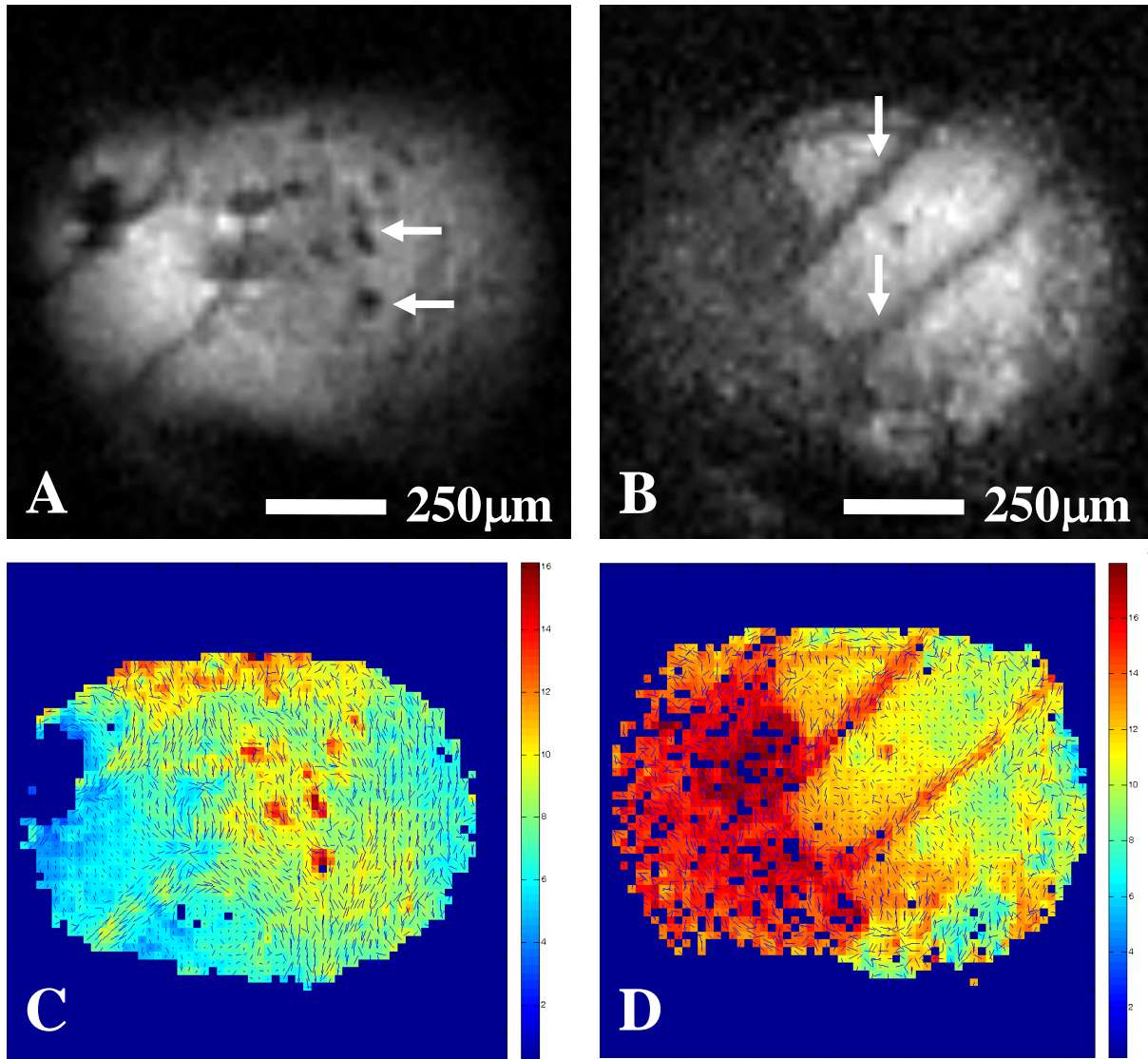


Figure 3-16. Diffusion-weighted MRM images ($TR = 2000\text{ms}$, $TE = 30.1\text{ms}$, $\Delta = 17\text{ms}$, $\delta = 6\text{ms}$, $b = 1800\text{s/mm}^2$, tissue slice = $100\mu\text{m}$, resolution = $15.625\mu\text{m}$ in-plane, Avg = 10, Scan time = 42min 40sec) of the spinal cord's ventral horn in the pig including ADC maps with diffusion orientation overlays. A) Cell bodies of alpha-motor neurons (horizontal arrows) are visible. B) Axon bundles (vertical arrows) projecting through the boundary between gray and white matter are visible. Note that the structures described possess similar signal characteristics as those seen in DW images of the rat spinal cord. C) ADC map with orientation map overlay of the MRM image in (A). Notice that locations corresponding to perikarya exhibit higher ADC values than the surrounding gray matter. D) ADC map with orientation map overlay of the MRM image in (B). Notice that bars representing diffusion orientation in the axons lie preferentially along their length. Unit for ADC value on colorbars = $10^{-1} \text{um}^2/\text{ms}$.

CHAPTER 4
MAGNETIC RESONANCE IMAGING OF MANGANESE UPTAKE AND NEURONAL
ACTIVITY IN THE LIVE HIPPOCAMPAL SLICE MODEL

Introduction

While previous experiments within this work have revealed novel insights into the origins of MRI signal in tissue elements such as axon bundles and cells, all of the studies thus far have been concerned with structural organization and morphology. As such, attaining the highest resolution possible was paramount to the success of these experiments. This necessitated the use of fixed tissue slices which can be subjected to extended imaging periods without undergoing structural changes. This is accomplished in our study by the process of formaldehyde fixation which results in cross linkage of proteins through methylene bridges (Puchtler and Meloan, 1985). While fixed tissue is tolerant to this treatment, it cannot be manipulated to undergo physiological changes. The following experiments employ acute hippocampal slices as a means of studying manganese uptake and neural function in a living tissue model.

Use of Manganese as a Contrast Agent in the Live-Slice Model of Rat Hippocampus

Despite the fact that its toxic properties have been well documented, the use of manganese ion (Mn^{2+}) has persisted due to its abilities to act as a retrograde neuronal tracer and observe calcium-dependent properties using MRI. Its ability to increase the relaxation rate of neighboring protons—thus offering SNR increases in T_1 -weighted imaging protocols—has also contributed to its continued use. Clinically, manganese has been used as a contrast-enhancing device during human liver imaging (Lim et al., 1991). When used for research purposes, manganese has traditionally been employed during *in vivo* protocols by the vascular infusion (Lin and Koretsky, 1997), intraperitoneal injection, or subcutaneous injection (Kuo et al., 2005) of fluids containing dissolved manganese salts. Due to unavoidable factors such as dilution upon entering the bloodstream, these protocols require relatively large doses of manganese and can make

accurately gauging the concentration of manganese deposited into neural tissues difficult. Direct microinjection of manganese into neural tissue has been employed as a means of circumventing the problems with systemic administration, but this technique exhibits its own difficulties: mainly, a localized concentration gradient caused by diffusion of manganese away from the site of injection (Watanabe et al., 2004). The following experiment attempts to demonstrate manganese uptake in a system which avoids the problems encountered during similar *in vivo* studies as a means of establishing an effective dosage regimen for use in the live-slice hippocampal model.

Diffusion-Weighted MRI of Neuronal Activity in the Live Hippocampal Slice Model

Functional imaging of the central nervous system is of great significance in the neurological sciences because of its potential to reveal how intricate physiological processes occurring at the cellular level contribute to the vast array of neurological functions in humans. Understanding how these mechanisms underpin higher-order brain function would offer new insight into well-studied yet poorly understood phenomena such as the activity-based changes that accompany memory formation and recall or functional deficits that manifest as disease-specific symptomatology. Perhaps most importantly, functional imaging offers a means of examining brain activity that is global in its scope as well as non-invasive: both of which are necessary to reveal the complex distribution of activity that is the hallmark of a functioning brain.

In recent years, multiple imaging modalities have been employed in an effort to provide functional data about the inner workings of the human brain. Most notably, magnetoencephalography (MEG) and blood oxygenation level dependent (BOLD) functional magnetic resonance imaging (fMRI) have made significant progress in this area, but both techniques possess unfavorable characteristics. MEG is limited to fields generated by cortical

tissue and has limited spatial resolution. While BOLD-based fMRI exhibits better spatial resolution than MEG, this technique, like all haemodynamic-based modalities, measures a surrogate signal of neuronal activity—changes in blood oxygenation level rather than actual neural activation—which has been reported to deviate both spatially and temporally from the neural activity which it purports to describe (Logothetis, 2008). Also, studies indicate that the coupling between cerebral blood-flow and metabolism—which is the physiological mechanism behind the BOLD-based fMRI signal—is not a single, non-linear relationship but may vary between brain regions or even be subject to some “central command” capable of introducing a spatial dissociation among changes in blood flow and oxygen metabolism (Vafae and Gjedde, 2004). Moreover, recent experimental evidence has described a portion of the haemodynamic response in the primary visual cortex of macaques that seems to result from anticipated trial onset rather than neural activity (Sirotin and Das, 2009). Thus, BOLD fMRI relies on a complex coupling between neural activity, cerebral metabolism and blood-flow and this, along with the shortcoming that the surrogate signal reflects neuronal mass activity, makes unambiguous data interpretation difficult in some cases. Although the limits of MEG and fMRI as means of measuring neural function are far from being realized, the respective spatial and temporal limitations inherent to these techniques will eventually interfere with their ability to accurately describe neural function. It is expected that our understanding of brain function will greatly benefit from the development and application of complementary methods for studying brain function.

Several studies have reported transient changes in neuronal morphology in tight connection with neuronal activity (Cohen et al., 1996; Iwasa et al., 1980; Kim et al., 2007). Such transient changes in tissue microstructure should—in principle—be detectable with diffusion-weighted

MRI. Using diffusion-weighted imaging in this manner would provide a non-invasive method for precise localization of neuronal activity based on a direct coupling between action potential generation and changes in tissue microstructure. Diffusion-based imaging of the working brain has been reported previously (Darquie et al., 2001, Le Bihan et al., 2006); however, it remains unclear whether signal changes observed with these methods reflect cell swelling related to neural activation (Le Bihan et al., 2006), residual vascular effects (Miller et al., 2007), or some combination of both.

The present study describes how activity-induced morphological changes occurring at the cellular level can be detected using diffusion-sensitive MRI and discusses how the described changes relate to neural function and functional imaging. The investigations are carried out in the live hippocampal brain slice model which ensures that diffusion-based functional MR measurements take place in a system devoid of vasculature's potential corrupting influence. Moreover, the absence of a functioning blood-brain barrier allows for the introduction of chemical compounds at known concentrations directly into the extracellular space (Collingridge, 1995). Our initial experiments document stability of the slice model in our experimental setup. This ensures the diffusion-weighted signal changes described are not due to factors such as temperature fluctuations, ischemia-induced cell swelling, or tissue death. The following experiments compare DW MR signal from slices in the resting state to that obtained from the same slices following exposure to potassium or kainate. These substances are used as a means to induce cellular activity in the hippocampal slice. In the case of kainate, we demonstrate signal change to be dependent on cellular response to kainate alone: no signal change is seen upon inhibition of kainate activity by pretreatment with the competitive receptor antagonist CNQX (6-cyano-7-nitroquinoxaline-2,3-dione). We also present activation patterns obtained with kainate

when slices have been pretreated with the non-competitive NMDA receptor antagonist MK-801. Different patterns of signal change are seen between the experiments employing kainate and those using potassium.

Methods

Use of Manganese as a Contrast Agent in the Live-Slice Model of Rat Hippocampus

Live hippocampal slice preparation

Male Sprague Dawley rats (150g) were anesthetized and euthanized by methods described previously (Chapter 2). The brain was excised and the hippocampi removed intact by gross dissection. Hippocampi were cut into 500 μ m thick slices along the septo-temporal axis using a McIlwain tissue chopper and immersed in oxygenated—bubbled carbogen (95% O₂, 5% CO₂)—solutions of manganese chloride tetra-hydrate (10, 20, 30, 40, 60, 80, 100, or 1000 μ M) in ddH₂O. These experiments employed a hypotonic bath solution rather than a physiologically buffered solution as a means of providing an osmotic gradient beneficial to the uptake of manganese ion. Control slices were prepared in the same manner but immersed in ddH₂O containing no manganese compound. Slices were allowed to incubate for 1h before being removed from the manganese bath, given a quick rinse in oxygenated ddH₂O, and placed in a multislice tissue chamber previously developed in our laboratory for experiments requiring the imaging of multiple slices in the course of a single MR experiment (Shepherd et al., 2002). Briefly, individual slices were placed between circular, mesh inserts hand-cut from nylon mesh (250 micron pore size) monofilament cloth (CMN-250-B, Small Parts Inc.) affixed with ethyl cyanoacrylate adhesive (42050, Ellsworth Adhesives) to handmade rings (6.0mm internal diameter, 9.0mm outer diameter, 0.6 to 0.7 mm thickness to accommodate the depth of each tissue slice) machined from solid, polyoxymethylene rods (ZRD-06-12, Small Parts Inc.) using a metal lathe.

T₁-weighted MRI experiments

Multislice, T₁-weighted (TR = 500ms, TE = 5.3ms, geometric slice thickness = 0.25mm, in-plane resolution = 150μm), spin echo images were taken and later used for statistical comparison. One dataset featuring higher resolution images (geometric slice thickness = 0.25mm, in-plane resolution = 39μm) of the manganese treatment groups were also collected. Lastly, slices from the 1000μM and 40μM treatment groups were stored in ddH₂O for periods of 24h following the initial imaging session before undergoing the same imaging protocol as a means of testing the magnitude of manganese retention in slices over this time period.

Data analysis of manganese-treated hippocampal slices

Signal to noise ratios were calculated for each slice as described previously (Chapter 2), expressed as a percentile of the untreated control, and grouped (n = 5) according to treatment condition before undergoing ANOVA statistical analysis (SigmaStat, V 3.5). In slices which exhibited a nonuniform uptake of manganese, ROIs were taken from areas in which the manganese uptake was greatest. To test whether significant differences were present between groups, a post hoc test that employed the Bonferroni correction to adjust for multiple comparisons was used.

Diffusion-Weighted MRI of Neuronal Activity in the Live Hippocampal Slice Model

Live hippocampal slice preparation

Male Sprague Dawley rats (150g) were anesthetized by inhalation of isoflurane gas. Prior to euthanasia, all animal subjects were tested for the absence of toe-pinch, righting, and ocular reflexes to insure they were unconscious and insensitive to pain. Animals were decapitated immediately following reflex testing. Following decapitation, brains were grossly dissected, immersed in ice-cold, phosphor-buffered, oxygenated artificial cerebrospinal fluid (ACSF) (120mM NaCl, 26mM NaHCO₃, 1.5mM KH₂PO₄, 1.4mM MgSO₄·7H₂O, 2mM CaCl₂·2H₂O,

3mM KCl, 10mM Glucose; osmolality = 300mOsm, pH 7.4) and cut into 500 μ m-thick sections using a vibratome as described previously (Chapter 3) with the noted exception that, during these experiments, the vibratome's tissue bath contained oxygenated ACSF solution rather than PBS. Live slices were then transferred to a 10mm NMR tube containing a multi-slice perfusion apparatus as described previously (Shepherd et al., 2002). Briefly, hippocampal slices were placed in pairs between adjacent inserts arranged in a stack (2-3 layers). Circular inserts were designed and fabricated as described previously (Chapter 4). An additional device which consisted of a hollow, 1cm high section of polyoxymethylene rod with a vertical groove cut to accommodate placement of the perfusion systems inflow line (06417-31, Cole-Parmer) was placed below the inserts to allow for induction of perfusate. Perfusion with ACSF was carried out in all experiments at a rate of 2ml/min. Two outflow lines were positioned in the NMR tube as to allow for a close proximity between tissue slices and the air interface (approx. 4-6 mm) and to ensure that—in the event of an outflow line failure—the second line could regulate perfusate volume in the NMR tube thus preventing flooding of the magnet bore.

Diffusion-weighted MRI experiments

Diffusion-weighted images (TR = 2000ms, TE = 28ms, Δ = 13.4ms, δ = 6.0ms, averages = 1, geometric slice thickness = 300 μ m, in-plane resolution = 156 μ m, b-values = 37, 600, 1200, 1800, 2400s/mm²) were acquired using a diffusion-weighted, spin echo sequence on a vertical-bore, 600MHz (14.1T) Bruker MRI system. In each experiment, images were replicated three times as well as staggered in their overall order to test for system and tissue stability respectively. A separate experiment which employed the tissue protocol of the kainate treatment group was conducted at microscopic in-plane resolutions (in-plane resolution = 78 μ m, averages = 6, b-values = 116, 1800, 2400s/mm²) in an attempt to better resolve the hippocampal slice

laminae. Once placed inside the magnet, tissue slices were perfused with untreated, oxygenated ACSF (30min) and then imaged (30min) with the perfusion paused to eliminate flow artifacts. This initial image set established a baseline for each experiment that all subsequent images in that experiment were compared to. After the first imaging session, slices were again perfused with untreated, oxygenated ACSF solution (15 min) followed by an additional perfusion (30min) of oxygenated ACSF alone—to test model stability—or ACSF containing a compound intended to evoke neural activity (27mM KCl or 100 μ M kainate). Osmolality of the ACSF solutions was maintained at physiological levels by removal of equimolar amounts of NaCl. The ACSF containing these compounds was introduced into the perfusate stream by means of an in-line, bubble-trap apparatus designed and fabricated by Dr. Brain Hansen consisting of a valve-topped, 30ml syringe attached to a polyoxymethylene base. The bubble-trap device served the dual purpose of preventing air bubbles from entering the NMR tube and ensuring minimal dilution of the treated ACSF containing KCl or kainate. Lastly, perfusion was interrupted before running the imaging protocol (30 min) a second time. In all experiments that employed chemical inhibition, the inhibitor—10 μ M MK-801 or 10 μ M CNQX—was present in the perfusate ACSF as well as the ACSF used for tissue cutting medium as previous studies have shown increased efficacy with pretreatment (Wang et al., 2006). All experiments were carried out with the spectrometer's bore temperature locked at the magnet room's ambient temperature of 23° C.

Data analysis of activity experiments

MR images collected with Paravision software (Bruker, PV3.02) were reconstructed to 32-bit floating point and processed using the analysis package ImageJ developed by the National Institutes of Health. First, datasets were coregistered spatially by aligning the images from resting state and active state using a rigid body transformation. This was done to minimize the

influence of slice movement during the experiments due to gradient motion, flow, or changes in slice morphology. The coregistration ensured appropriate pixel-wise comparisons between images and, judging by the sub-pixel magnitude of adjustment on the imaging data, indicated stability of our perfusion system. From here, images were exported to MatLab (The MathWorks Inc., v. R2007a) where a pixel by pixel analysis was carried out. Significance maps were generated using ANOVA by comparing pixels (i,j) from baseline images taken at a particular b-value with their co-registered pixels from images taken following treatment at the same b-value. Thus, each map presented is composed of color-coded pixels that convey the magnitude of statistically significant differences (1-p) within pre-treatment and post-treatment tissue slices. All statistical analysis was performed on MRI datasets that employed no filtering or apodization. Line graphs show data from ROIs taken from raw magnitude images. Differences seen in the statistical analysis were considered significant at $p < 0.05$. As a tool for quantitative analysis of the changes in diffusion properties of the tissue, we employed a biexponential fit to data from our experiments using MK-801 in combination with kainate. This fitting method also allows for comparison to similar analysis from earlier studies. The biexponential fit summarizes the normalized diffusion weighted MR signal thusly;

$$S(b) = f \cdot \exp(-b \cdot D_1) + (1-f) \cdot \exp(-b \cdot D_2) \quad (4-1)$$

Where the signal as a function of diffusion weighting, b , is then described as the sum of two components attenuated by diffusion coefficients D_1 and D_2 , and weighted by f and $(1-f)$, respectively. In our analysis we fit (4-1) to data from the resting state. The active state is then fitted using the values for D_1 and D_2 obtained from the fit to the resting state data allowing only the weighting of the two signal components to shift from resting state to active state. We denote

the faster diffusion coefficient D_1 and the slower D_2 arbitrarily; therefore, the factor f describes the weighting of the fast-decaying signal component.

Results

Use of Manganese as a Contrast Agent in the Live-Slice Model of Rat Hippocampus

Initial experiments conducted with concentrations of manganese—1000 μ M—found to be effective for use in *in vivo* studies (Silva et al., 2004) proved to be far too concentrated for use in the live-slice protocol and resulted in drastically reduced SNR within hippocampal slices due to the T_2^* -shortening effects of manganese (Figure 4-1). Analysis of variance and post hoc statistical testing revealed that all groups save for that exposed to the lowest concentration of manganese (10 μ M) achieved statistically significant ($\alpha = 0.05$) signal increases as compared to controls (Figure 4-2). Moreover, the multiple between-group comparisons revealed that 40 μ M, 60 μ M, and 80 μ M treatment groups achieved statistically significant signal increases as compared to the 10 μ M treatment group. The greatest gains in SNR were achieved in the 40 μ M and 60 μ M treatment groups which both exhibited a nearly five-fold—4.79X and 4.82X respectively—increase over the control group. The fact that the 100 μ M treatment group did not achieve a statistically significant signal difference when compared to the 10 μ M treatment group suggests that the point at which T_2^* shortening effects begin to outweigh signal increases gained by T_1 shortening effects occurs in close proximity to this manganese concentration. The signal enhancing and ablating effects due to manganese exposure at concentrations of 40 μ M and 1000 μ M respectively were found to be retained in tissues for up to 24h following the initial exposure to manganese (Figure 4-3). Finally, the higher resolution scan (39 μ m in-plane) of a hippocampus exposed to 100 μ m manganese resulted in contrast enhancement which revealed the presence of hippocampal tissue laminae not commonly visible in equivalent MR images

employing untreated tissue (Figure 4-4). These laminae included the stratum lucidum and stratum lacunosum. The observation that manganese uptake permitted the visualization of these tissue layers coupled with the fact that said layers were not visible in the lower dosage treatment groups which produced higher signal suggests a reduced uptake of manganese ion as compared to adjacent tissue layers.

Diffusion-Weighted MRI of Neuronal Activity in the Live Hippocampal Slice Model

Slice stability experiments

Our control experiment intended to test for hippocampal slice stability within the confines of our research protocol. Results revealed that all slices ($n = 4$) were found to be stable with equivalent signal magnitude and diffusion attenuation over both imaging periods where the slices had been exposed to untreated, oxygenated ACSF during perfusion. Difference maps highlighting pixels which differ significantly ($p < 0.05$) between diffusion-weighted images from the first and second imaging sessions were calculated for all four slices and overlaid onto corresponding MR images (Figure 4-5). Few pixels achieved a level of diffusion signal change which resulted in statistically significant differences in either the perfusate or the hippocampal slices. Attenuation curves from a plot of raw signal intensity as a function of b-value revealed that no significant difference existed between imaging periods for perfusate or tissue at any of the b-values tested (Figure 4-6). Many pixels which achieved statistically significant differences between imaging periods in our stability experiments were located at the physical boundary between tissue and perfusate which is suggestive of an artificial edge effect.

Potassium-induced neural activation and inhibition via MK-801

Following exposure to ACSF containing 27mM KCl, hippocampal slices ($n = 4$) exhibited significant increases in diffusion-attenuated signal (Figure 4-7). Although KCl-treated slices exhibited localized diffusion-signal changes in the CA1 and CA3 regions of the hippocampus,

they also showed a pattern of diffusion signal change along the border between tissue and perfusate that encircled their perimeters nearly uninterrupted. This was true of all samples within the KCl treatment group and could be indicative of generalized swelling within the slices. Our attempts to inhibit the depolarization-inducing effects of elevated extracellular potassium concentration with the non-competitive NMDA receptor antagonist MK-801 did not produce a decrease in diffusion-attenuated signal intensity (Figure 4-8). Contrary to our original expectations, slices treated with MK-801 prior to potassium exposure exhibited a larger diffusion-signal increase—in terms of both magnitude and affected area—than hippocampal slices treated with potassium alone. This finding not only illustrates that MK-801 treatment is not sufficient to inhibit the effects of elevated extracellular potassium, but also suggests that there are alternate mechanisms at work—i.e. besides activation-induced sodium and calcium influx through NMDA channels—contributing to the observed diffusion signal increases induced by exposure to elevated potassium. When hippocampal slices from groups exposed to untreated ACSF were compared to those treated with MK-801, untreated slices exhibited significantly ($p < 0.0001$) higher SNR (Figure 4-9).

Magnetic Resonance Microscopy of kainate-induced neural activation

High-resolution scans depicting hippocampal slice activation with kainate exhibited a global decrease in ADC as illustrated by our map depicting percent change of ADC between resting and active states (Figure 4-10). While some areas registered an ADC increase, the majority of pixels registered a decrease which is in accordance with the increase in diffusion signal observed in acquisitions taken at lower resolutions. Unfortunately, the low signal levels associated with these high-resolution scans were counterproductive to the intended purpose of achieving clearer separation of the hippocampal tissue layers as it was all but impossible to differentiate between tissue subtypes in the slices. For this reason, the scan protocol for higher

resolution MRM scans was abandoned in favor of one capable of providing lower resolution scans in which the separate hippocampal tissue layers could be distinguished clearly.

Kainate-induced neural activation and inhibition via CNQX

Following exposure to ACSF containing 100 μ M kainate, hippocampal slices (n = 6) exhibited significant ($p < 0.05$) increases in diffusion-attenuated signal (Figure 4-11). Although all slices in this group exhibited some degree of significant diffusion signal increase, the variability of both location and magnitude of the described signal change is evident upon viewing the difference maps. Diffusion-signal decay curves representing raw signal from ROIs drawn in tissue and perfusate from resting and kainate-induced active states are shown (Figure 4-12, A). Normalized decay curves from tissue ROIs were also calculated (Figure 4-12, B). Tissue ROIs contained portions of the pyramidal cell layer, stratum radiatum, and stratum oriens from the CA1 region of the hippocampus. The tissue signal curves separate as diffusion weighting increases. Raw diffusion signal increase as a result of kainate activation reaches approximately 18% at the highest b-value tested ($b = 2400 \text{ s/mm}^2$) for the described ROI. For the control experiment in which hippocampal slices (n = 6) were treated with the competitive, kainite receptor antagonist CNQX (10 μ M) prior to kainite (100 μ M) exposure, far fewer pixels registered statistically significant diffusion signal increases suggesting a lack of activity in the chemically inhibited samples (Figure 4-13). The majority of pixels achieving significant differences in diffusion signal are located at the border between tissue and perfusate as was the case in our stability experiment.

Kainate-induced neural activation with MK-801 pretreatment

For the experiment in which slices (n = 6) were pretreated with MK-801 (10 μ M) prior to activation with kainate, an even more robust diffusion-signal increase was observed (Figure 4-

14). The magnitude and localization of areas displaying significant increases were far less variable than the experiment which employed activation by kainate alone. The greatest signal changes were localized to tissues of the CA1 region—primarily the pyramidal cell layer and stratum radiatum—as well as the granule cell and molecular layers of the dentate gyrus. Diffusion-signal decay curves generated from small ROIs encompassing portions of the CA1 region (Figure 4-15) as well as large ROIs encompassing areas exhibiting the highest magnitude of signal change measured at $b = 2400\text{s/mm}^2$ (Figure 4-16) were compiled. In both cases, diffusion characteristics were found to have changed in the tissue following activation by kainate as evidenced by the divergence that occurred in signal attenuation curves as diffusion weighting increased. Normalized signals from Figure 4-16 were used in a biexponential analysis of the change in diffusion properties between resting and active states. A summary of this analysis is presented (Table 4-1).

Discussion

Use of Manganese as a Contrast Agent in the Live-Slice Model of Rat Hippocampus

While the use of manganese as a clinically viable contrast agent depends heavily on the development of new chemical compounds and protocols which limit its toxic effects, the myriad of calcium-dependent physiological processes which can be observed indirectly using manganese as a MR contrast agent virtually assures its continued use in medical research. Its ability to enter cell bodies through channels normally designated for calcium differentiates manganese from contrast agents such as gadodiamide which have been reported to remain primarily in the extracellular space (Normann and Hals, 1995). This characteristic may foster retention in tissues—as evidenced by our data exhibiting signal consistency in treated slices over a 24h period—during cases in which prolonged signal enhancement is required. Currently, the increase in signal intensity garnered by using manganese in our slice protocol could be traded for

improved spatial resolution or decreased scan time. The improved contrast can be used to visualize hippocampal layers not seen in conventional MRI. In future studies, we hope to employ manganese as a means of observing apoptosis—a calcium-dependent physiological process—using MRI techniques.

Diffusion-Weighted MRI of Neuronal Activity in the Live Hippocampal Slice Model

Neural activity is associated with an increase in extracellular potassium due to the efflux of potassium ions from cells as a part of the repolarization phase of nerve firing. If activity in the neuron outpaces the ability of the Na/K ATP pumps to fully restore this concentration gradient, the shift in extracellular potassium concentration will increase the neuron's resting membrane potential leading to a hyper excitable cell (Alberts et al., 2002). Artificially increasing the extracellular potassium ion concentration depolarizes the cells and elicits a rapid-fire behavior from affected neurons. These patterns of chemically elicited neural firing have been associated with excitotoxic activity and are used classically to model epileptogenesis (Zuckermann et al., 1968).

Kainate is a chemical compound that has also been employed in epileptogenic models due to its role in excitatory neuronal signaling (Schwob et al., 1980; Shinozaki and Konishi, 1970). It acts directly on the ionotropic, non-NMDA glutamate receptor that is a namesake for the compound itself. These kainate receptors are present on both pre and postsynaptic membranes and are thought to play a key role in regulating neural excitability (Contractor et al., 2000).

It is for their role in the events associated with neural activation that kainate and potassium compounds were chosen for our study. While the outcome of exposure to these compounds in the slice model is quite similar in that they both are able to elicit activation-based—and in the case of potassium, non-activation based—cell swelling, the mechanisms with which they act are remarkably different allowing us to observe and manipulate different aspects of the biological

machinery responsible for neural activation. We have attempted to relate neural activation induced by these compounds to changes in the diffusion signal of MR images. While it is not yet agreed upon to what extent vascular flow contributes to the diffusion signal increases seen as a result of neural activation *in vivo*, the experiments presented here show that changes in the diffusion-weighted signal can be observed in devascularized tissue treated with compounds that elicit neural activity. This result suggests that the activation-based changes in the *in vivo* experiments described by Darquie and Le Bihan (Darquie et al., 2001; Le Bihan et al., 2006) should not be summarily dismissed as a vascular flow phenomenon pending closer investigation into the origins of the described signal change.

The signal attenuation curves of treated and untreated tissue separate as the diffusion weighting increases indicative of the length scale of the microstructural changes caused by neuronal activation. Experiments using kainate show that the active state is more signal intense than the resting state and that the diffusion attenuation in the active state is slower than in the resting state. While the experiment employing kainate alone exhibited noticeable between-slice variability in the elicited diffusion changes, this effect could be accounted for by variation in kainate receptor expression along the septo-temporal axis as our study did not control stringently for this variable (Martens et al., 1998). Conversely, this signal change does not occur if the tissue is pretreated with the inhibitor CNQX. The described signal change must therefore arise from the microstructural changes accompanying neuronal activation and thus represents a potential means of observing cellular function with diffusion-weighted MRI. Activation-induced cell swelling is most evident in the experiment where slices were pretreated with the neuroprotective NMDA receptor antagonist MK-801. This effect can be attributed to a reduction in the initial ischemic insult that results from slice procurement which lowers the diffusion-weighted signal in control

scans thereby increasing the magnitude of signal change following activation. The described change in diffusion attenuation follows similar trends regardless of whether MK-801 is employed: activated slices exhibit slower diffusion attenuation indicating a decreased apparent diffusion coefficient (ADC) in the active state. Such activity-dependent decreases in ADC were reported previously in *in vivo* studies (Darquie et al., 2001; Le Bihan et al., 2006). The biexponential analysis performed on ROIs from slices pretreated with MK-801 and exposed to kainate allows for comparison to a similar analysis performed on *in vivo* diffusion weighted fMRI data (Le Bihan et al., 2006) where a shift of 1.7% was found from fast to slow decaying signal between the resting and active states. Our analysis shows the same overall behavior but the effect is more pronounced in the slice model with the fast decaying signal component reduced by 49.6% on average between the resting and active state. The larger magnitude of signal change in our studies is likely due to the additive effect of multiple neuronal depolarizations which occur over longer scan times compared to those used in the *in vivo* studies.

Although treatments with both elevated KCl and kainate lead to a widespread diffusivity decrease in the hippocampus, our results—in the case of KCl where the effect was seen to be more general across the slice—suggest that the drop in diffusion rate can occur in the absence as well as the presence of neural firing. The same effect has been reported in previous studies (Andrew et al., 1996) and attributed to glial swelling throughout the slice as K^+ is taken up by the glial network. Another possible contribution to the observed results is that the neuronal firing due to elevated extracellular potassium ion was not adequately inhibited upon introduction of the NMDA antagonist MK-801. This seems likely given the observation that the diffusion signal change increased in area and intensity when using MK-801 in conjunction with elevated potassium. The described effect could be explained by MK-801's ability to suppress NMDA-

receptor mediated cellular swelling following ischemic stroke (Gill et al., 1996) coupled with activity induced by voltage-gated sodium channels acting independently of NMDA channels rather than in concert with them (Takahashi et al., 1997). These findings highlight the need to exercise caution in establishing a correlative or causative relationship between activity-inducing treatments and neural activity before this effect could hope to be utilized as a means of obtaining functionally relevant MRI data in the clinic. Also, while the methods of neural activation described in the current study are well established, the levels of activity elicited from our treatment protocols have long been associated with excitotoxicity. It is worth noting however that other studies, in the case of KCl-induced activation, have found this swelling to be reversible even when using equivalent concentrations of potassium (Stroman et al., 2008).

In the present study, we have described the ability to monitor periods of increased neural activation using diffusion MRI methods with the shift in diffusion signal attributed to micro-structural changes occurring at the cellular level. With sufficient development, this effect could be employed in functional neuroimaging experiments that obtain better spatial and temporal resolution than offered by current MEG and BOLD-based protocols.

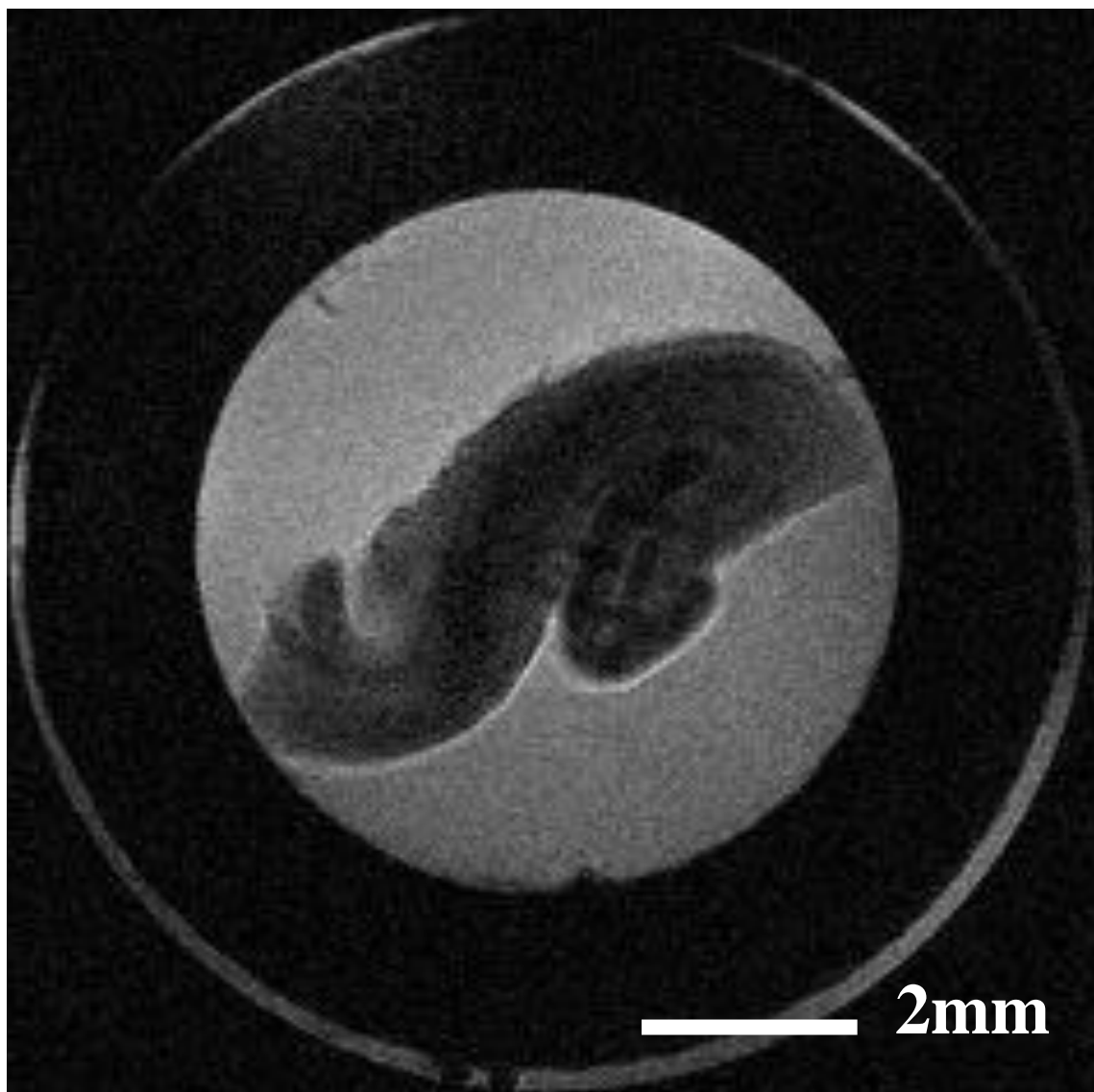


Figure 4-1. T_1 -weighted (TR = 500ms, TE = 5.3ms, geometric slice thickness = 0.25mm, in-plane resolution = 39 μ m) image of a hippocampal slice from the 1000 μ M manganese treatment group. The drastic T_2^* shortening effects following high-concentration manganese exposure are evident due to the near-complete ablation of signal from within the hippocampal tissue.

Signal to Noise Measurements of Hippocampal Slices Based on Manganese Treatment Group

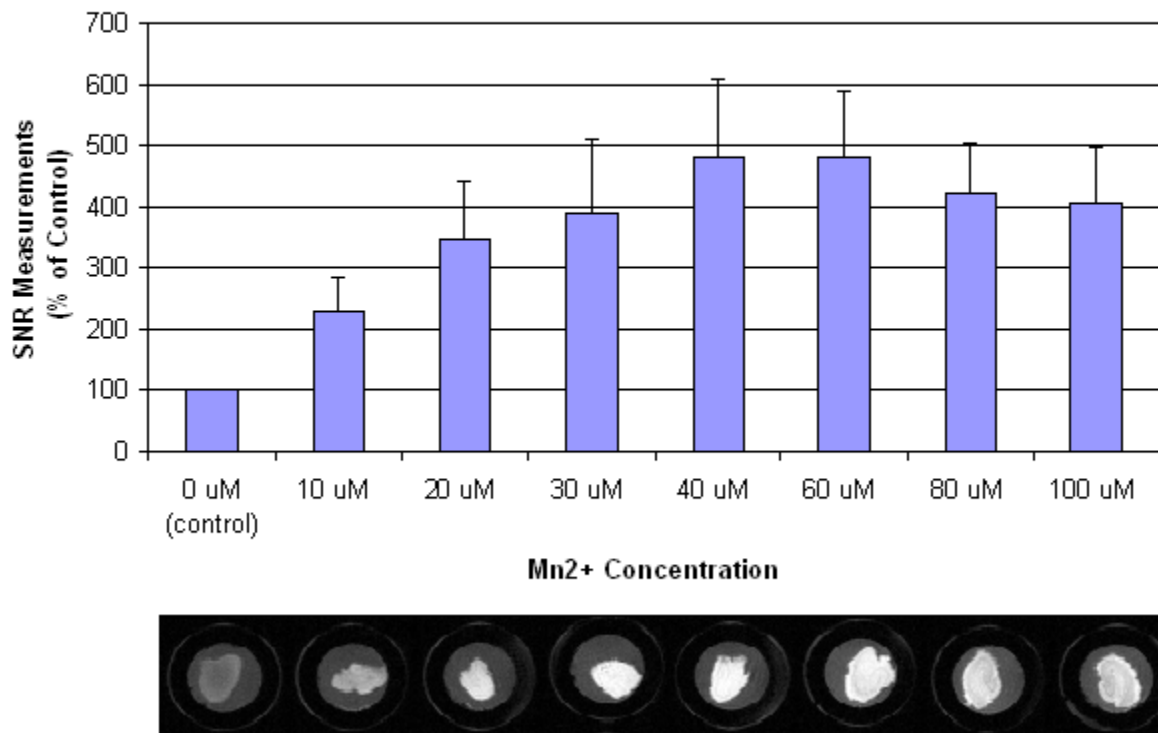


Figure 4-2. Mean signal to noise ratios for all manganese treatment groups ($n = 5$) reported as percent of control. All treatment groups with the exception of the 10 μ M group achieved statistically significant signal increases ($\alpha = 0.05$) compared to control. The 40 μ M, 60 μ M, and 80 μ M treatment groups were also found to have attained significant signal increases over the 10 μ M group. Inset MRIs are representative examples from each of the eight treatment groups in order of increasing manganese concentration.

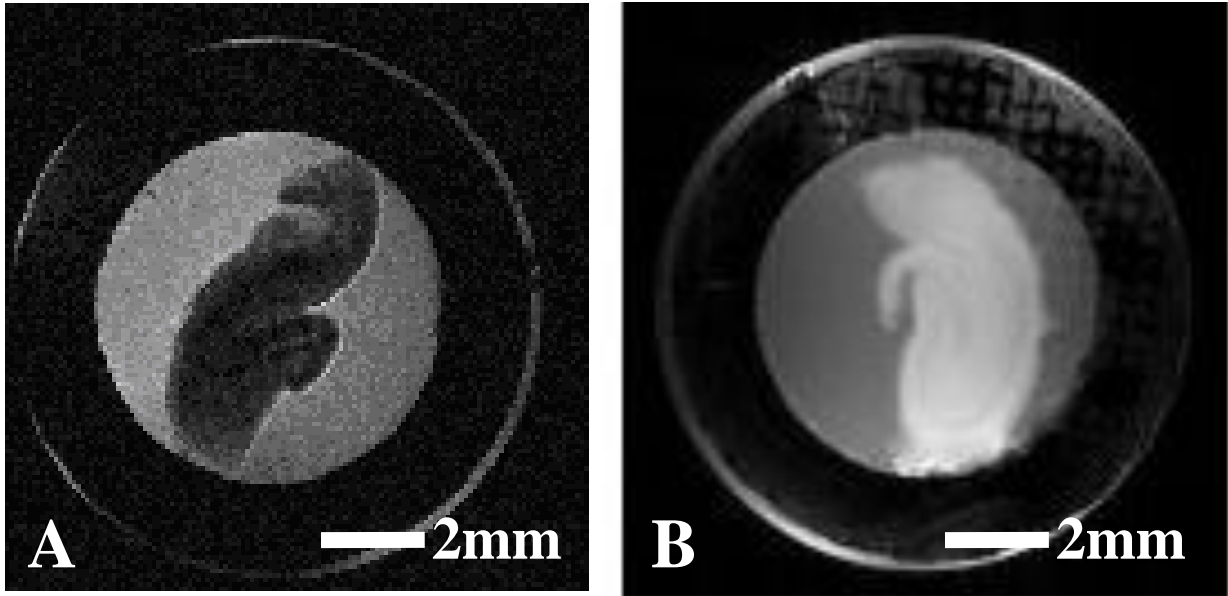


Figure 4-3. T_1 -weighted (TR = 500ms, TE = 5.3ms, geometric slice thickness = 0.25mm, in-plane resolution = $150\mu\text{m}$) images from the live hippocampal slice protocol following a 1h bath application of manganese and a 24h wash in hypotonic ddH₂O containing no manganese. A) A representative MRI of a slice from the $1000\mu\text{M}$ treatment group 24h following manganese exposure B) A representative MRI of a slice from the $40\mu\text{M}$ treatment group 24h following manganese exposure. Both treatment groups pictured clearly retained the relaxation altering effects of their exposure to manganese 24h after the initial exposure period implying that the manganese ions themselves were also retained.

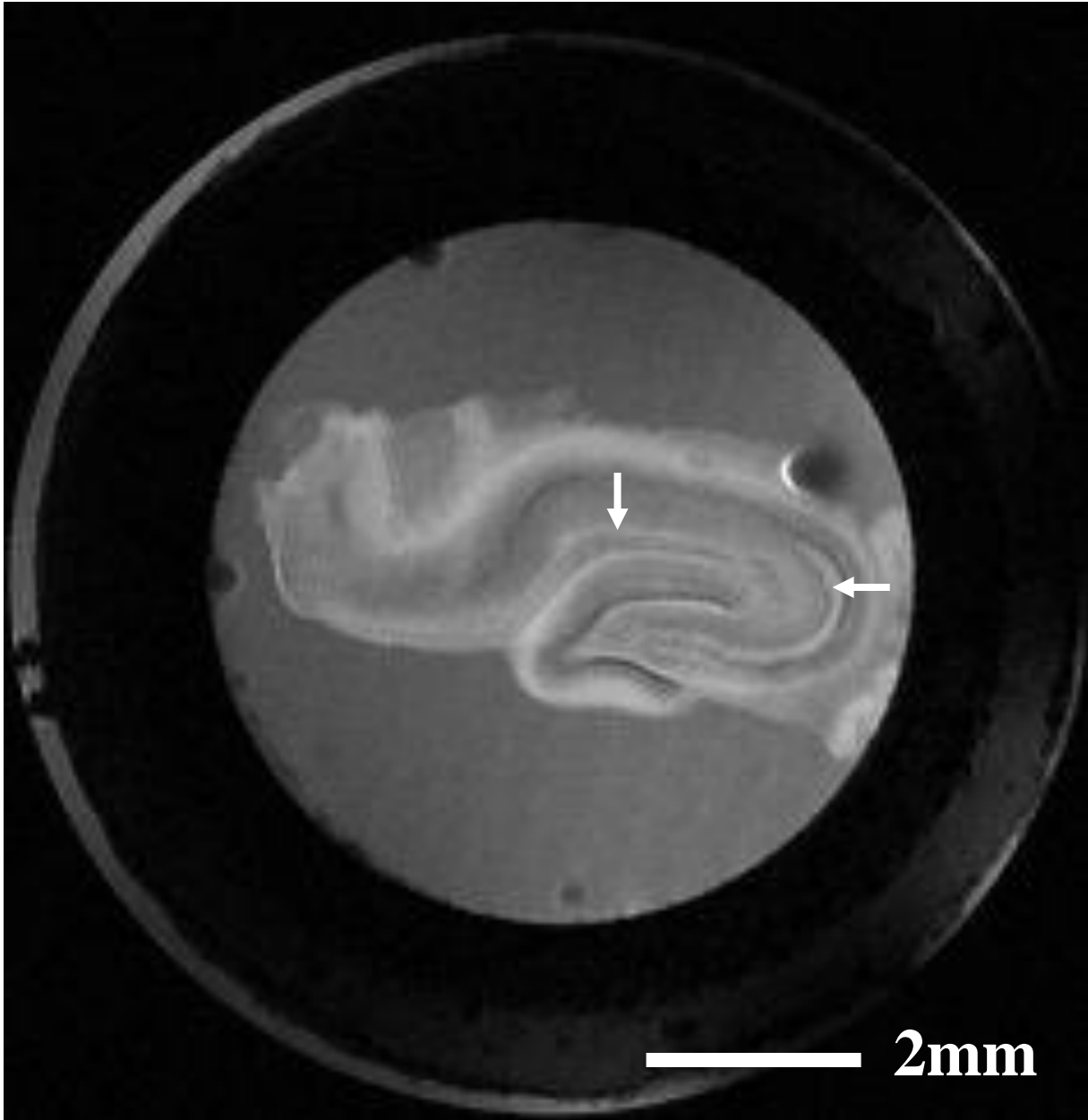


Figure 4-4. T_1 -weighted image (TR = 500ms, TE = 5.3ms, geometric slice thickness = 0.25mm, in-plane resolution = $39\mu\text{m}$) of a representative hippocampal slice from the $100\mu\text{M}$ manganese treatment group. The laminar anatomy of the hippocampus is displayed in non-native contrast as a result of the manganese treatment. Specific laminae including the stratum lucidum (horizontal arrow) and the stratum lacunosum (vertical arrow) which are generally not visualized in conventional MR imaging are revealed thanks to T_2^* shortening effects in adjacent tissue layers.

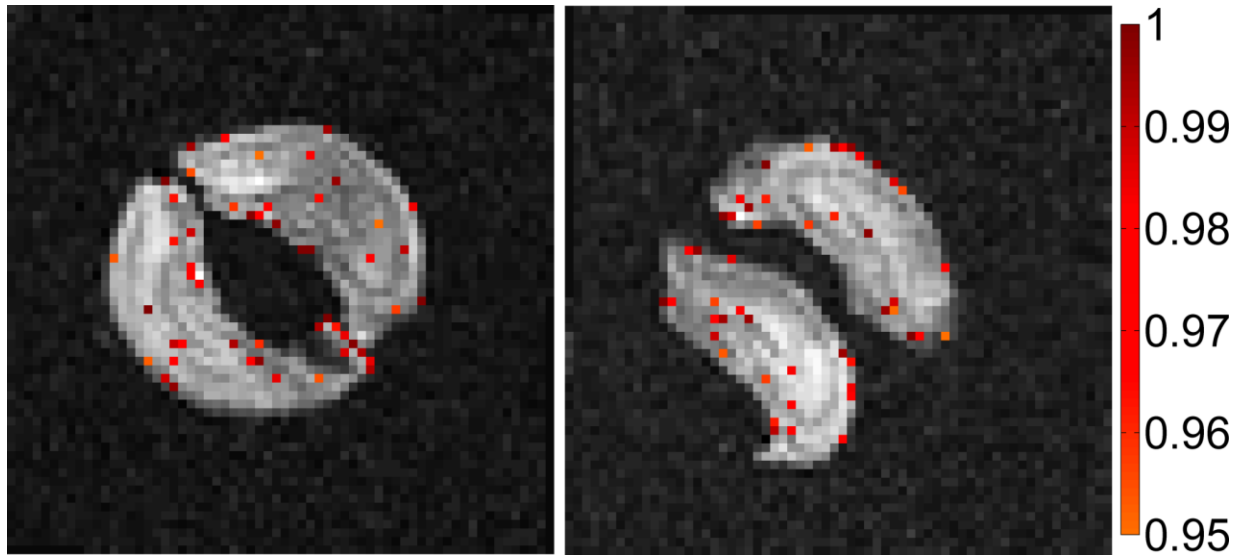


Figure 4-5. Difference maps from rat hippocampal slices employed during our stability experiments overlaid on corresponding diffusion-weighted ($b = 2400\text{s/mm}^2$) MR images. Pixels which achieved significant ($p < 0.05$) differences between the first and second imaging sessions are highlighted and have been color-coded based on degree of significance. Colorbar shows $(1-p)$.

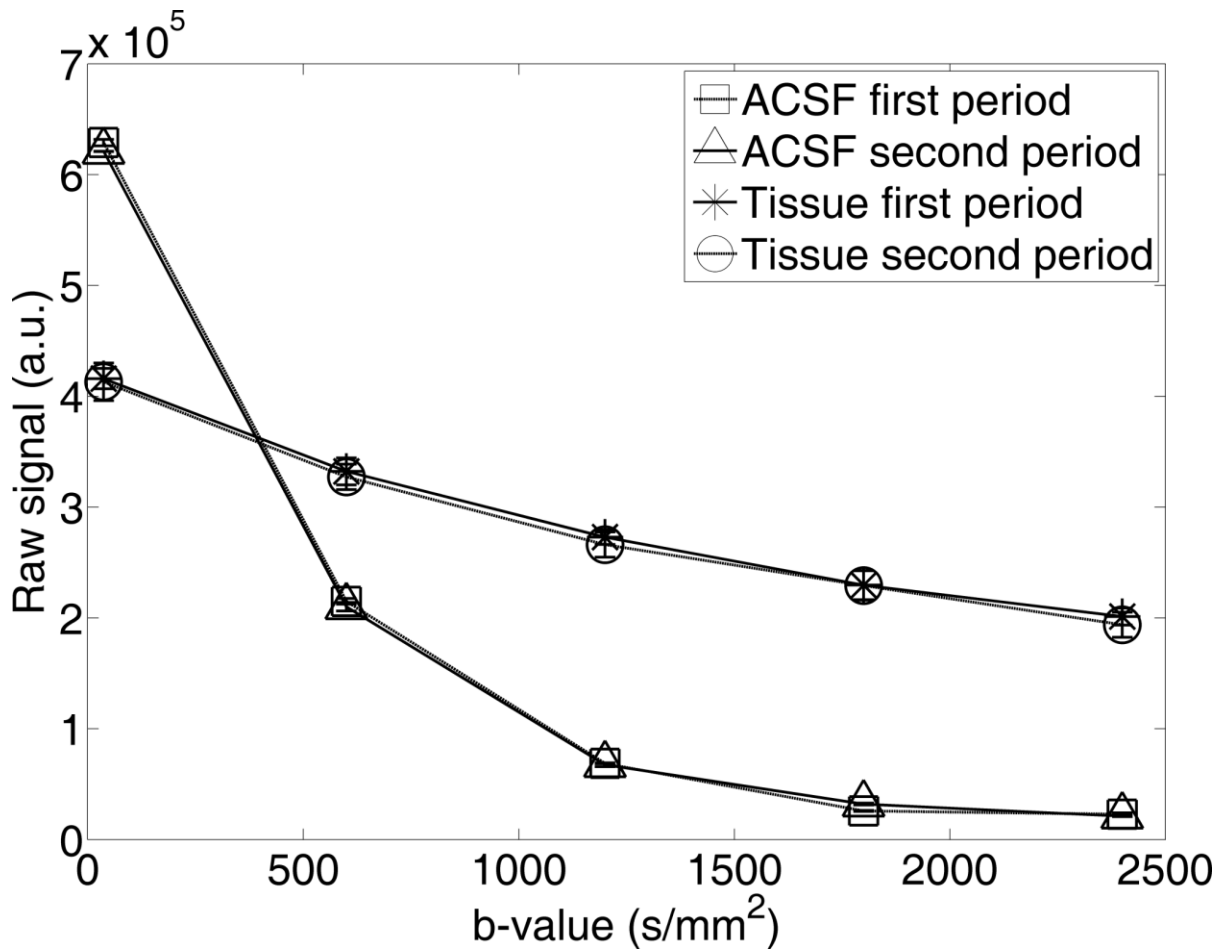


Figure 4-6. Plot of raw signal (arbitrary units) versus diffusion weighting (b-value) for ROIs drawn in oxygenated ACSF perfusate and live-slice hippocampal tissue. Diffusion attenuation curves from the initial imaging session (square, asterisk) and the second imaging session (triangle, circle) are displayed. No statistically significant ($p \leq 0.05$) differences were observed in perfusate or tissue slices during the timecourse of our experimental protocol illustrated by the overlap of our perfusate curves (square, triangle) and the overlap of our tissue curves (asterisk, circle).

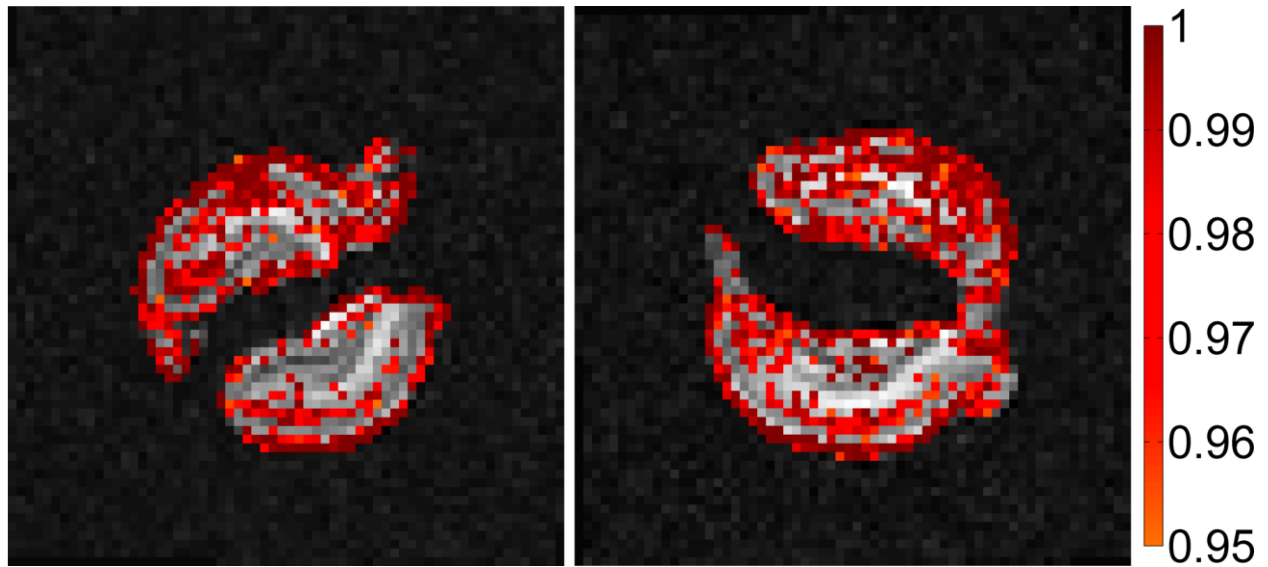


Figure 4-7. Difference maps overlaid on corresponding diffusion-weighted ($b = 2400\text{s/mm}^2$) MR images illustrating diffusion signal changes in rat hippocampal slices following exposure to elevated potassium ion concentration. These maps show significantly different ($p < 0.05$) pixels in the slices ($n = 4$) following exposure to ACSF containing elevated KCl (27mM). Colorbar shows $(1-p)$.

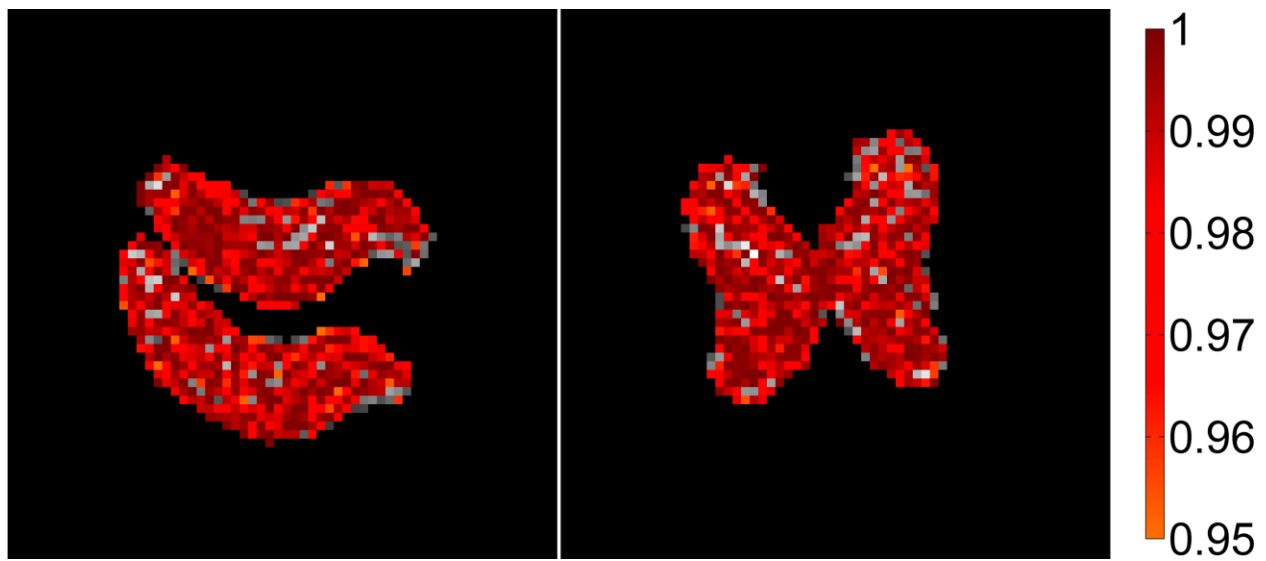


Figure 4-8. Difference maps overlaid on corresponding diffusion-weighted ($b = 2400\text{s/mm}^2$) MR images illustrating diffusion signal changes in rat hippocampal slices upon exposure to elevated potassium ion concentration following pretreatment with MK-801. These maps show significantly different ($p < 0.05$) pixels in the MK-801 ($10\mu\text{M}$) pretreated slices ($n = 4$) following exposure to ACSF containing elevated KCl (27mM). Colorbar shows $(1-p)$.

Mean Signal to Noise Ratios of Untreated and MK-801 Treated Hippocampal Slices

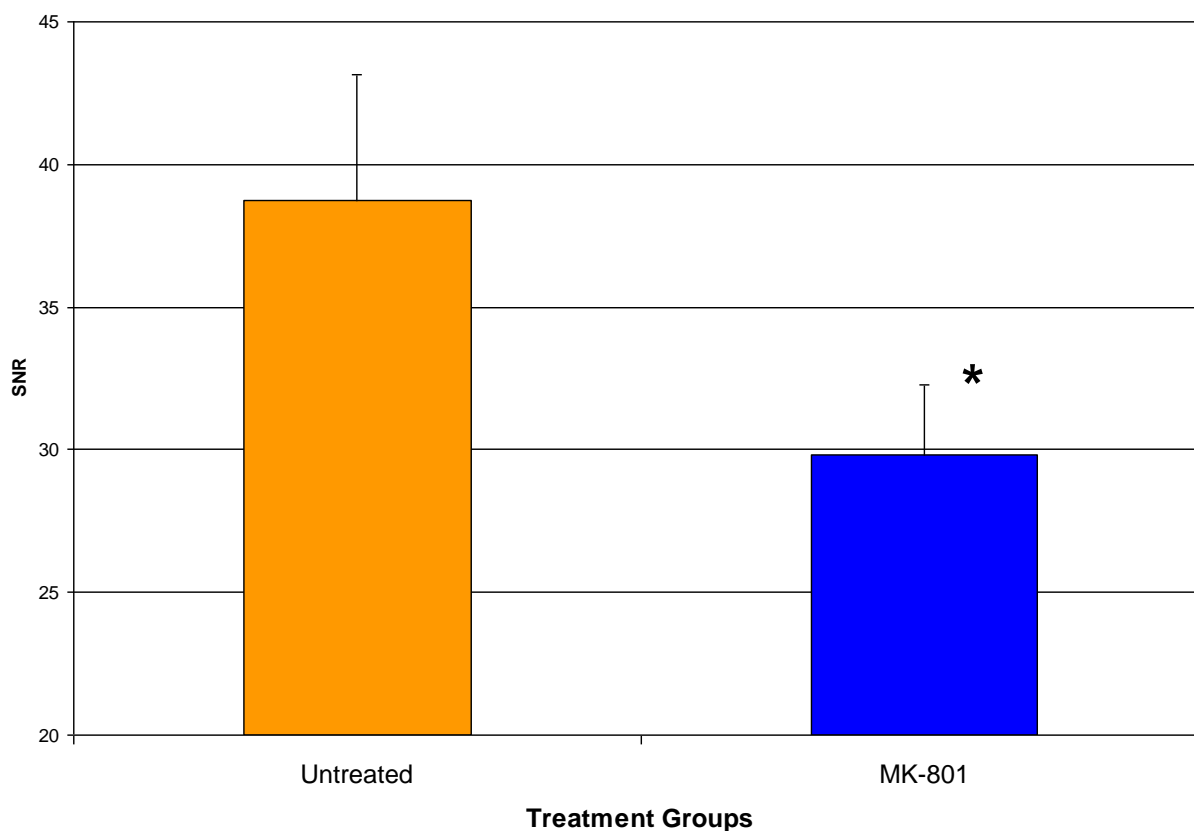


Figure 4-9. Bar graph representing the mean difference in signal to noise ratios between untreated rat hippocampal slices (n = 8) and those treated with the non-competitive NMDA receptor antagonist MK-801 (n = 10). Mean SNR was significantly lower (*; $p < 0.0001$) in MK-801 treated slices as compared to untreated slices. This effect is most likely attributable to the suppression of NMDA-induced tissue edema following mechanical injury.

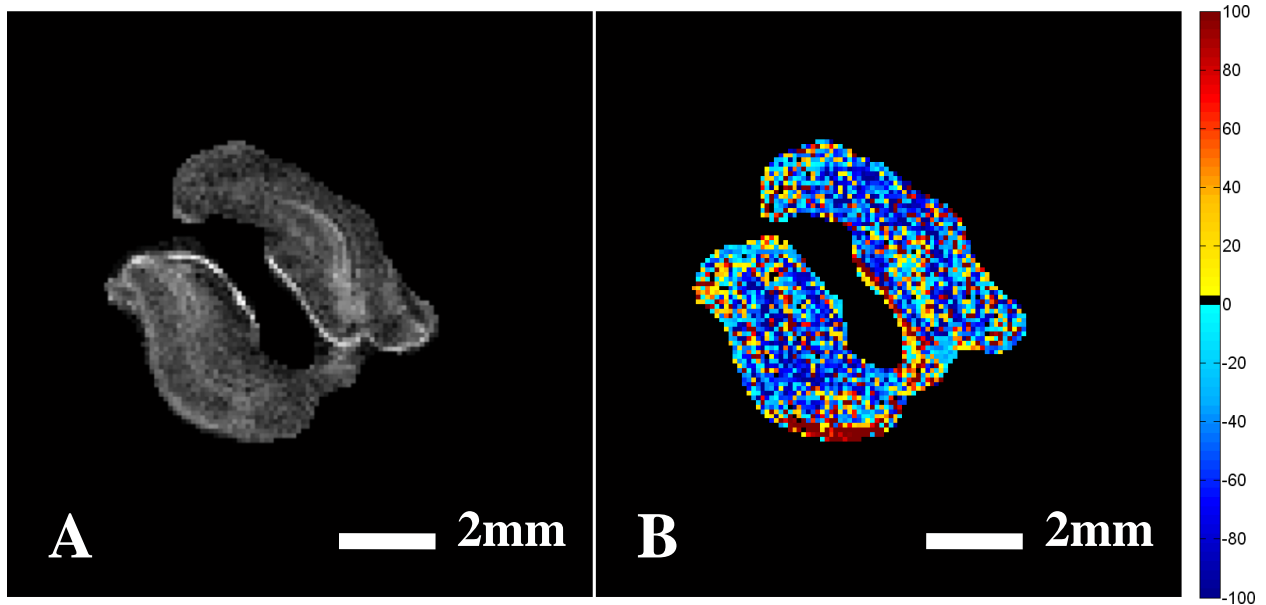


Figure 4-10. Magnetic resonance microscopy of rat hippocampal slices treated with kainate to induce neural activity. A) A representative image from the MRM datasets ($b = 2400\text{s/mm}^2$, in-plane resolution = $78\mu\text{m}$, averages = 6) collected during our activity experiment. B) Difference map illustrating the percent change in mean diffusivity for a pair of live hippocampal slices before and after treatment with ACSF containing kainate ($100\mu\text{M}$). Although the trend towards decreasing mean diffusivity dominates the majority of the slice, increases in mean diffusivity are also present. Due to the low signal available in our MRM images, assignment of regional diffusivity changes within hippocampal slices was problematic. Colorbar shows percent change in mean diffusivity above (hot colors) and below (cold colors) those measured during the tissue's resting state.

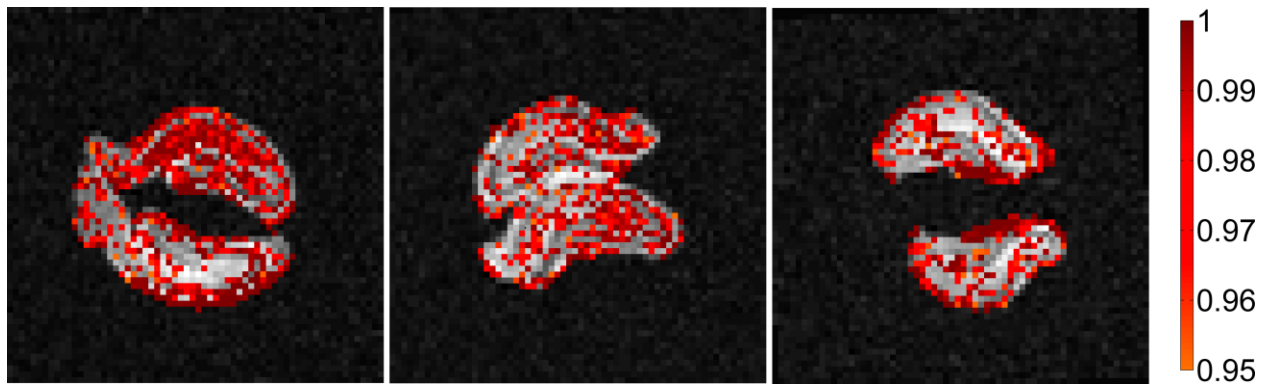


Figure 4-11. Difference maps overlaid on corresponding diffusion-weighted ($b = 2400\text{s/mm}^2$) MR images illustrating diffusion signal changes in rat hippocampal slices following exposure to kainate. These maps show significantly different ($p < 0.05$) pixels in the slices ($n = 6$) following exposure to ACSF containing kainate ($100\mu\text{M}$). Colorbar shows $(1-p)$.

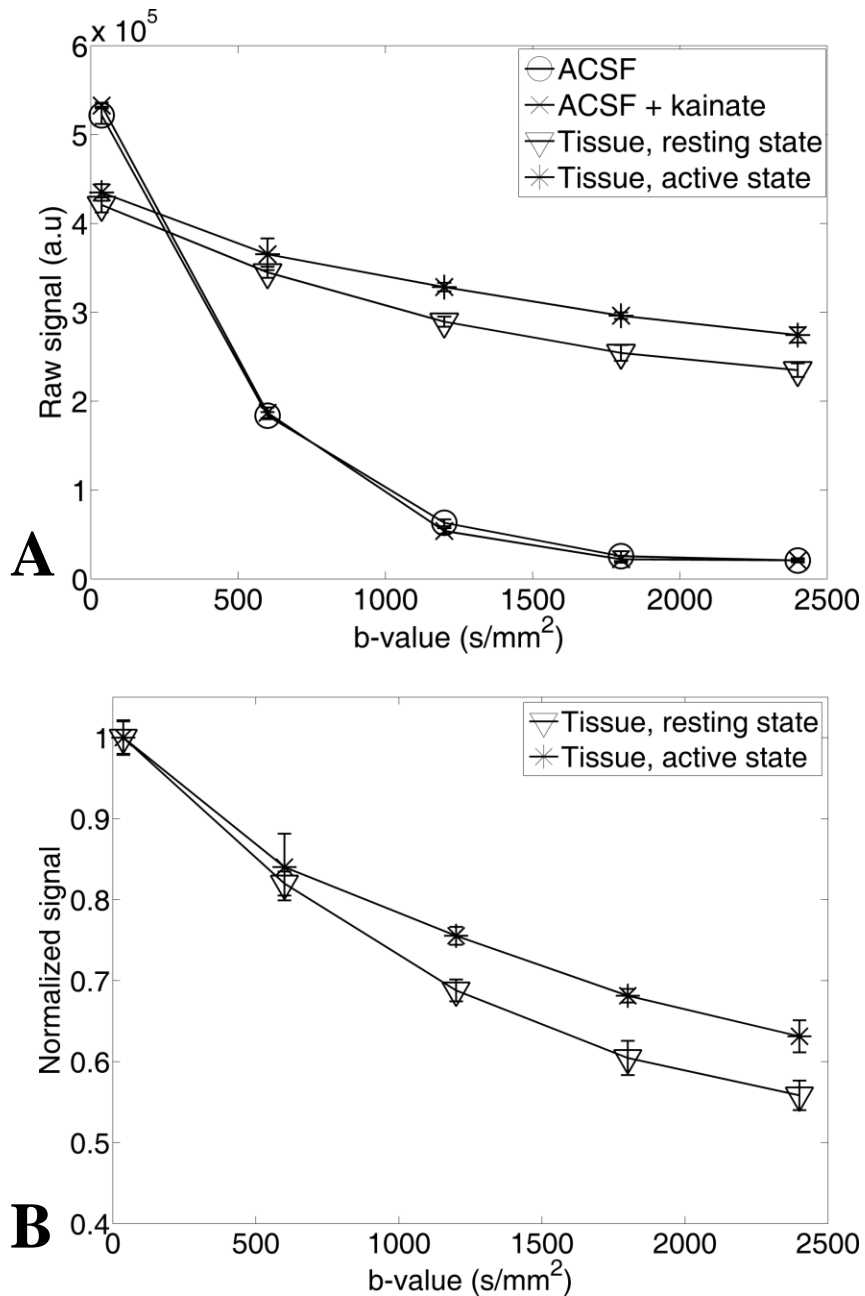


Figure 4-12. Diffusion signal decay curves from live hippocampal slice ($n = 6$) experiment showing signal changes as a function of diffusion weighting before and after activation with kainate. A) Raw diffusion signal attenuation curves for ROIs drawn in the ACSF perfusate (circle, cross) and the CA1 region of the hippocampus (triangle, asterisk) before (circle, triangle) and after (cross, asterisk) activation with $100\mu\text{M}$ kainate. B) Normalized data from the tissue ROI described in (A) illustrating that the curves diverge as diffusion weighting increases.

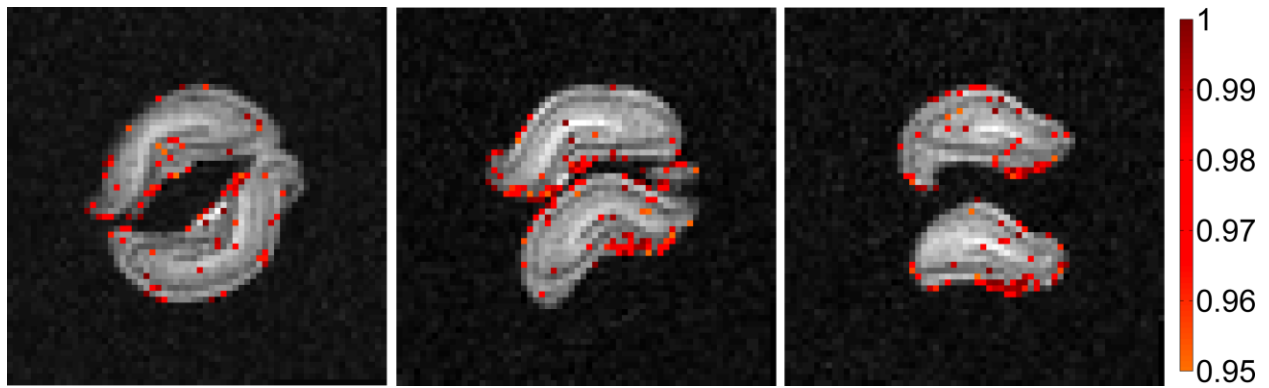


Figure 4-13. Difference maps overlaid on corresponding diffusion-weighted ($b = 2400\text{s/mm}^2$) MR images illustrating the relative lack of diffusion signal changes in rat hippocampal slices pre-treated with CNQX (6-cyano-7-nitroquinoxaline-2,3-dione) after kainate exposure. These maps show significantly different ($p < 0.05$) pixels in the slices ($n = 6$) pretreated with CNQX ($10\mu\text{M}$) following exposure to ACSF containing kainate ($100\mu\text{M}$). Colorbar shows $(1-p)$.

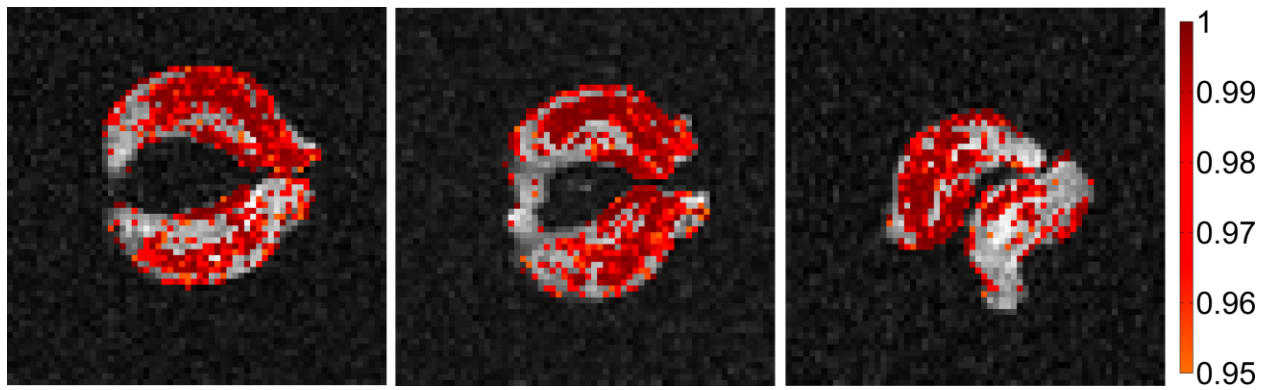


Figure 4-14. Difference maps overlaid on corresponding diffusion-weighted ($b = 2400\text{s/mm}^2$) MR images illustrating the robust diffusion-signal increases after kainate exposure. These maps show significantly different ($p < 0.05$) pixels in the slices ($n = 6$) pretreated with CNQX ($10\mu\text{M}$) following exposure to ACSF containing kainate ($100\mu\text{M}$). Colorbar shows $(1-p)$.

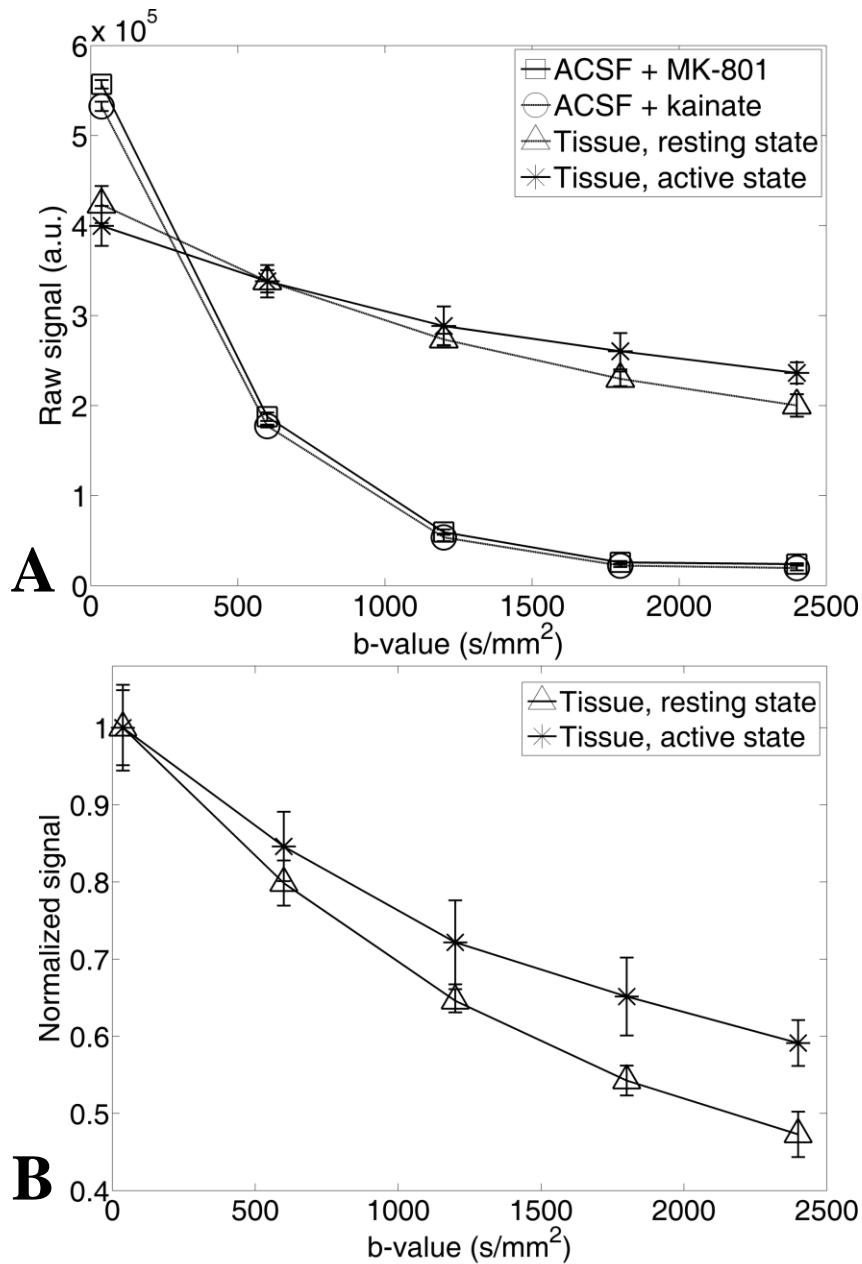


Figure 4-15. Diffusion signal decay curves from live hippocampal slice ($n = 6$) experiment in which tissue was pretreated with MK-801 ($10\mu\text{M}$) showing signal changes as a function of diffusion weighting before and after activation with kainate. A) Raw diffusion signal attenuation curves for ROIs drawn in the ACSF perfusate (square, circle) and the CA1 region of the hippocampus (triangle, asterisk) before (square, triangle) and after (circle, asterisk) activation with $100\mu\text{M}$ kainate. B) Normalized data from the tissue ROI described in (A) illustrating that the curves diverge as diffusion weighting increases.

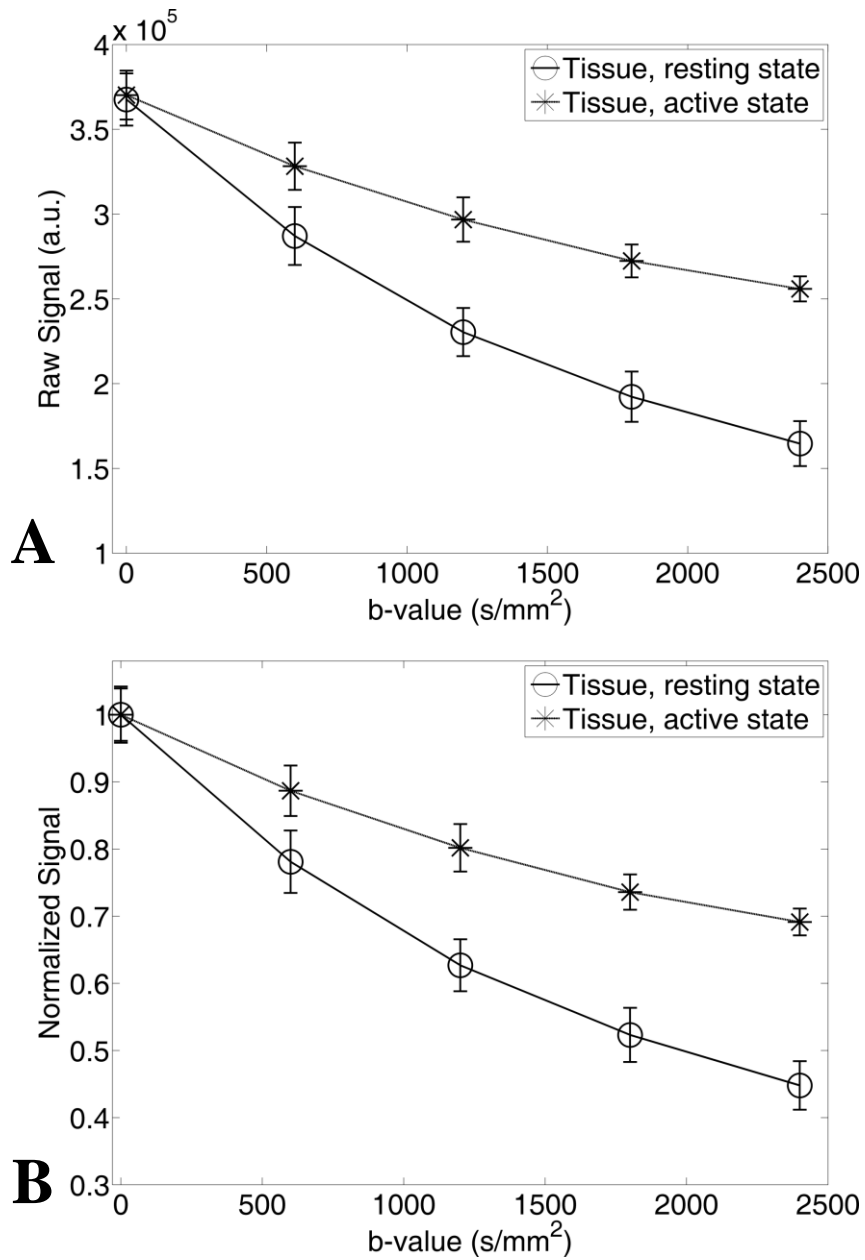


Figure 4-16. Diffusion signal decay curves from live hippocampal slice ($n = 6$) experiment generated from ROIs exhibiting the greatest magnitude of diffusion signal change before and after activation with kainate ($100\mu\text{M}$) in MK-801 ($10\mu\text{M}$) pretreated tissue. A) Raw diffusion signal attenuation curves for ROIs drawn in the CA1 region of the hippocampus before (circle) and after (asterisk) activation with $100\mu\text{M}$ kainate. B) Normalized data from the tissue ROI described in (A) illustrating that the curves diverge as diffusion weighting increases.

Table 4-1. Results of the biexponential analysis performed on normalized data from the live hippocampal slice experiment employing MK-801 pretreatment (10 μ M) followed by kainate activation (100 μ M).

	State	D_1 ($\times 10^{-4}$ mm ² /s)	D_2 ($\times 10^{-4}$ mm ² /s)	f	Δf
ROI 1	Rest	5.67	0.36	0.79	-0.43
	Active	5.67	0.36	0.36	
ROI 2	Rest	7.64	0.63	0.48	-0.22
	Active	7.64	0.63	0.26	
ROI 3	Rest	6.25	0.46	0.67	-0.36
	Active	6.25	0.46	0.31	
ROI 4	Rest	7.13	0.59	0.59	-0.24
	Active	7.13	0.59	0.35	
ROI 5	Rest	7.33	1.01	0.61	-0.24
	Active	7.33	1.01	0.37	
ROI 6	Rest	5.64	0.86	0.70	-0.43
	Active	5.64	0.86	0.27	

CHAPTER 5
DESIGN AND FABRICATION OF A MICROPERFUSION APPARATUS TO AID IN
MAGNETIC RESONANCE MICROSCOPY OF LIVE TISSUE SLICES

Introduction

During our previous investigations, we were able to collect—to our knowledge—the highest resolution MRM images of neural tissues to date by combining a powerful, high-field spectrometer (14.1T) with prototype microsurface coils thus attaining the high levels of signal needed to visualize mammalian cellular structures. Unfortunately, due to factors such as lengthy (≥ 7 h) scan times, these protocols required the use of fixed tissue specimen which revealed much in terms of structure but nothing in terms of physiology. Conversely, our studies in the live-slice model which focused on manganese uptake and neural activity were able to reveal distinct physiological processes occurring in neural tissue but, due to temporal limitations of the slice model related to tissue viability, could not attain resolutions high enough to reliably separate intracellular and extracellular compartments. In the following experiments, we attempt to combine the ultra-high resolution attained when using microsurface coils with our ability to perform MR measurements in living tissues. Achieving this goal required the design and fabrication of a MR-compatible microperfusion system that could be used with the current-generation microsurface coils.

Design Considerations

Modern tissue perfusion systems have advanced far beyond the humble beginnings of those employed in previously cited experiments conducted by Otto Warburg and Henry McIlwain. Some of the most highly evolved perfusion systems ever created have been developed by groups working in the field of tissue engineering (Choi et al., 2007; Khong et al., 2007). These systems use a series of microneedles to deliver perfusate deeper into excised tissue slices than can be readily achieved by diffusion processes thus circumventing mass transfer limitations:

a long-standing problem resulting from the inability to adequately perfuse tissue cores in excised samples greater than 300 μ m thick. While it has been shown these designs result in prolonged sample viability, factors such as their large size and use of materials incompatible with MR systems renders such designs useless for the purposes of live-slice MRM. Luckily, efforts have been made to engineer microneedles out of MR-compatible materials such as borosilicate glass and biodegradable, thermoplastic polymers opening the possibility for these techniques to be applied in MRI studies (McAllister et al., 2003). The simplest perfusion system designs combine thin ($\leq 300\mu\text{m}$) tissue slices with continuous or intermittent perfusate renewal. Such designs depend exclusively on diffusion processes for both the delivery of oxygen and trophic factors as well as the removal of metabolic waste products. It was a platform such as this that was used in our live-slice experiments in chapter 4 (Blackband et al., 1997; Espanol et al., 1996; Shepherd et al., 2002). Designs such as these are widely used in diverse fields of research and, as such, are available commercially from numerous biotechnology equipment suppliers. Unfortunately, the described spatial and compatibility limitations associated with our NMR hardware precluded the use of all commercially available tissue perfusion systems. What's more, the potential market for such a product is so limited that it is highly unlikely that any standardized, NMR-compatible tissue perfusion systems for use with ultra-high field spectrometers will become commercially available in the near future. Thus, like much of the equipment developed for use in specialized NMR experiments, our proposed perfusion rig was to be a one-off model designed specifically for our experimental needs.

When conducting excised tissue protocols which call for the maintenance of sample viability over the course of NMR experiments, additional considerations must be taken into account to ensure compatibility with the NMR system components. The most important of these

considerations is the ability to function within the spatial and functional limitations of the NMR scanner itself. Spatial limitations can be quite problematic for peripheral equipment design in NMR experiments regardless of its intended function. In horizontal systems which have been designed purposefully with the intention of performing *in vivo* NMR protocols, the bore dimensions are somewhat less restrictive and can often accommodate tissue perfusion apparatus—often modified to ensure MR compatibility—with relative ease (Atalay et al., 1993; Reeder et al., 1999). This issue becomes more problematic upon consideration of an ultra-high field magnet’s inherent bore narrowness and the litany of equipment—including shim gradients, imaging gradients, RF coils, and components contained within the probe body—required to fit inside these bore dimensions in order to perform the simplest of imaging experiments. When attempting to add something as complicated and cumbersome as a tissue perfusion apparatus to the 600MHz vertical-bore spectrometer used in the present experiments in addition to the components already mentioned, spatial considerations are of the utmost importance and influence more than any other factor the perfusion rig’s design.

Another principle concern is the use of NMR-compatible building materials. This factor limits the design, of course, to non ferromagnetic substances which excludes possible components containing nickel, cobalt and steel. Even paramagnetic materials such as titanium, aluminum and copper as well as various alloys containing these materials must be avoided due to their tendency to produce susceptibility artifacts (Ernstberger et al., 2007; Lauer et al., 2005; Matsuura et al., 2002; 2005). This limitation can be avoided almost entirely as most perfusion rig components can be fabricated from polymer resins. Commonly available commercial plastics such as polytetrafluoroethylene (PTFE) and polyoxymethylene (POM) are inexpensive, easily machined, and compatible with both MR imaging and biological systems; however, this issue

can still prove problematic when considering the use of peristaltic pumps to achieve perfusate flow (Badak et al., 2004; Vicente et al., 2006). Because the majority of these devices contain ferromagnetic components, care must be taken in preventing proximity to the spectrometer in order to ensure safety and reliable pump operation. Again, this appears to be an easily solved problem as increasing the length of perfusion lines can keep the pump apparatus from coming too close to the magnet; however, the use of long perfusion lines introduces alternative problems related to increases in the surface area of tubing through which perfusate must pass. Because plastic tubing is permeable to gas, chemical properties of the perfusate—most notably dissolved oxygen content, dissolved carbon dioxide content, and pH—will change as it passes through the perfusion system (Kania et al., 2005). In MRI experiments where perfusion lines can stretch to lengths of 6m or more, this factor influences perfusate characteristics so profoundly that additional testing at the site of the tissue well is necessary to guarantee the maintenance of physiological conditions.

Lastly, characteristics of the NMR technique can influence the operation and design of a perfusion apparatus. For instance, continuous tissue perfusion during an MRI experiment is not possible in most cases due to distortions imparted to images in the form of flow artifacts. This is a type of motion artifact—usually described in terms of vascular flow phenomena—in which excited spins contained in a flowing liquid are improperly rephased due to the change in position they experience as a result of the flow (Haacke et al., 1999). Flow artifacts can manifest differently depending on diverse factors including the type of flow—pulsatile or laminar—, its velocity and direction, and imaging parameters such as echo time and slice thickness. Multiple imaging strategies have been developed to compensate for flow artifacts, but are most effective when used to correct for laminar flow of constant velocity (Westbrook et al., 2005). As a result

of the various components and tissue samples contained within a perfusion rig, flow becomes turbulent when traversing these barriers and thus produces flow artifacts which are not amenable to removal by these means. Descriptions of NMR-compatible systems which avoid this issue and allow for constant perfusion have been reported (Wachowicz and Snyder; 2005). Alternatively, these flow artifacts can be eliminated by using an intermittent perfusion protocol interlaced with imaging periods as described previously (Chapter 4). While this method was convenient, care needed to be exercised to ensure its compatibility within the experimental parameters employed as a prolonged cessation of perfusate flow can lead to a buildup of toxic metabolites or a dearth of essential nutrients.

Methods

Fabrication of a MR-Compatible, Microperfusion Rig for Conducting Live-Slice MRM

Tissue retention apparatus

The problem of tissue placement in relation to the use of the microsurface coils was first encountered far in advance of our attempted live-slice experiments. All microcoils came equipped with tissue wells measuring 500 μm in depth. Our preliminary fixed-tissue experiments used 500 μm thick slices which could be held in place by the PCR film used to seal the well effectively pressing the tissue to the coil face and preventing slice movement when the coil was oriented vertically. Soon after our preliminary imaging, it became clear that a thinner tissue slice would be beneficial as it would allow us to see through the tissue to the coil face and determine exactly which portion of the sample was to be imaged. Predictably, when attempting to use a tissue slice thinner than the coil's well depth, as soon as the coil was switched from the horizontal to vertical orientation, the slice would drift away from the coil because nothing was holding it in place. Also, due to mass transfer limitations, it was understood that slices larger than 300 μm could not be used for live-slice, excised tissue studies conducted with the

microcoils. Clearly, if both fixed-tissue and live-slice microimaging studies were to proceed, a method to secure thin ($<500\mu\text{m}$) slices to the back of the tissue well and retain contact with the coil face was required. To achieve this end, we first fashioned a circular insert (4.5mm diameter, $60\mu\text{m}$ thick) out of a nylon mesh sheet (CMN-0053-C, Small Parts Inc.). Mesh weave with a $50\mu\text{m}$ pore size was selected to provide perfusate access to the tissue for live-slice experiments. To allow us to view the tissue underneath the mesh insert as well as prevent portions of the nylon mesh from entering images, a viewing window (2mm x 1.75mm) was positioned in the insert (Figure 5-1, A). This was accomplished by hand cutting with a surgical scalpel under a dissecting microscope to prevent fraying of the nylon filaments. The viewing window was offset to account for the coil's position being slightly off center in the tissue well. Next, to hold both the mesh insert and underlying tissue slice in place, a retention ring was fabricated out of a nylon washer (WN-M02-C, Small Parts Inc.). First, the central hole of the washer was enlarged to 4.76mm using a hand operated metal punch (Y-HP-K1, Small Parts Inc.). The thickness of the washer was reduced to $250\mu\text{m}$ by filing so that all components—sample, mesh insert, and retention ring—when stacked together would fit within the $500\mu\text{m}$ well depth. Finally, a notch was cut into the altered washer to finish fabrication of the retention ring component (Figure 5-1, B). Use of these two components prevented lateral movement and kept the slice from losing contact with the coil face during both fixed-tissue and live-slice experiments.

Perfusion well and lines

The well was designed with the intention of serving as the junction point in a liquid tight system connecting the coil's tissue well with the inflow and outflow lines. Because the tissue wells of the microcoils were circular in design, the face of the perfusate well that was to interface with the tissue well was made circular also. Available space for the perfusion well located

between the coil's tissue well and the inside of the micro5 gradient stack measured 8.85mm. Thus, a length of 7.6mm was chosen for the perfusion well to ensure clearance of the gradients upon probe assembly. A cylindrical plug (height = 7.6mm, diameter = 9.5mm) was machined from a piece of POM rod (ZRD-06-12, Small Parts Inc.) using a metal lathe. One end of this plug was bored out using a 6.75mm drill bit to make an open-ended barrel configuration which formed the body of the perfusion well. Because space was not available to run perfusion lines through the probe body, 12.6m of thin walled, PTFE perfusion lines (06417-31, Cole-Parmer) were introduced through the top of the spectrometer bore. Two holes (1.3mm) were drilled in the side of the perfusion well to accommodate placement of these lines (Figure 5-2). Also, a 1.3m length of surgical tubing (6429-13, Norton) was coupled to the inflow line at the point where perfusate enters the rig to ensure compatibility with the peristaltic pump.

Paraffin sealing gasket

The last component needed to complete the prototype microperfusion rig was a means by which to make a seal between the perfusion and tissue wells which was nonpermanent, liquid tight, both MR and biocompatible, and which conformed to the spatial limitations of the 600MHz micro5 probe body. Various early iterations composed of nonpermanent adhesives—such as rings made from commercial document mounting squares (3M, 859S) or double-sided PCR film—were attempted but all were ultimately unsuccessful due to an inability to maintain a liquid tight seal during preliminary testing. Ultimately, paraffin wax was chosen as a material to serve as a gasket for the microperfusion rig due to its superior sealing ability as a solid following the transition from a liquid state. The main challenge in using this material since the gaskets were not reusable was determining dimensions which could be regularly reproduced and which would contain sufficient wax to seal the rig but not so much as to close the gap between wells and inhibit perfusate access to the tissue. After testing various configurations, it was found that a ring

(outer diameter = 13.5mm, inner diameter = 8mm, thickness = 4mm) was able to meet these requirements. In order to ensure reproducibility, wax sheets of uniform thickness (4.2mm) were required. To control this fabrication, paraffin wax pellets (8002-74-2, Sigma-Aldrich) were weighed and introduced into a heated water bath (37401, Rival) containing deionized water of a known volume (1.5l). After all the paraffin pellets had melted, the heater on the bath was turned off and, upon cooling to room temperature, produced a uniform wax sheet on the water's surface. After a series of short experiments, it was determined that using 100g of paraffin in conjunction with the 1.5l water volume produced wax sheets of the desired thickness. In order to create forms for the repeated fabrication of paraffin rings, NMR tubes (513A-7PP, 515-3pp-4FB, Wilmad Lab Glass) were scored along their circumference using a silicon-carbide sharpening stone (08-930, Fisher Scientific) and snapped to yield two, open ended glass tubes. Paraffin wax disks were fabricated by heating one end of the 15mm tube using a handheld butane torch (R-36310-40, Cole-Parmer) and pressing the heated glass into the paraffin sheets. Lastly, paraffin rings (Figure 5-3) were created using the same techniques by pressing heated 8mm tubes into the centers of the paraffin disks.

Testing Perfusate Conditions in the Operational Microperfusion Rig

To ensure that sample slices were being maintained at near physiological conditions, a test was performed to measure perfusate pH, osmolality, and dissolved oxygen content at three points in the perfusion rig: the perfusate reservoir, perfusate well, and waste reservoir. These points roughly represent the beginning, middle, and end of the perfusate's path through the rig respectively. Initially, perfusate was adjusted to the desired tissue exposure conditions—pH = 7.3 to 7.4, osmolality = 300mOsm, dissolved oxygen content = 95% saturation—at the perfusate reservoir as was the standard protocol in previous live-slice experiments conducted in our laboratory (Blackband et al., 1997; Buckley et al., 1999; Bui et al., 1999; Shepherd et al., 2002;

2006a,b). After reaching the desired conditions as listed above, the peristaltic pump was activated initiating flow through the perfusion system at a rate of 2ml/min. The open face of the perfusate well was sealed with PCR film during this test in order to maintain a closed system and ensure perfusate would continue to flow through the entire rig. Once the flowing perfusate reached the end of the outflow line and began to fill the reservoir, a zero timepoint was initiated. Measurements of pH, oxygen saturation, and osmolality were taken at 10min intervals using a low-volume pH probe (6030-02-BNC, Mettler Toledo), dissolved oxygen meter (MI-730, Microelectrodes Inc.), and freezing point osmometer (5002, Precision Systems Inc.) respectively. This procedure was repeated three times over a 30min time period. The measurements were grouped based on the location of measurement and the means of each condition measured were calculated. The calculated values reflecting conditions at the perfusion well were then compared to the target conditions. Based on the differences calculated between our measurements and the target conditions, the perfusate contained within the initial reservoir was altered in an inverse linear fashion before the test was conducted again. This procedure was repeated until conditions at the perfusate reservoir were identified which yielded the specified target conditions at the perfusion well. Oxygen saturation of the ACSF was also monitored to ensure that pH adjustments did not dramatically reduce oxygen content available to the excised tissue slice.

Live-Slice Imaging of the CA1 region in Rat Hippocampus: A Pilot Study

Live-slice preparation and perfusion rig assembly

Adult (150g), male Sprague Dawley rats were anesthetized, euthanized, and their brains were dissected and mounted to a tissue cutting block as described previously (Chapter 3). Mounted specimen were immersed in an ice-cold bath of oxygenated ACSF (120mM NaCl, 26mM NaHCO₃, 1.5mM KH₂PO₄, 1.4mM MgSO₄·7H₂O, 2mM CaCl₂·2H₂O, 3mM KCl, 10mM Glucose; osmolality = 300mOsm, pH 7.4) and sliced into 300µm thick sections using a

vibratome. Following cutting, hippocampal sections were dissected from coronal brain slices and positioned in the 500 μ m diameter microcoil's tissue well so that the pyramidal cell layer in the CA1 region was traversing the coil's face. The coil was kept on ice prior to and for the duration of the sample placement procedure in an attempt to preserve slice viability by slowing metabolism. Following tissue placement, the nylon mesh insert was positioned over the tissue so that the pyramidal cell layer and underlying coil were visible through the insert's viewing window. Next, the nylon retention ring was inserted into the microcoil's tissue well securing both the mesh insert and tissue sample in place. A small amount of oxygenated ACSF solution was placed on the tissue to prevent dehydration during the rig sealing procedure. As paraffin is brittle at ambient temperatures, successful mating of the tissue and perfusion wells required controlled melting of the wax seals. First, a paraffin gasket was heated on one side using handheld butane torch. When the gasket's surface reached the phase transition temperature, the perfusion well was pressed against it immediately forming a liquid tight seal between the gasket and well. Next, the perfusion well with a gasket now attached was inverted and heated on the opposite side in the same manner. Once the gasket began exhibiting signs of phase transition, the perfusion well was pressed against the tissue well with the wax gasket positioned in between. Perfusion was initiated at a rate of 2ml/min immediately following the sealing procedure. An exploded schematic of all components within the perfusion rig illustrating the order in which they were assembled has been included (Figure 5-4). The integrity of the wax seal was confirmed by observing the rig until perfusate was seen exiting the outflow line. In the instances which the wax gasket failed to form a liquid tight seal, the described sealing protocol was repeated. If the case arose in which a seal could not be achieved in a timely manner (<15min), the experiment was aborted. Once the rig was securely sealed, the coil was oriented vertically and placed atop

the micro5 probe body before attachment of the gradient stack. Effluent from the outflow line was again confirmed to ensure the wax seal had not been compromised during attachment of the imaging gradients. Lastly, the probe body was inserted into the bottom of the magnet bore as the perfusion lines were simultaneously drawn from the top to prevent slack in the lines during probe insertion. Once the probe was secured in place, the outflow line was checked for perfusate flow once more to confirm the lines had not been obstructed.

Magnetic resonance microscopy of the CA1 region in live hippocampal slices

Following successful tissue placement, rig setup, and probe insertion, MRM of the CA1 region was performed. First, a diffusion-weighted pilot image (TR = 2000ms, TE = 36.1ms, Δ = 17ms, δ = 6ms, b = 4000s/mm², slice thickness = 300 μ m, resolution = 46.9 μ m in-plane, scan time = 2min8s) was collected to confirm that the pyramidal cell layer was positioned over the coil face. Provided the presence of the pyramidal cell layer was detected, a series of three MR scan protocols were performed. The first was a series of thirteen diffusion-weighted scans (TR = 2000ms, TE = 36.1ms, Δ = 17ms, δ = 6ms, slice thickness = 300 μ m, resolution = 46.9 μ m in-plane, scan time = 2min8s) which varied only in their diffusion weighting (b = 0 (10 effective), 100, 300, 500, 1000, 2000, 4000, 5000, 6000, 8000, 10,000, 15,000, and 30,000s/mm²). The second was a series of five diffusion-weighted scans (TR = 2000ms, Δ = 17ms, δ = 6ms, b = 2000s/mm², slice thickness = 300 μ m, resolution = 46.9 μ m in-plane, scan time = 2min8s) which varied only in their echo times (TE = 27.1, 30, 36, 40, and 50ms). The third was a series of four diffusion-weighted scans (TE = 27.1ms, Δ = 17ms, δ = 6ms, b = 2000s/mm², slice thickness = 300 μ m, resolution = 46.9 μ m in-plane) which varied in their relaxation (TR = 2500, 1000, 500, and 300ms) and, consequently, their scan times. The described protocols were repeated over a series of six total experiments; however, tissue movement during one experimental set lead to the

loss of one series of variable diffusion weighted data. Thus, we were left with $n = 6$ for the variable TE and TR datasets and $n = 5$ for the variable b-value data. This data was then used to compare the diffusion properties of the hippocampal subregions—stratum oriens, stratum radiatum, and pyramidal cell layer—as well as estimate their individual T_1 and T_2 values using a non-linear least squares fit (Marquardt, 1963) to the equation;

$$S = PD(1 - e^{-TR/T_1})e^{-TE/T_2}e^{-bD} \quad (5-1)$$

Where S is the MR signal taking into account T_1 , T_2 , and diffusion weighting, PD is the proton density signal, TR and TE are the repetition and echo times respectively, b is the diffusion weighting, and D is the apparent diffusion coefficient. The estimated T_1 and T_2 values for different regions were then tested for significant differences using ANOVA statistical analysis. The diffusion data was further separated into two groups based on datasets requiring a normalization step to eliminate variability in the noise ($n = 2$) caused by variability in the receiver gain settings during image collection and datasets collected with equivalent gain values ($n = 3$). Signal decay plots of the variable diffusion weighted data were compiled so that the diffusion properties of the tissue subregions under investigation could be examined.

Results

Testing Perfusate Conditions in the Operational Microperfusion Rig

Following the first series of experiments in which ACSF was adjusted to the target conditions at the perfusion reservoir, it was noted that these conditions were not retained at the perfusion well. A trend of decreasing dissolved oxygen content and increasing pH was observed as the perfusate traversed the rig so that these conditions were evident in the perfusate well, but became even more pronounced in the waste reservoir (Table 5-1). Osmolality readings were stable in measurements performed throughout the rig at various pH and dissolved oxygen levels and, as such, did not require further adjustment. A second series of tests in which pH levels were

adjusted to 7.2 at the perfusate reservoir failed to achieve the target conditions at the perfusion well (Table 5-2). A third series of experiments in which the pH of the ACSF in the perfusate reservoir was adjusted to neutral conditions yielded pH values at the perfusion well in the physiological range (Table 5-3). The percent oxygen saturation fell slightly (60.5% at pH = 7.56 to 57.1% at pH = 7.38) following pH adjustment.

Live-Slice Imaging of the Pyramidal Cell Layer in Rat Hippocampus: A Pilot Study

Mean T_1 values calculated for the pyramidal cell layer, stratum radiatum, and stratum oriens were 2266 ± 352 ms, 2218 ± 374 ms, and 2287 ± 367 ms respectively (Figure 5-5, A). Mean T_2 values calculated for the pyramidal cell layer, stratum radiatum, and stratum oriens were 88 ± 38 ms, 71 ± 22 ms, and 77 ± 24 ms respectively (Figure 5-5, B). Analysis of variance indicated no significant differences between tissue subregions thus obviating the need to perform additional statistical analysis. Diffusion signal decay curves revealed a consistent pattern in which the tissue region corresponding to the pyramidal cell layer exhibited higher diffusion than either the stratum radiatum or stratum oriens (Figure 5-6). This pattern was observed regardless of the analysis method employed and was thus present in graphs of both raw and normalized data.

Discussion

Fabrication of a MR-Compatible, Microperfusion Rig for Conducting Live-Slice MRM

Following an extensive period of prototype fabrication coupled with functional testing both outside and inside the imaging spectrometer, we arrived at a microperfusion rig design capable of supplying a continuously renewing influx of fresh perfusate that was compatible with the unadulterated Bruker microsurface coils and which operated within the spatial limitations of our magnet system. However, additional testing of perfusate conditions revealed that our ACSF solution was undergoing changes as it passed through the rig creating dissolved oxygen and pH gradients. These phenomena presumably resulted from the loss of dissolved O_2 and CO_2 gas

from within the ACSF perfusate leading to the observed decrease in oxygen concentration and increase in pH (Davenport, 1974). As the perfusate traversed the interior of the rig, dissolved gasses were permitted to escape from the perfusion lines due to the gas permeability of the tubing used. Perfusate which had spent more time inside the tubing—and was therefore farther along in the rig—had lost more dissolved gasses to the atmosphere accounting for the spatially dependent pattern of the reported measurements. As a consequence of this occurrence, conditions at the site of tissue perfusion did not initially fall within the target conditions for optimal neural tissue metabolism. Correcting for the difference in pH required increasing the acidity of our ACSF solution at the perfusate reservoir to offset the unwanted increase in alkalinity. This step ensured that the pH at the perfusion well was kept within the desired physiological range (7.3 to 7.4). Correcting for the loss of dissolved oxygen from the perfusion rig; however, was not possible using this strategy. The oxygen concentration of the carbogen gas (95% O₂, 5% CO₂) was high enough that using pure oxygen—thus increasing the total concentration of O₂ an additional 5%—would not have offset the nearly 40% decrease in dissolved O₂ observed in ACSF passing from the perfusate reservoir to the perfusion well. Moreover, because the microperfusion rig's openings are located at its ends when the perfusion well is sealed onto the microcoil, induction of gas at a position closer to the site of tissue perfusion was not possible using the current design. Regardless of this limitation, data from previous studies conducted in neural tissue suggest that hippocampal slices such as those which we employed in our experiments should exhibit normal metabolic behavior at the pH range and oxygen levels reported. Previous studies have described sustained metabolic rates for brain tissue in an equivalent perfusate—Ringer's solution—at percent oxygen saturation ranging anywhere between 100% and 50% (Skolnik et al., 1966). In experiments measuring dissolved oxygen

content within the interstitial space of multiple brain regions in the rat model, a range of 5 μ M to 80 μ M has been reported (Wang et al., 2003) with measurements in the hippocampal formation ranging from 50 μ M to 70 μ M (Andreasen et al., 1997). A dissolved oxygen concentration of 57.1% corresponding to 6.7e⁻⁴ mol/l or 21.44 mg/l of dissolved gas contains approximately ten times the level of dissolved oxygen in even the most oxygen rich regions of the rat hippocampus measured *in vivo*: 70 μ M or 2.24mg/l. After performing these measurements and comparing them with values found in the literature, we were confident that the metabolic demands of the hippocampal slices employed in our live-slice experiments would be adequately met despite the unanticipated drop in the oxygen content of our ACSF perfusate. While we were ultimately able to attain perfusate conditions within boundaries amenable to hippocampal slice metabolism, the pH adjustments and measured oxygen content are applicable only to the rig as it is currently designed. This is a disadvantage in the sense that, if the perfusion lines which are in use require adjustment, replacement, or any other alteration which could affect their composition or length, new experiments would need to be conducted to ensure optimal perfusate conditions at the tissue slice are maintained. With this existing limitation in mind, future rig designs will incorporate perfusion lines which can pass through the probe body allowing the perfusion well to enter the magnet bore from the bottom rather than the top. This configuration will permit a significant reduction in the length of the lines and presumably a significant reduction in the loss of dissolved perfusate gasses as well.

Live-Slice Imaging of the CA1 region in Rat Hippocampus: A Pilot Study

Although we were able to collect multiple datasets in the desired lamina of live slices from rat hippocampi using the microperfusion rig, data analysis following our initial experiments revealed high levels of within-group variability. This contributed to the large error values

reported in the variable TR and TE experiments as well as the distance between diffusion signal decay curves of the same tissue group in the analysis of our variable diffusion weighting experiments. Several factors could have contributed to these problems and will need to be addressed systematically prior to conducting additional live slice studies. First, an experiment detailing the temporal limits of tissue viability in the microperfusion rig should be performed to determine the timeframe over which tissue remains stable under the perfusion conditions described. Arguably, this experiment should have been performed prior to the commencement of our pilot studies as part of rig characterization. We attempted to avoid this issue in our preliminary experiments by limiting the scan time during our live-slice protocol (45min) thereby eliminating the possibility of variability caused by tissue instability given previous findings that hippocampal slices remain stable for 12h during acute slice preparations (Pakhotin et al., 1990). As such, the variability observed in our MR data is not likely to have originated from tissue changes during the MR experiment but cannot be ruled out pending additional investigation. It is also possible that variations in the distance between tissue slices and the coil face caused the described variability. Another explanation for the described variability which has not been tested is the possibility that the wax sealing procedure caused a heat shock injury which varied in severity between experiments (Barr and Dokas, 1998). Because care was taken to isolate the butane flame to components not in contact with the slice itself and because the coil components that contacted melted wax insulate well against heat, this possibility is highly unlikely. While every attempt was made to slow metabolism in the slices and decrease the time spent without exposure to oxygenated ACSF, limitations inherent to the current experimental protocol could have contributed to the variability in our live-slice data by introducing variability in the agonal state of our tissue slices. As stated in the methods, experiments in which the perfusion rig could

not be sealed in a period of 15min or less were considered to be failed attempts because it was assumed that lack of perfusion in excess of this time would have contributed to significant tissue degradation. However, this figure was based on the standard amount of time it took to assemble the perfusion apparatus during the average experiment rather than a detailed account of the subtle tissue changes occurring over this time period. Although it is not always possible to draw direct parallels due to differences in experimental protocols, previous studies conducted at physiological temperatures (37.5° C) have reported tissue damage to brain slices in as little as 6min to 10min following oxygen and glucose deprivation (Jarvis et al., 2001). While it was common for setup prior to perfusion to take 10min or more due to the challenges of the sealing procedure, some of the experiments included a sealing procedure which was successful on the first attempt leading to variability in the time period prior to perfusion. Because testing the rig's seal involved commencement of the perfusion process, it was not practical to standardize this time interval by delaying the onset of perfusion. Furthermore, we determined this practice would likely be more detrimental than beneficial to the data as time spent without exposure to necessary metabolites contributes to ischemic damage. Clearly, if the period between tissue harvesting and commencement of perfusion is to be shortened, fundamental changes to the current protocol and rig design are needed. First, decreasing the overall time and success rate of the sealing procedure is imperative to reducing this time interval. The wax sealing protocol was by far the most time consuming portion of this procedure as well as the step most likely to fail and thus be responsible for termination of the experiment. As such, a new protocol for sealing the rig has been developed featuring an o-ring style closure that functions using light compression to maintain contact between the perfusion well and coil (Figure 5-7). The o-ring itself (Small Parts Inc., ORS-010-25) has an inner diameter of 6.35mm, outer diameter of 9.525mm, and is made of silicone.

Although we have not used the improved rig for live-slice experiments, initial bench tests of this design resulted in a 100% success rate for achieving a leak-proof seal on the first attempt in three separate tests as well as a drastically reduced overall time (approximately 1min) from the tissue securing step to the sealing of the perfusion rig. Also of note, the new design requires no exposure to flame, meets our biocompatibility requirements, and works regardless of whether components are wet or dry prior to sealing: a primary cause of failure in the case of the wax seal being thin films of residual ACSF.

Another important issue in regards to our live-slice data is the apparent lack of between-group variability in our T_1 and T_2 analysis of the different tissue types. Within group variability is still present—presumably for the same reasons discussed above—but the expected differences of T_1 and T_2 values between tissue types failed to materialize. Moreover, while our estimated T_2 values for hippocampal subregions came close to values reported in the literature—80ms to 110ms—for whole hippocampal measurements (Duncan et al., 1996; Oertzen et al., 2002; Woermann et al., 1989), our estimates for T_1 were over twice values previously reported for human hippocampus (Kiefer et al., 2004). This disparity is more likely due to shortcomings in our MR scan protocol and estimation rather than our perfusion protocol. First, the VTR and VTE scan series which we used to calculate T_1 and T_2 values respectively contained rather heavy diffusion weighting ($b = 2000\text{s/mm}^2$) to aid in visualization of the pyramidal cell layer by sacrificing available signal. The diffusion scan protocol necessitated the use of relatively long echo times (minimum TE = 27.1ms) which further reduced available signal in the initial measurements. It is our feeling that employment of the described scan protocols resulted in estimation errors caused by mixed weighting parameters. It is worth noting that our T_1 and T_2 estimates are far closer to values reported for acute slices of rat cortex (Shepherd et al., 2009)

and hippocampal slice cultures (Shepherd et al., 2006b). These observations may suggest that tissue treatment during the live-slice protocol could result in the disparity between T_1 values estimated from *in vivo* human and *ex vivo* rat experiments. Subsequent studies will make use of alternate pulse programs to attain images with better distributions of T_1 and T_2 weighting as well as less diffusion weighting in hopes that the accuracy of our estimated T_1 and T_2 values will improve.

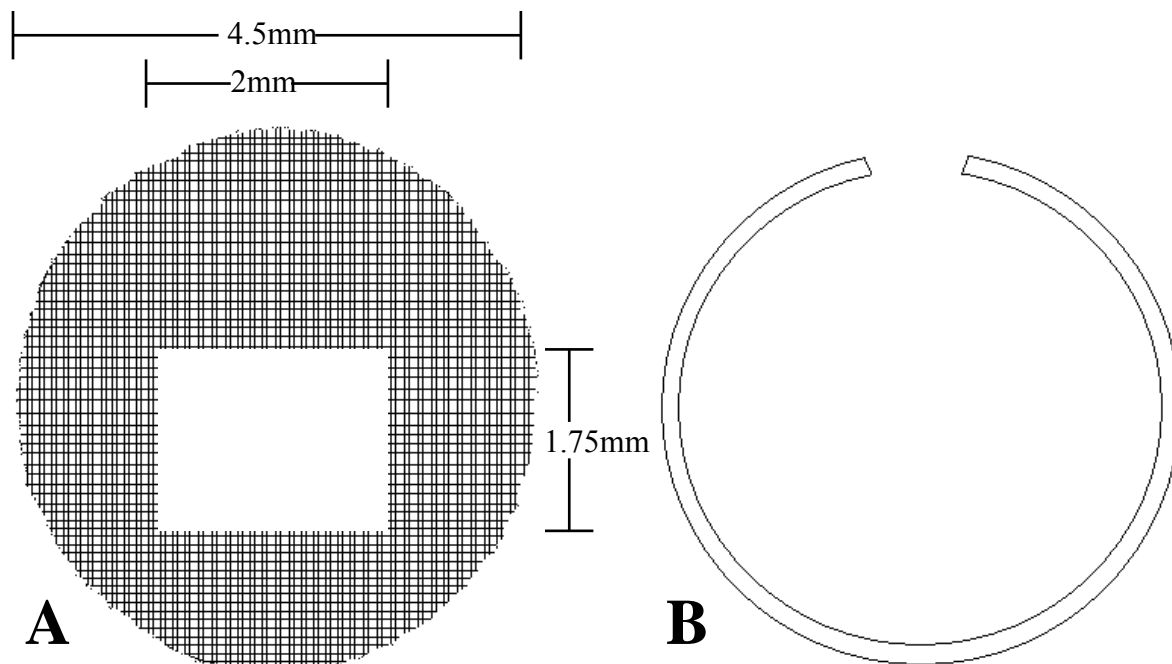


Figure 5-1. A schematic drawing of the components which comprise the tissue retention apparatus used in both fixed-sample and live-slice imaging experiments employing the microsurface coils. A) The first component consisted of a circular, nylon mesh disk 4.5mm in diameter with a 2mm x 1.75mm cutout centered in the horizontal plane but positioned 1.5mm lower in the vertical plane to ensure proper overlap with the surface coil. B) The second component consisted of a flexible, nylon retention ring (250 μ m thick) used to hold the mesh insert—and thereby the tissue slice—in place during the course of the MR imaging experiments using microsurface coils.

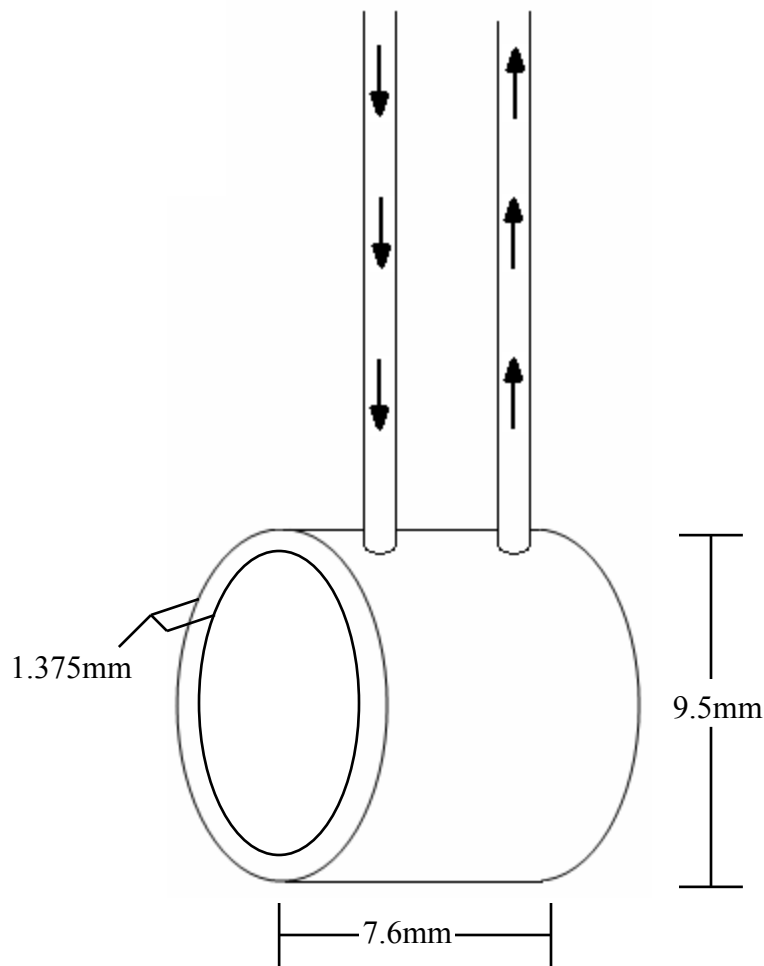


Figure 5-2. A schematic drawing of the microperfusion well component with PTFE perfusion lines extending from the well's top. The open-barrel shaped perfusion well was machined from polyoxymethylene rod. In this diagram, the open ended section (left) is intended to interface with the circular tissue well located on the microsurface coil. Perfusion lines represent inflow from the perfusion reservoir (down arrows) and outflow to the waste container (up arrows). The inflow line was placed closer to the interface with the tissue slice as it was thought that proximity to fresh perfusate might aid in sustaining slice viability.

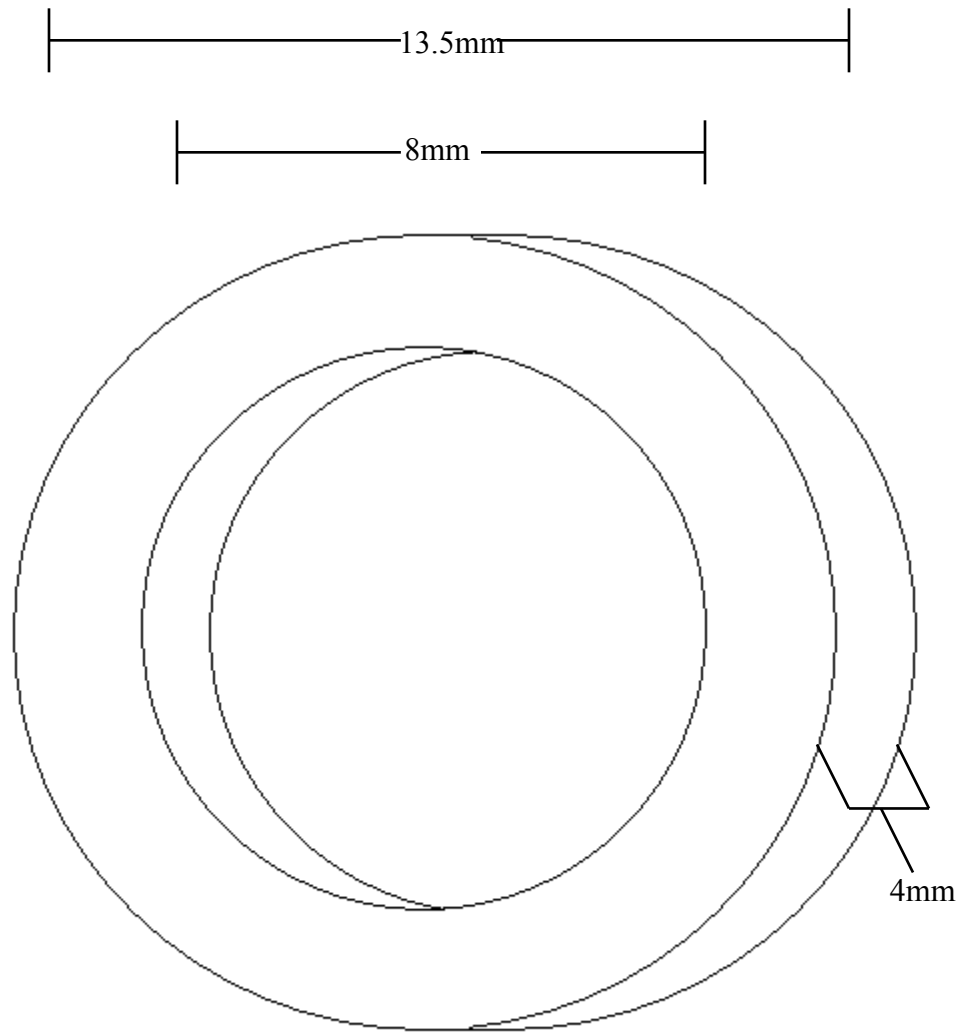


Figure 5-3. Schematic drawing of a wax gasket used to seal the microperfusion rig during live-slice experiments. Each gasket was hand fabricated from wax sheets made by melting and cooling MR and biocompatible paraffin wax pellets.

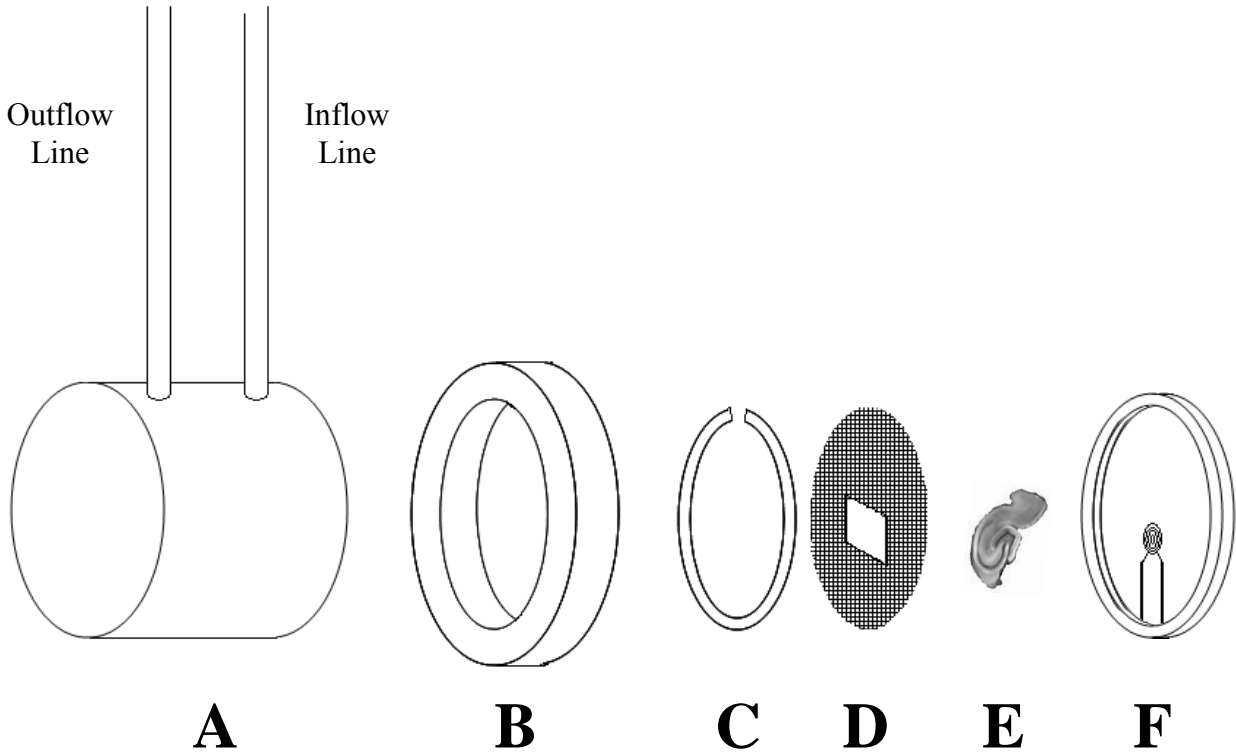


Figure 5-4. An exploded diagram of the microperfusion rig illustrating the order of assembly during our live-slice experiments. The separate components represented in the schematic are A) the perfusion well, B) a paraffin wax gasket, C) the retention ring, D) the mesh insert, E) a hippocampal slice, and F) the microcoil and its surrounding tissue well.

Table 5-1. Results of experiments chronicling pH, osmolality, and percent dissolved oxygen measurements of ACSF in the operational microperfusion rig. In this series of experiments, ACSF located in the perfusate reservoir at the beginning of the perfusion rig was adjusted to conditions (pH = 7.4, osmolality = 300mOsm, dissolved oxygen = 95%) which were intended to maintain viability of the tissue slice located at the perfusate well.

		Perfusate Reservoir	Perfusate Well	Waste Reservoir
Experiment 1	pH	7.40	7.56	7.70
	mOsm	301	303	302
	% oxygen	95.0	60.4	43.0
Experiment 2	pH	7.39	7.55	7.72
	mOsm	302	300	304
	% oxygen	95.1	60.4	43.1
Experiment 3	pH	7.40	7.58	7.73
	mOsm	299	301	301
	% oxygen	95.0	60.6	43.1
Averages	pH	7.40	7.56	7.72
	mOsm	301	301	302
	% oxygen	95.0	60.5	43.1

Table 5-2. Synopsis of the second series of experiments measuring pH taken at different locations in the microperfusion rig during operation. In this set of experiments, perfusate reservoir pH was adjusted to 7.2 prior to initiation of the experiment in an attempt to achieve target conditions at the perfusion well.

	Perfusate Reservoir pH	Perfusate Well pH	Waste Reservoir pH
Experiment 1	7.20	7.44	7.63
Experiment 2	7.19	7.45	7.62
Experiment 3	7.20	7.43	7.60
Average	7.20	7.44	7.62

Table 5-3. Results of the third set of experiments attempting to produce the desired perfusate conditions at the perfusate well. Adjusting the perfusate reservoir ACSF to neutral pH levels resulted in physiological pH conditions at the perfusate well. The percent dissolved oxygen was measured in this series of experiments to ensure that the pH alterations had not affected these values.

		Perfusate Reservoir	Perfusate Well	Waste Reservoir
Experiment 1	pH	7.00	7.37	7.63
	% oxygen	95.1	57.0	44.4
Experiment 2	pH	6.98	7.38	7.62
	% oxygen	95.0	57.2	44.3
Experiment 3	pH	6.99	7.40	7.60
	% oxygen	95.0	57.0	44.4
Average	pH	6.99	7.38	7.62
	% oxygen	95.0	57.1	44.4

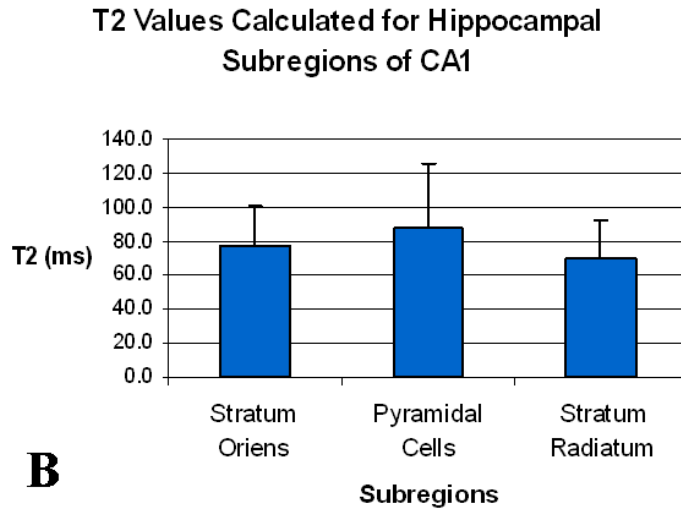
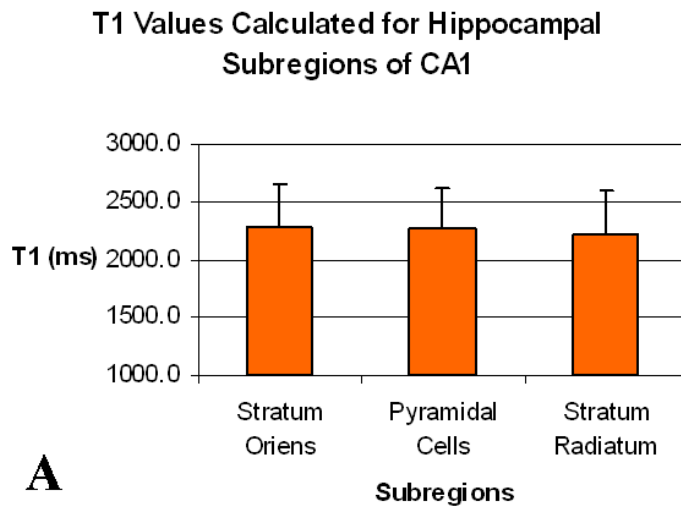


Figure 5-5. Mean values of T_1 and T_2 estimated from variable TR and TE live-slice experiment data ($n = 6$) respectively. A) T_1 values. B) T_2 values. Error bars are representative of within-group standard deviations. ANOVA statistical analysis revealed no significant between-group differences in either experiment.

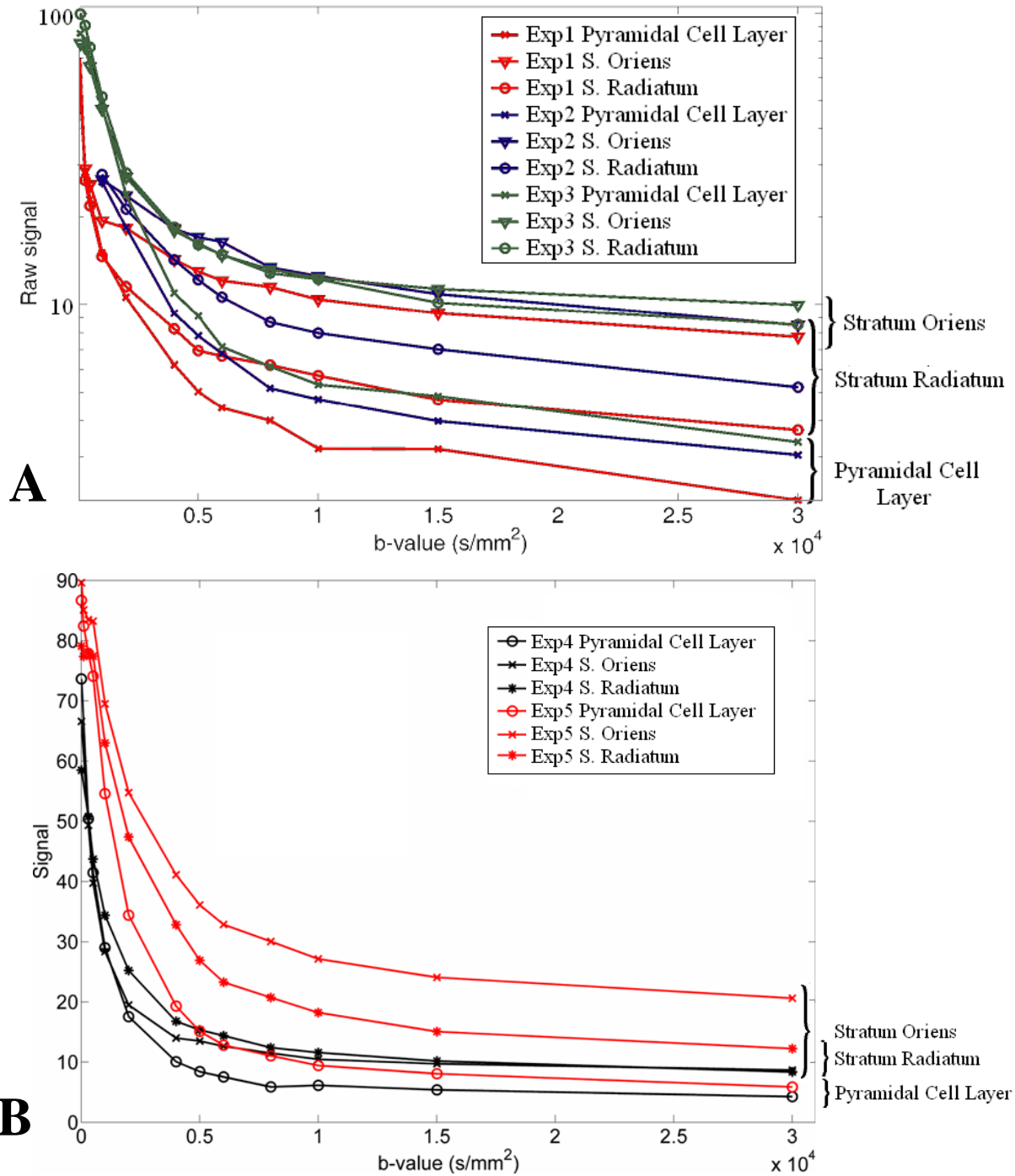


Figure 5-6. Diffusion signal decay curves from live hippocampal slice ($n = 5$) experiments showing signal changes in CA1 tissue layers as a function of diffusion weighting. A) Results of experiments conducted at equivalent receiver gain values. B) Results of experiments which employed a normalization step to account for variability in receiver gain settings. Although significant variability exists within tissue groups, a clear pattern emerges at high diffusion weighting in both analyses in which pyramidal cells exhibit the highest diffusion rates while tissue of the stratum radiatum and stratum oriens show lower diffusion rates with overlapping diffusion signal values.

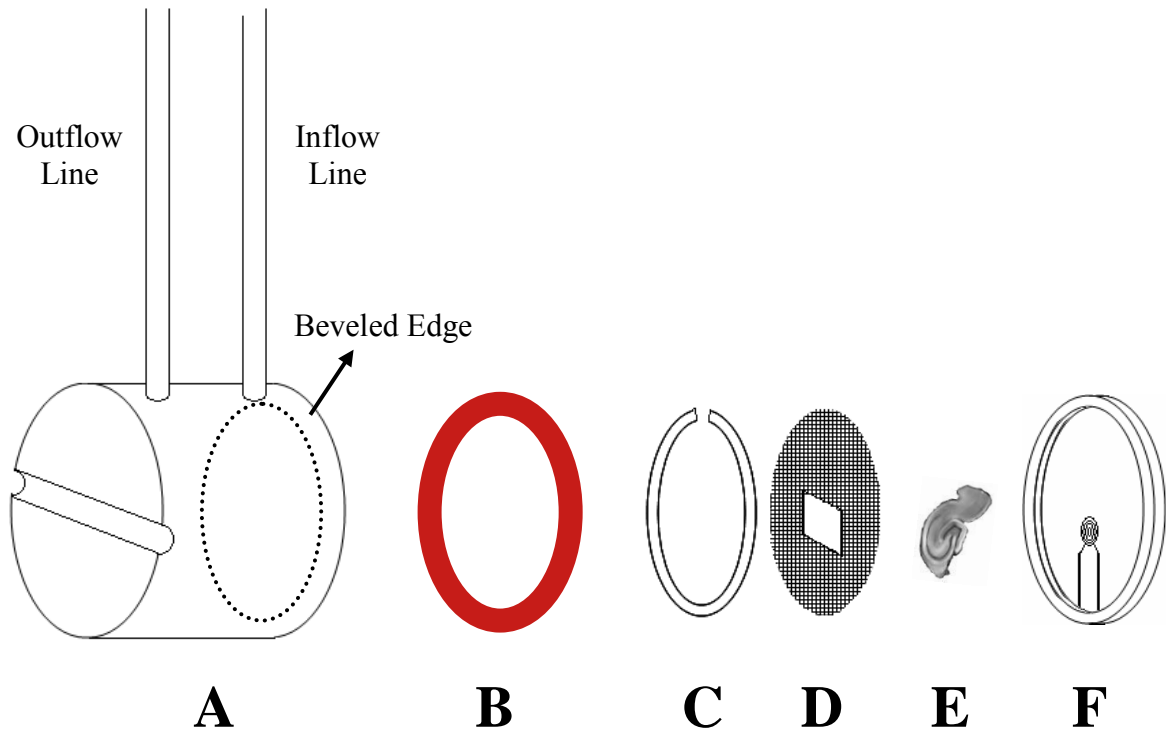


Figure 5-7. An exploded diagram illustrating the improved microperfusion rig design. The separate components represented in the schematic are A) the perfusion well, B) a silicone o-ring gasket, C) the retention ring, D) the mesh insert, E) a hippocampal slice, and F) the microcoil and its surrounding tissue well. Components C, D, and E remain unchanged from the previous design. Component A has been given a beveled edge on its open end to better accommodate the o-rings rounded profile while a groove to accommodate a band-style pressure fitting has been added to components A (pictured) and F (not pictured).

CHAPTER 6 CONCLUSIONS AND FUTURE DIRECTIONS

Identification of Hypointense Microstructures in Striatal MRM Images

Due to our inability to garner correlative datasets between MR and light microscopy images during preliminary studies in the mouse striatum, direct histological evidence for the structural origins of the hypointense microstructures was not forthcoming. Given that the spatial and morphological observations seemed to suggest iron-rich haemoglobin could be responsible for some but not all of the hypointense structures seen in our MR images, we concluded that a non-ferric source of signal contrast could be responsible for at least a portion of the microstructures observed. While these observations alone provided no conclusive evidence as to the structural origins of the signal contrast, the findings influenced subsequent studies in the hippocampus and spinal cord which revealed novel insights into the origin of MR signal as it relates to tissue structure at the cellular level. First, it was noted that similar hypointense contrast can be achieved through both diffusion and non diffusion-weighted scan parameters inside cell body-rich laminae of the hippocampus. Perhaps most importantly, similar contrast was observed upon imaging of individual alpha-motor neuron cell bodies in the ventral horn of the spinal cord. These experiments represent the first time that the cell bodies of mammalian neurons were imaged using MRI techniques and show that these perikarya appear darker than the tissue layers which surround them. This finding is quite significant in that it suggests a higher intracellular than extracellular rate of diffusion. This finding is discussed in greater detail in the section regarding interpretation of diffusion data, but—for the purposes of helping identify the microstructures observed in the striatum—it is significant because it shows that cell bodies can manifest as hypointense signal regions in diffusion-weighted MRM images. While this is not direct evidence of the microstructures' structural origin, coupled with the supporting evidence

that suggests they are not caused by noise artifacts, air bubbles, or iron deposits we can say that the structures most likely to have caused the appearance of the hypointense regions are a mixture of haemoglobin from pooled blood and striatal cell bodies.

Clinical Relevance of MRM in Biological Tissues

One of the most frequent criticisms leveled at MRI performed with microcoils is that because the methodology cannot be used as a clinical tool it therefore has no relevance to clinical medicine. Furthermore, tissue microstructure is readily accessible via various light microscopy techniques—which are cheaper, offer better resolution, and are more widely available than MRI—thus relegating MRM analysis techniques to obsolescence prior to their development. Although the logic of these arguments is arguably flawed, the views presented in them are quite valid. Contemporary MRM techniques cannot compete with biopsy protocols already in clinical use and therefore cannot improve these methods of diagnosis. Likewise, if MRM of tissue slices offered nothing more than relatively low resolution, black and white images obtained over long periods of time at great expense, it would be nothing more than an anachronistic curiosity hardly worthy of a historical footnote. Given a cursory investigation, it would seem that MRM does not have much to offer the field of clinical medicine. Putting aside some of the less obvious potential future applications of MRM, these techniques still have a great deal to contribute to modern medicine. Magnetic resonance microscopy currently has the potential to reveal the compartment-specific origins of NMR signal in mammalian tissue by means which are directly observable and therefore unambiguous. Critics that are willing to concede this point might argue that, because clinical scanners cannot approach the resolution levels of research spectrometers, possessing knowledge of how cellular compartmentation influences the NMR signal is of no benefit to diagnostic medicine. This is yet another misconception that originates from overemphasizing the methodology and technical aspects of the MRI experiment. In fact, data from high-resolution

MRI studies can be used to offer more accurate descriptions of tissue behavior which can be applied to the interpretation of lower resolution MRI data such as those collected at clinical field strengths. These modeling procedures, while subject to the errors common to all modeling, will offer a more accurate representation than those currently available. This is mainly due to the fact that current models which attempt to describe properties of microscopic tissue environments by interpretation of diffusion data have been developed using data gleaned from tissue studies conducted at macroscopic resolutions (Anderson et al., 2000; Niendorf et al., 1996; Sekino et al., 2006; Zijl et al., 1991). While it may seem counterintuitive to make inferences such as this, it is important to remember that model development is an iterative process and the models described in these publications were developed within the confines of the technology available at the time and place of their creation. By using MRM data taken at resolutions high enough to allow for visualization of cellular structure, we hope to contribute to a new understanding of how compartmentation in tissue affects the NMR signal which will in turn lead to more accurate modeling of diffusion data and improve our diagnostic capabilities in the clinic. Only by investigating the microstructural origins of MR signal change related to pathology in tissues will we be able to fully realize the potential of MRI as a clinical diagnostic tool and transform it from its current state into a modality capable of detecting the earliest and most subtle changes wrought by disease.

Interpretation of Diffusion Data in Biological Tissues

Diffusion Data and Tissue Compartmentation

To date, descriptions of the microstructural environment in biological tissues have focused on the interpretation of diffusion data: mainly, how changes in diffusion signal decay curves generated by NMR experiments examining tissues under various perturbations can be attributed to changes occurring in the tissues' microstructure. As discussed in the previous

section, the current body of work regarding this topic was generated using MR techniques that relied on indirect observation of the tissue changes described within. As a result, some of the fundamental conclusions drawn from these experiments were found to be incorrect upon further investigation. One such assertion being that the fast and slow diffusion components described by the biexponential diffusion model can be accounted for by diffusion behavior involving water exchange between the extracellular and intracellular water pools respectively (Benveniste et al., 1992). Arguably, the most egregious of these erroneous conclusions was that, due to factors such as higher intracellular restriction, protein content, and viscosity the rate of diffusion must be greater in the extracellular space than in the intracellular space (Niendorf et al., 1996). If this were a true representation of the diffusion properties exhibited by biological tissues, we would expect cell bodies to appear brighter than the tissues surrounding them in diffusion-weighted images and exhibit lower apparent diffusion values. The data presented in this work—being the first to describe cell bodies in mammalian tissue by direct observation—clearly shows the opposite to be true. While a thorough explanation as to how changes in tissue microstructure affect the NMR diffusion signal will have to wait for perturbation studies conducted at subcellular resolutions, it is possible to speculate on why water diffusion rates differ between cellular and extracellular compartments. From a structural standpoint, the interiors of cells contain far more membrane barriers than the relatively interconnected extracellular space. Also, while the specific density of interstitial space has not been measured directly, previous non-MR based diffusion analysis have likened it to cerebrospinal fluid with a sparse matrix consisting primarily of glycosaminoglycans and proteoglycans (Nicholson and Syková, 1998). These factors would seem to reinforce the expectation of high extracellular and low intracellular diffusion which this work has shown to be false. Because pyramidal cell bodies in the

hippocampal CA1 pyramidal cell layer show high apparent diffusion rates in live-slice studies, it may be tempting to attribute this finding to proton dephasing caused by cytoplasmic streaming which results from biological mechanisms occurring within the cell itself as part of normal physiological processes. In this case, intracellular water would exhibit higher than expected apparent diffusion because of the confounding mechanistic influence of operational cellular machinery. However, this hypothesis alone cannot explain the phenomenon of high intracellular diffusion because—if this were the case—we would expect to find low intracellular diffusion within fixed tissue samples in which all of the membranous structures remained intact but all physiological processes had ceased. This scenario is contrary to the evidence provided by our diffusion-weighted images of cells in fixed hippocampal and spinal cord samples. Moreover, the reported rates of cytosolic streaming in animal cells are quite low (5 to 20 $\mu\text{m}/\text{min}$) when compared to diffusion rates of water in brain tissue (Serbus et al., 2005; Wolke et al., 2007). While the experimental findings presented in this work cannot be adequately explained within the confines of our current understanding of water diffusion, restriction, and compartmentation in biological tissues and how each affects the NMR signal, it is our hope that future MRM studies focusing on signal origin at the cellular level will lead to a new, more accurate representation of the NMR properties of tissue microstructure.

Diffusion Data and Functional Imaging

This work represents the first instance in which attempts were made using MRM methods to visualize neuronal swelling as it relates to cell activation in the absence of confounding flow effects induced by blood circulation. While this effect is well documented in optical and electrophysiological studies, our ability to observe it using MRI techniques is still being debated. Doctors Le Bihan and Darquie have reported seeing diffusion signal changes in functioning areas

of human brains; however, similar results have yet to be confirmed by independent groups. Critics of their work often point to the effects of vascular flow as an alternate explanation for the observed diffusion signal changes. While the study in the present work was able to record diffusion signal changes in brain slices related to neural activity—and thus show that the effects of neuronal activation can be measured in the absence of flow effects—it cannot definitively end the debate on diffusion-weighted functional imaging for numerous reasons. First, the electrical activation of cells for the purposes of our experiments was far different than the electrical activity associated with normally functioning cells. The bath exposure to elevated potassium or kainate employed in our protocol is known to result in sustained, global cellular activity in the hippocampus. The patterns associated with this type of activation are commonly known as bursting or seizing and represent short (100ms) or sustained (several seconds) periods of elevated electrical activity respectively (Netoff et al., 2004). Traditionally, this type of activity is associated with excitotoxicity (Monasterio et al., 2008). Both bursting and seizing behavior exhibit higher rates of cell firing than those recorded from normally functioning tissue and are, therefore, not directly comparable. It is important to note however that the diffusion changes—shift from fast to slow diffusion in the biexponential model—reported in our study are nearly thirty times greater than those reported by Le Bihan. The observation that the measurable effect on diffusion was larger in our study could possibly be accounted for by the disparity between normal and chemically induced firing rates or the additive effect caused by temporal differences between spin echo and echo-planar scan protocols. These explanations are, of course, speculative and the contributing factors to this rather large difference in diffusion measurements will not be elucidated without further study. Lastly, in regards to the previous *in vivo* studies, our findings support the assertion that the effects of neural activity can be observed using diffusion-weighted

imaging in a model system free from the possibility of flow artifacts; however, it does not support or refute that the signal changes observed by Le Bihan and Darquie were due to neural firing. Again, due to the differences in experimental models, the results of our studies are nearly impossible to compare without making unfounded and thus inadvisable assumptions about the mechanisms at work behind the described signal changes. Clearly, in order to generate stronger evidence in favor of diffusion-weighted functional imaging, the methodologies of our slice protocol need refinement so as to more closely mimic the activation patterns found during normal neural cell communication.

Future Directions

Fabrication of a Helmholtz-Pair Style Microcoil Array

The microsurface coils employed in our experiments represent a step forward in the science of RF coil engineering as they have allowed us to visualize structures not previously imaged using MR methods. For all of their usefulness however, alterations in the basic design of these coils could vastly improve their usefulness and applicability to biological science. The largest draw back by far when using the microcoils is the inherent dearth of surface area excited by the coil face. This becomes more problematic as ever smaller coils are used to attain MR signal gains and leads to an instance of diminishing returns as the coil's field of view shrinks to a size that cannot contain materials of biological interest. Also suffering in this instance is the ability to reliably position samples containing items of interest over the microsurface coil face. This procedure is still performed by hand—albeit with the aid of a dissecting microscope—and does not offer the luxury of sample adjustment following positioning. This means that samples experiencing unwanted shifts on even the micrometer scale often do not contain the structure that were the intended focus of the imaging. This, of course, is often not realized until after

preliminary imaging is completed leading to lost resources in the form of research subjects, working hours, and machine time.

Recently, a 128-coil array used for the purposes of cardiac imaging was described in the literature (Schmitt et al., 2008). Phased-array technology has traditionally been used to improve SNR and shorten scan times, but the same principle could be employed in a new microcoil design to increase the field of view in a MRM experiment. All the necessary system elements exist to accommodate this proposed design, i.e. no technological breakthroughs would be required to occur prior to its development. The process of designing, fabricating, and testing such a coil would require a large commitment of time and resources from personnel skilled in both RF technology and microfabrication techniques; however, it is our belief that attaining such a device will be instrumental to the future of biological microscopy as it relates to MR.

In addition to having such a small field of view, one of the biggest drawbacks of the current microcoil design is that it generates an inhomogeneous field of view. This property is inherent to all surface coils and does not pose a serious problem for structural studies such as those performed during our single cell and tractography experiments. Unfortunately, this factor can pose a serious problem to quantitative studies if it is not possible to ensure that measurements are taken from the exact same spot relative to the coil face. This factor can introduce a great deal of variability between separate experiments in the same study and could possibly have contributed to the signal variation seen in our live-slice experiments. Although initial tests of our tissue retention system showed the slice to be in contact with the coil face, this was not confirmed in each subsequent experiment. A pilot scan with slice orientation positioned through the coil face could confirm that the tissue is lying flush against the surface coil and thus will be included as a control in future quantitative work in which the microcoils are employed.

Alternatively, this issue could be solved using engineering principles if there were a way to attain a more homogeneous field over a larger area. This could be accomplished by using a more traditional saddle coil to excite the sample and relegating the microsurface coil to a receive-only function. Although this would allow for more homogeneous excitation, the receive function would still result in inhomogeneity. Arranging two microcoils into a Helmholtz pair configuration—although more difficult to implement—would allow for more homogeneous excitation and reception than what is currently attainable with a single surface coil. Ideally, these concepts could be combined into a phased array design consisting of multiple Helmholtz pairs which would allow for the uniform excitation of large sections of tissue slices. While design and fabrication of such a system would require far greater engineering expertise than those possessed by the author, such a device would be useful for a myriad of scientific and clinical pursuits: not the least important being the potential implications for the field of tissue engineering.

Visualization of Perikerya, Axon Bundles, and Neural Activity Using Diffusion-Weighted MRM: Implications for Tissue Engineering

Future success in generating functional parenchyma for use in tissue replacement therapies will depend upon reliable, non-destructive methods of structural validation. One of the most important—and ignored—considerations in the field of tissue replacement is the tenet that function and structure are inextricably linked. As such, studies which attempt to replicate certain properties of damaged tissue components—i.e. cell type—in replacement grafts without regard to the microstructural organization of the tissue in question have met with limited success (Gorio et al., 2004; Wu et al., 2003). The negative findings of these studies and many others like them suggest that without replication of a damaged tissue's basic structural elements, there is little hope of restoring functional deficits incurred as a result of that tissue's malfunction or loss. If tissue replacement therapies are ever to be applied to the most complex functional tissues, such

as those in found in the central nervous system, the analysis methods used for assessing their structure must be capable of obtaining resolutions sufficient to track interconnectivity at the cellular level.

Of all tissue replacement therapies to date, by far the most successful examples come from studies employing tissue grafts that are thin or that involve tissue with inherently low vascularization (Moon and West, 2008). This observation highlights one of the largest unsolved problems in the field of tissue engineering: the difficulty of vascularizing tissue constructs. Without the ability to offer sufficient nutrient delivery and waste removal—both key functions of the circulatory system—tissues with high metabolic demand may only function in constructs thin enough to allow for diffusion processes to act in lieu of vascular perfusion. Thin, laminar sheets of cardiac parenchyma—a highly demanding tissue type in terms of its metabolic requirements—are reported to have been employed successfully in the literature (Shimizu et al., 2006). In this example, the authors have implanted multiple sheets of cultured cardiomyocytes into living rats three layers at a time (3 tissue sheets = 80 μ m thickness) over ten separate surgical procedures to construct a tissue graft totaling roughly 1mm in thickness. The implementation of this method is dependent on the time interval between multiple surgical procedures allowing for the infiltration of vasculature from the host animal into each newly implanted tissue graft. Other studies have employed explanted vascular beds as living scaffolds for the seeding and introduction of various stem cell populations into host animals (Chang et al., 2009). Using this method, portions of the seeded stem cell populations remained viable in a three dimensional, biological tissue construct and allowed for successful implantation. However, it should be noted that cell viability in this study was heavily time dependent with perfused constructs remaining in the *ex vivo* environment for 24h losing up to half of their seeded cell populations. While these studies represent

remarkable achievements in the field of tissue engineering, they also serve as examples of how much more progress needs to be made if we are to ever develop complex, functional, three-dimensional constructs that can be used clinically for tissue replacement. Some of the most promising tissue engineering applications involve the layering of many thin, cultured tissue segments in order to obtain three dimensional constructs (Borenstein et al., 2007). The techniques described in this work include microfabrication of the individual tissue sheets so as to control for the organization of multiple cell types into a functioning organ system. The authors also discuss the interspersion of synthetic capillary networks between layers of parenchyma effectively offering a solution to the problem of vascularizing large tissue constructs. The fact that these highly engineered synthetic organ constructs are formed from thin tissue sheets has enormous implications for the future of MRM. Currently, the preferred methods of imaging viable cells include laser scanning microscopy (LSM) protocols employed in either two-photon LSM or one-photon confocal LSM. The sample penetration depth offered by two-photon LSM and confocal LSM enables visualization of the complex, three-dimensional structures inherent to biological tissues. While both imaging methods offer superb image resolution—250nm using fluorescent techniques—as well as fast acquisition times—multiple images per second—neither can claim to be non-invasive (Cox and Sheppard, 2004). Because both employ high-powered laser excitation as a means of tissue visualization, the protocols have been shown to elicit various phototoxic effects resulting from the generation of oxygen free radicals and changes in calcium homeostasis. These alterations in cell physiology lead to numerous undesirable conditions including nuclear fragmentation, DNA strand breaks, plasma membrane compromise, and apoptotic cell death (Knight et al., 2003; Tilapur et al., 2001). The use of fluorescent dyes—a common practice in LSM protocols—exacerbates this problem as they often create oxygen free

radicals upon degradation. (Hüser et al., 1998; Zorov et al., 2000). These phototoxic effects are so prevalent and dramatic that they have been employed in a treatment known as photodynamic therapy as a means of killing tumor cells (Diamond et al., 1972). When LSM is employed as a means of validating the microstructure of engineered tissues used in replacement therapies, these detrimental side-effects could potentially lead to compromised samples and ultimately result in graft rejection. While progress is being made to reduce the cellular stress effects caused by LSM, no visualization method for viable tissue currently exists that is both non-invasive and able to resolve tissue microstructure at the cellular level; however, MRM will likely be a candidate for this purpose in the near future. Given that MR is a non-invasive technique and that we have demonstrated its ability to visualize both individual cell bodies and axon bundles, it is not so difficult to imagine some iteration of the described MRM methods being used to determine the microstructural organization of thin tissue layers. Furthermore, if future studies are able to confirm the utility of using diffusion-weighted imaging as a means of detecting neural firing, these same methods could serve as a means of confirming neural network connectivity at the cellular level. This, in turn, could aid in the fabrication of custom tissue grafts devoid of phototoxic stress effects and designed to mimic the microstructural aspects of the tissues they are intended to replace. While this alone would not ensure the success of tissue replacement therapies, it would represent a significant advance in the field of tissue engineering and bring us closer to a day where autologous tissue grafts would be widely available for patients suffering from tissue damage and organ failure.

Diffusion-Weighted fMRI

In the study employing diffusion-weighted imaging as a means of visualizing changes in the diffusion properties of tissue associated with neural activation, we demonstrated the ability to observe said changes in the absence of a functioning vascular network. The implications of this

research were important in that the primary criticism of previous works purporting to observe these changes were that they were due to the confounding effects of blood flow. However, it is important to remember that the neural activation patterns in our experiments were different and thus could not directly confirm or refute the previous findings. Ideally, we would like to perform similar, avascularized, live-slice tissue experiments with the ability to mimic neural activation patterns observed during *in vivo* experiments. As discussed previously, we opted for chemical induction of neural activation in our experiments due to the difficulties of conducting electrophysiological equipments in conjunction with MRI. Another technique has recently been suggested which may serve as a means of eliciting the desired activity in future live-slice experiments. The method is known as photostimulation and can currently be achieved through multiple methodologies (Callaway and Katz, 1993; Fortin et al., 2008). The common theme to photostimulation methods revolves around modifications to cell-signaling machinery by creating an intermediate step in which light of a particular wavelength is required to initiate ligand binding or channel activation. These modifications are brought about by changing a ligand's chemical or steric properties in a light-dependent reaction. Electrophysiological data have confirmed the ability to control nerve firing using photostimulation even demonstrating that the rate of action potential generation in a sample can be manipulated by changing the wavelength of incident light. We believe this method could be used to control the firing rate of a small population of neurons in a live-slice MRM experiment. Employing a fiber optic cable to deliver light of a specified wavelength to a tissue slice pre-treated with a photoswitchable label might allow us to replicate firing patterns observed during normal physiological nerve activation without the need for electrophysiological equipment. In addition to the methods described here, we would presumably need to employ a diffusion-weighted, echo planar imaging protocol in

order to acquire MR images quickly enough to observe diffusion signal changes due to neuronal firing. Such MRI scan protocols have been described previously in the literature (Shen et al., 2008). It is our intention to conduct a future study using a combination of the described methodology—i.e. both photostimulation and devascularized, live brain tissue slices—which, depending on the results, would offer stronger evidence for or against the possibility of using diffusion-weighted fMRI in functional studies.

APPENDIX
 SPHERICAL COORDINATES FOR DIFFUSION GRADIENT DIRECTIONS USED IN
 DIFFUSION TENSOR IMAGING EXPERIMENTS

21-Directions (rank-4)	
Theta	Phi
0.0000	90.0000
63.4350	0.0000
63.4350	72.0000
63.4350	144.0000
63.4350	216.0000
63.4350	288.0000
31.7175	0.0000
31.7175	72.0000
31.7175	144.0000
31.7175	216.0000
31.7175	288.0000
58.2826	36.0000
58.2826	108.0000
58.2826	180.0000
58.2826	252.0000
58.2826	324.0000
90.0000	18.0000
90.0000	54.0000
90.0000	90.0000
90.0000	306.0000
90.0000	342.0000

LIST OF REFERENCES

- Acker, J.P., McGann, L.E., 2000. Cell-cell contact affects membrane integrity after intracellular freezing. *Cryobiology*. 40, 54-63.
- Aguayo, J.B., Blackband, S.J., Schoeniger, J., Mattingly, M.A., Hintermann, M., 1986. Nuclear magnetic resonance imaging of a single cell. *Nature*. 322, 190-191.
- Ahn, C.B., Cho, Z.H., 1991. Diffusion and perfusion in high resolution NMR imaging and microscopy. *Mag. Reson. Med.* 19, 228-232.
- Alberts, B., 2002. *Molecular Biology of the Cell*. Garland Science, New York.
- Anderson, A.W., Pizzonia, J.X., Bronen, R.A., Spencer, D.D., Gore, J.C., 2000. Effects of cell volume fraction changes on apparent diffusion in human cells. *Magn. Reson. Imaging*. 18, 689-695.
- Andreasen, A., Danscher, G., Juhl, S., Stoltenberg, M., Revsbech, N.P., Jensen, H., Jensen, K.B., 1997. Distinct differences in partial oxygen pressure at micrometer ranges in the rat hippocampal region. *J. Neurosci. Methods*. 72(1), 15-21.
- Andrew, R.D., Adams, J.R., Polischuk, M., 1996. Imaging NMDA- and kainate-induced intrinsic optical signals from the hippocampal slice. *J. Neurophys.* 76(4), 2707-2717.
- Armon, C., 2008. From clues to mechanisms: understanding ALS initiation and spread. *Neurology*. 71, 872-873.
- Arvidsson, A., Collin, T., Kirik, D., Kokaia, Z., Lindvall, O., 2002. Neuronal replacement from endogenous precursors in the adult brain after stroke. *Nature Med.* 8(9), 963-970.
- Atalay, M.K., Forder, J.R., Chacko, V.P., Kawamoto, S., Zerhouni, E.A., 1993. Oxygenation in the rabbit myocardium: assessment with susceptibility-dependent imaging. *Radiology*. 189(3), 759-764.
- Badak, M.I., Ozkisacik, E.A., Boga, M., Guncun, U., Discigil, B., 2004. Replacement of a Björk-Shiley delrin aortic valve still functioning after 25 years. *Tex. Heart Inst. J.* 31(3), 303-305.
- Barr, C.S., Dokas, L.A., 1998. Glucocorticoids regulate protein synthesis in hippocampal slices under mild heat shock conditions. *Endocrine* 8(2), 135-141.
- Barrick, T.R., Lawes, I.N.C., Clark, C.A., 2009. White matter tract visualization using properties of termination coordinate eigenmaps. *Magn. Reson. Med.* 61, 1261-1267.
- Basser, P.J., 1995. Inferring microstructural features and the physiological state of tissues from diffusion-weighted images. *NMR Biomed.* 8(7-8), 333-344.
- Bassar, P.J., Mattiello, J., LeBihan, D., 1994. MR diffusion tensor spectroscopy and imaging. *Biophys. J.* 66, 259-267.

- Bellomo, G., Perotti, M., Taddei, F., Mirabelli, F., Finardi, G., Nicotera, P., Orrenius, S., 1992. Tumor necrosis factor α induces apoptosis in mammary adenocarcinoma cells by an increase in intranuclear free Ca^{2+} concentration and DNA fragmentation. *Cancer Res.* 52, 1342-1346.
- Benkovic, S.A., Connor, J.R., 1993. Ferritin, transferrin, and iron in selected regions of the adult and aged rat brain. *J. Comp. Neurol.* 338(1), 97-113.
- Benveniste, H., Hedlund, L.W., Johnson, G.A., 1992. Mechanism of detection of acute cerebral ischemia in rats by diffusion-weighted magnetic resonance microscopy. *Stroke.* 23(5), 746-754.
- Blackband, S.J., Bui, J.D., Buckley, D.L., Zelles, T., Plant, H.D., Inglis, B.A., Phillips, M.I., 1997. MR Microscopy of Perfused Brain Slices. *Magn. Reson. Med.* 38, 1012-1015.
- Borenstein, J.T., Weinberg, E.J., Orrick, B.K., Sundback, C., Kaazempur-Mofrad, M.R., Vacanti, J.P., 2007. Microfabrication of three-dimensional engineered scaffolds. *Tissue Eng.* 13(8), 1837-1844.
- Buckley, D.L., Bui, J.D., Phillips, M.I., Zelles, T., Inglis, B.A., Plant, H.D., Blackband, S.J., 1999. The effect of ouabain on water diffusion in the rat hippocampal slice measured by high resolution NMR imaging. *Mag. Reson. Med.* 41, 137-142.
- Bui, J.D., Buckley, D.L., Phillips, M.I., Blackband, S.J., 1999. Nuclear magnetic resonance imaging measurements of water diffusion in the perfused hippocampal slice during N-methyl-D-aspartate-induced excitotoxicity. *Neurosci.* 93(2), 487-490.
- Callaghan, P.T., 1991. *Principles of Nuclear Magnetic Resonance Microscopy*. Oxford, New York.
- Callaghan, P.T., Eccles, C.D., 1988. Diffusion-limited resolution in nuclear magnetic resonance microscopy. *J. Mag. Reson.* 78, 1-8.
- Callaway, E.M., Katz, L.C., 1993. Photostimulation using caged glutamate reveals functional circuitry in living brain slices. *Proc. Natl. Acad. Sci. USA.* 90, 7661-7665.
- Carthew, P., Dorman, B.M., Edwards, R.E., Francis, J.E., Smith, A.G., 1993. A unique rodent model for both the cardiotoxic and hepatotoxic effects of prolonged iron overload. *Lab. Invest.* 69(2), 217-222.
- Chang, E.I., Bonillas, R.G., El-ftesi, S., Chang, E.I., Ceradini, D.J., Vial, I.N., Chan, D.A., Michaels V, J., Gurtner, G.C., 2009. Tissue engineering using autologous microcirculatory beds as vascularized bioscaffolds. *FASEB J.* 23, 906-915.
- Cho, Z.H., Ahn, C.B., Juh, S.C., Lee, H.K., Jacobs, R.E., Lee, S., Yi, J.H., Jo, J.M., 1988. Nuclear magnetic resonance microscopy with 4-microns resolution: theoretical study and experimental results. *Med. Phys.* 15(6), 815-824.

- Cho, Z.H., Ahn, C.B., Juh, S.C., Jo, J.M., Friedenber, R.M., Fraser, S.E., Jacobs, R.E., 1990. Recent progress in NMR microscopy towards cellular imaging. *Phil. Trans. R. Soc. Lond. A.* 333, 469-475.
- Choi, Y., McClain, M.A., Laplaca, M.C., Fraiser, A.B., Allen, M.G., 2007. Three dimensional MEMS microfluidic perfusion system for thick brain slice cultures. *Biomed. Microdevices.* 9(1), 7-13.
- Ciobanu, L., Webb, A.G., Pennington, C.H., 2003. Magnetic resonance imaging of biological cells. *Prog. Nucl. Magn. Reson. Spect.* 42, 69-93.
- Cohen, L.B., Hille, B., Keynes, R.D., 1996. Light scattering and birefringence changes during activity in the electric organ of *Electrophorus electricus*. *J. Physiol.* 203, 489-509.
- Collingridge, G.L., 1995. The brain slice preparation: a tribute to the pioneer Henry McIlwain. *J. Neurosci. Meth.* 59, 5-9.
- Contractor, A., Swanson, G.T., Sailer, A., O'Gorman, S., Heinemann, S.F., 2000. Identification of the kainate receptor subunits underlying modulation of excitatory synaptic transmission in the CA3 region of the hippocampus. *J. Neurosci.* 20(22), 8269-8278.
- Cox, G., Sheppard, C.J.R., 2004. Practical limits of resolution in confocal and non-linear microscopy. *Microsc. Res. Tech.* 63,18-22.
- Crossgrove, J., Zheng, W., 2004. Manganese toxicity upon overexposure. *NMR Biomed.* 17, 544-553.
- Darquie, A., Poline, J.B., Poupon, C., Saint-Jalmes, H., Le Bihan, D., 2001. Transient decrease in water diffusion observed in human occipital cortex during visual stimulation. *Proc. Natl. Acad. Sci. USA.* 98(16), 9391-9395.
- Davenport, H.W., 1974. *The ABC of Acid-Base Chemistry: The Elements of Physiological Blood-gas Chemistry for Medical Students and Physicians*, 6th ed. University of Chicago Press, Chicago.
- Davies, R.E., 1963. A Molecular Theory of Muscle Contraction: calcium-dependent contractions with hydrogen bond formation plus ATP-dependent extensions of part of the myosin-actin cross-bridges. *Nature.* 199, 1068-1074.
- Diamond, I., Granelli, S.G., McDonagh, A.F., Nielsen, S., Wilson, C.B., Jaenicke, R. 1972. Photodynamic therapy of malignant tumors. *Lancet.* 2(7788), 1175-1177.
- Dobson, A.W., Erikson, K.M., Aschner, M., 2004. Manganese neurotoxicity. *Ann. NY Acad. Sci.* 1012, 115-128.
- Domenighetti, G., 2007. Prognosis, screening, early detection and differentiation of arterial pulmonary hypertension. *Swiss Med. Wkly.* 137, 331-336.

- Drew, S.C., Silva, P., Crozier, S., Pearcey, M.J., 2004. A diffusion and T₂ relaxation MRI study of the ovine lumbar intervertebral disk under compression in vitro. *Phys. Med. Biol.* 49(16), 3585-3592.
- Duncan, J.S., Bartlett, P., Barker, G.J., 1996. Technique for measuring hippocampal T₂ relaxation time. *Am. J. Neuroradiol.* 17, 1805-1810.
- Ernstberger, T., Heidrich, G., Buchhorn, G., 2007. Postimplantation MRI with cylindric and cubic intervertebral test implants: evaluation of implant shape, material, and volume in MRI artifacting—an in vitro study. *Spine J.* 7(3), 353-359.
- Espanol, M.T., Litt, L., Chang, L.H., James, T.L., Weinstein, P.R., Chan, P.H., 1996. Adult rat brain-slice preparation for nuclear magnetic resonance spectroscopy studies of hypoxia. *Anesthesiology.* 84(1), 201-210.
- Focht, S.J., Snyder, B.S., Beard, J.L., Van Gelder, W., Williams, L.R., Connor, J.R., 1997. Regional distribution of iron, transferrin, ferritin and oxidatively-modified proteins in young and aged Fischer 344 rat brains. *Neurosci.* 79(1), 255-261.
- Fortin, D.L., Banghart, M.R., Dunn, T.W., Borges, K., Wagenaar, D.A., Gaudry, Q., Karakossian, M.H., Otis, T.S., Kristan, W.B., Trauner, D., Kramer, R.H., 2008. Photochemical control of endogenous ion channels and cellular excitability. *Nat. Methods.* 5(4), 331-338.
- Foster-Gareau, P., Heyn, C., Alejski, A., Rutt, B.K., 2003. Imaging single mammalian cells with a 1.5 T clinical MRI scanner. *Magn. Reson. Med.* 49, 968-971.
- Foy, C.M.L., Nicholas, H., Hollingworth, P., Boothby, H., Williams, J., Brown, R.G., Al-Sarraj, S., Lovestone, S., 2007. Diagnosing Alzheimer's disease—non-clinicians and computerized algorithms together are as accurate as the best clinical practice. *Int. J. Geriatr. Psychiatry.* 22, 1154-1163.
- Gill, R., Sibson, N.R., Maskell, L., Carpenter, T.A., Hall, L.D., Pickard, J.D., 1996. The protective effect of MK-801 on infarct development over a period of 24 h as assessed by diffusion-weighted magnetic resonance imaging. *NMR Biomed.* 9(6), 241-248.
- Gonzalez, L.E., Juknat, A.A., Venosa, A.J., Verrengia, N., Kotler, M.L., 2008. Manganese activates the mitochondrial apoptotic pathway in rat astrocytes by modulating the expression of proteins of the Bcl-2 family. *Neurochem. Int.* 53(6-8), 408-415.
- Gorio, A., Torrente, Y., Madaschi, L., Di Stefano, A.B., Pisati, F., Marchesi, C., Belicchi, M., Di Gilulio, A.M., Bresolin, N., 2004. Fate of autologous dermal stem cells transplanted into the spinal cord after traumatic injury (TSCI). *Neurosci.* 125, 179-189.
- Gouras, G.K., 2001. Current theories for the molecular and cellular pathogenesis of Alzheimer's disease. *Exp. Rev. Mol. Med.* 31 <http://www-ermm.cbcu.cam.ac.uk/01003167h.htm> last accessed 8/25/08.

- Greenlee, R.T., Hill-Harmon, M.B., Murray, T., Thun, M., 2001. Cancer Statistics, 2001. *CA Cancer J. Clin.* 51, 15-36.
- Haacke, E.M., 1999. *Magnetic Resonance Imaging: Physical Principles and Sequence Design.* Wiley-Liss, New York.
- Heyn, C., Ronald, J.A., Mackenzie, L.T., MacDonald, I.C., Chambers, A.F., Rutt, B.K., Foster, P.J., 2006. In vivo magnetic resonance imaging of single cells in mouse brain with optical validation. *Magn. Reson. Med.* 55, 23-29.
- Hsu, E.W., Aiken, N.W., Blackband, S.J., 1996. Nuclear magnetic resonance microscopy of single neurons under hypotonic perturbation. *Am. J. Physiol. Cell Physiol.* 271(6), C1895-C1900.
- Hüser, J., Rechenmacher, C.E., Blatter, L.A., 1998. Imaging the permeability pore transition in single mitochondria. *Biophys. J.* 74, 2129-2137.
- Hufnagel, A., Weber, J., Marks, S., Ludwig, T., De Greiff, A., Leonhardt, G., Widmann, G., Stolke, D., Forsting, M., 2003. Brain diffusion after single seizures. *Epilepsia.* 44(1), 54-63.
- Iwasa, K., Tasaki, I., Gibbons, R.C., 1980. Swelling of nerve fibers associated with action potentials. *Science.* 210, 338-339.
- Jackson, L.S., Nelson, J.A., Case, T.A., Burnham, B.F., 1985. Manganese protoporphyrin IX. A potential intravenous paramagnetic NMR contrast agent: preliminary communication. *Invest. Radiol.* 20(2), 226-229.
- Jarvis, C.R., Anderson, T.R., Andrew, R.D., 2001. Anoxic depolarization mediates acute damage independent of glutamate in neocortical brain slices. *Cereb. Cortex.* 11, 249-259.
- Johnson, G.A., Cates, G., Chen, X.J., Cofer, G.P., Driehuys, B., Happer, W., Hedlund, L.W., Saam, B., Shattuck, M.D., Swartz, J., 1997. Dynamics of magnetization in hyperpolarized gas MRI of the lung. *Magn. Reson. Med.* 38, 66-71.
- Jones, D.K., Simmons, A., Williams, S.C.R., Horsfield, M.A., 1999. Non-invasive assessment of axonal fiber connectivity in the human brain via diffusion tensor MRI. *Magn. Reson. Med.* 42, 37-41.
- Kallenberg, K., Shultz-Schaeffer, W.J., Jastrow, U., Poser, S., Meissner, B., Tschampa, H.J., Zerr, I., Knauth, M., 2006. Creutzfeldt-Jakob disease: comparative analysis of MR imaging sequences. *Am. J. Neuroradiol.* 27, 1459-1462.
- Kania, R.E., Herman, P., Ar, A., Tran Ba Huy, P., 2005. Technical pitfalls in middle ear gas studies: errors introduced by the gas permeability of tubing and additional dead space. *Acta Otolaryngol.* 125(5), 529-533.

- Kiefer, C., Slotboom, J., Buri, C., Gralla, J., Remonda, L., Dierks, T., Strik, W.K., Schroth, G., Klaus, P., 2004. Differentiating hippocampal subregions by means of quantitative magnetization transfer and relaxometry: preliminary results. *NeuroImage*. 23, 1093-1099.
- Khong, Y.M., Zhang, J., Zhou, S., Cheung, C., Doberstein, K., Samper, V., Yu, H., 2007. Novel intra-tissue perfusion system for culturing thick liver tissue. *Tissue Eng*. 13(9), 2345-2346.
- Kim, G.H., Kosterin, P., Obaid, A.L., Salzberg, B.M., 2007. A mechanical spike accompanies the action potential in mammalian nerve terminals. *Biophys. J.* 92(9), 3122-3129.
- Knight, M.M., Roberts, S.R., Lee, D.A., Bader, D.L., 2003. Live cell imaging using confocal microscopy induces intracellular calcium transients and cell death. *Am. J. Physiol. Cell Physiol.* 284, C1083-C1089.
- Koenig, S.H., Brown, R.D., 1985. Magnetic field dependence of proton relaxation rates in tissue with added Mn^{2+} : rabbit liver and kidney. *Mag. Reson. Med.* 2, 159-168.
- Krebs, H.A., 1981. *Otto Warburg: Cell Physiologist, Biochemist and Eccentric*. Clarendon Press, Oxford.
- Kuo, Y-T., Herlihy, A.H., So, P-W., Bhakoo, K.K., Bell, J.D., 2005. In vivo measurements of T_1 relaxation times in mouse brain associated with different modes of systemic administration of manganese chloride. *J. Magn. Reson. Imaging*. 21, 334-339.
- Lauer, U.A., Graf, H., Berger, A., Claussen, C.D., Schick, F., 2005. Radio frequency versus susceptibility effects of small conductive implants—a systematic MRI study on aneurysm clips at 1.5 and 3 T. *Magn. Reson. Imaging*. 23(4), 563-569.
- Le Bihan, D., Urayama, S-i., Aso, T., Hanakawa, T., Fukuyama, H., 2006. Direct and fast detection of neuronal activation in the human brain with diffusion MRI. *Proc. Natl. Acad. Sci. USA*. 103(21), 8263-8268.
- Leddy, H.A., Guilak, F., 2008. Site-Specific effects of compression on macromolecular diffusion in articular cartilage. *Biophys. J.* 95(10), 4890-4895.
- Li, C-L., McIlwain, H., 1957. Maintenance of resting membrane potentials in slices of mammalian cerebral cortex and other tissues *in vitro*. *J. Physiol.* 139, 178-190.
- Li, J.G., Stanisz, G.J., Henkelman, R.M., 1998. Integrated analysis of diffusion and relaxation of water in blood. *Magn. Reson. Med.* 40, 79-88.
- Lim, K.O., Stark, D.D., Leese, P.T., Pfefferbaum, A., Rocklage, S.M., Quay, S.C., 1991. Hepatobiliary MR imaging: first human experience with $MnDPDP^1$. *Radiology*. 178, 79-82.
- Lin, C-P., Tseng, W-Y.I., Cheng, H-C., Chen, J-H., 2001. Validation of diffusion tensor magnetic resonance axonal fiber imaging with registered manganese-enhanced optic tracts. *NeuroImage*. 14, 1035-1047.

- Lin, Y.J., Koretsky, A.P., 1997. Manganese ion enhances T₁-weighted MRI during brain activation: an approach to direct imaging of brain function. *Magn. Reson. Med.* 38(3), 378-88.
- Logothetis, N.K., 2008. What we can do and what we cannot do with fMRI. *Nature.* 453(12), 869-878.
- Marquardt, D.W., 1963. An algorithm for least-squares estimation of nonlinear parameters. *J. Soc. Ind. Appl. Math.* 11, 431-441.
- Martens, U., Capito, B., Wree, A., 1998. Septotemporal distribution of (³H)MK-801, (³H)AMPA and (³H)Kainate binding sites in the rat hippocampus. *Anat. Embryol.* 198, 195-204.
- Matsuura, H., Inoue, T., Konno, H., Sasaki, M., Ogasawara, K., Ogawa, A., 2002. Quantification of susceptibility artifacts produced on high-field magnetic resonance images by various biomaterials used for neurosurgical implants. Technical note. *J. Neurosurg.* 97(6), 1472-1475.
- Matsuura, H., Inoue, T., Ogasawara, K., Sasaki, M., Konno, H., Kuzu, Y., Nishimoto, H., Ogawa, A., 2005. Quantitative analysis of magnetic resonance imaging susceptibility artifacts caused by neurosurgical biomaterials: comparison of 0.5, 1.5, and 3.0 Tesla magnetic fields. *Neurol. Med. Chir.* 45, 395-399.
- Mattson, M.P., Chan, S.L., 2003. Calcium orchestrates apoptosis. *Nature Cell. Biol.* 5(12), 1041-1043.
- McAllister, D.V., Wang, P.M., Davis, S.P., Park, J-H., Canatella, P.J., Allen, M.G., Prausnitz, M.R., 2003. Microfabricated needles for transdermal delivery of macromolecules and nanoparticles: fabrication methods and transport studies. *Proc. Natl. Acad. Sci. USA.* 100(24), 13755-13760.
- Miller, K.L., Bulte, D.P., Devlin, H., Robson, M.D., Wise, R.G., Woolrich, M.W., Jezzard, P., Behrens, E.J., 2007. Evidence for a vascular contribution to diffusion fMRI at high b value. *Proc. Natl. Acad. Sci. USA.* 104(52), 20967-20972.
- Milton, W.J., Atlas, S.W., Lexa, F.J., Mozley, P.D., Gur, R.E., 1991. Deep gray matter hypointensity patterns with aging in healthy adults: MR imaging at 1.5T. *Radiology.* 181, 715-719.
- Minematsu, K., Li, L., Fisher, M., Sotak, C.H., Davis, M.A., Fiandaca, M.S., 1992. Diffusion-weighted magnetic resonance imaging: rapid and quantitative detection of focal brain ischemia. *Neurology.* 42(1), 235-240.
- Monasterio, N., Ramos, E., Morales, T., 2008. Changes in c-fos and NOS expression in the PVH of lactating rats in response to excitotoxicity and stress. *Ann. NY Acad. Sci.* 1148, 161-164.

- Moon, J.J., West, J.L., 2008. Vascularization of engineered tissues: approaches to promote angiogenesis in biomaterials. *Curr. Top. Med. Chem.* 8, 300-310.
- Mori, S., Crain, B.J., Chacko, V.P., Zijl, P.C.M.v., 1999. Three-dimensional tracking of axonal projections in the brain by magnetic resonance imaging. *Ann. Neurol.* 45, 265-269.
- Mori, S., Zhang, J., 2006. Principles of diffusion tensor imaging and its applications to basic neuroscience research. *Neuron.* 51, 527-539.
- Moseley, M.E., Cohen, Y., Kucharczyk, J., Mintorovitch, J., Asgari, H.S., Wendland, M.F., Tsuruda, J., Norman, D., 1990a. Diffusion-weighted MR imaging of anisotropic water diffusion in cat central nervous system. *Radiology.* 176, 439-445.
- Moseley, M.E., Kucharczyk, J., Mintorovitch, J., Cohen, Y., Kurhanewicz, J., Derugin, N., Asgari, H., Norman, D., 1990b. Diffusion-weighted MR imaging of acute stroke: correlation with T₂-weighted and magnetic susceptibility-enhanced MR imaging in cats. *AJNR.* 11, 423-429.
- Narita, K., Kawasaki, F., Kita, H., 1990. Mn and Mg influxes through Ca channels of motor nerve terminals are prevented by verapamil in frogs. *Brain Res.* 510, 289-295.
- Nasu, T., 1995. Actions of manganese ions in contraction of smooth muscle. *Gen. Pharmacol.* 26(5), 945-953.
- Nasu, T., Baba, K., 1997. Mechanics of manganese ions-induced contraction of ileal longitudinal muscle in Ca(2+)-free, high-K⁺ medium. *Gen. Pharmacol.* 28(4), 503-507.
- Netoff, T.I., Clewley, R., Arno, S., Keck, T., White, J.A., 2004. Epilepsy in small-world networks. *J. Neurosci.* 24(37), 8075-8083.
- Nicholson, C., Syková, E., 1998. Extracellular space structure revealed by diffusion analysis. *Trends Neurosci.* 21, 207-215.
- Niendorf, T., Dijkhuizen, R.M., Norris, D.G., van Lookeren Campagne, M., Nicolay, K., 1996. Biexponential diffusion attenuation in various states of brain tissue: implications for diffusion-weighted imaging. *Mag. Reson. Med.* 36(6), 847-857.
- Normann, P.T., Hals, P.A., 1995. In vivo stability and excretion of gadodiamide (GdDTPA-BMA), a hydrophilic gadolinium complex used as a contrast enhancing agent for magnetic resonance imaging. *Eur. J. Drug Metab. Pharmacokinet.* 20(4), 307-313.
- Odelblad, E., 1966. Micro-NMR in high permanent magnetic fields. *Acta. Obstet. Gynecol. Scand.* 45(2), 1-188.
- Oertzen, J.v., Urbach, H., Blümcke, I., Reuber, M., Träber, F., Peveling, T., Menzel, C., Elger, C.E., 2002. Time-efficient T₂ relaxometry of the entire hippocampus is feasible in temporal lobe epilepsy. *Neurology.* 58, 257-264.

- Olson, D.L., Peck, T.L., Webb, A.G., Magin, R.L., Sweedler, J.V., 1995. High-resolution microcoil $^1\text{H-NMR}$ for mass-limited, nanoliter-volume samples. *Science*. 270(5244), 1967-1970.
- Pakhotin, P.I., Belousov, A.B., Otmakhov, N.A., 1990. Functional stability of the brain slices of ground squirrels, *Citellus undulates*, kept in conditions of prolonged deep periodic hypothermia: electrophysiological criteria. *Neurosci*. 38(3), 591-598.
- Parker, G.J.M., 2004. Analysis of MR diffusion weighted images. *Brit. J. Radiol.*, Special Issue. 77, S176-S185.
- Phuttharak, W., Hesselink, J.R., Wixom, C., 2005. MR features of cerebral aspergillosis in an immunocompetent patient: Correlation with histology and elemental analysis. *Am. J. Neuroradiol*. 26, 835-838.
- Puchtler, H., Meloan, S.N., 1985. On the chemistry of formaldehyde fixation and its effects on immunohistochemical reactions. *Histochem*. 82, 201-204.
- Quadery, F.A., Okamoto, K., 2003. Diffusion-weighted MRI of haemangioblastomas and other cerebellar tumors. *Neuroradiol*. 45, 212-219.
- Redondo, C., López-Toledano, M.A., Lobo, M.V.T., Gonzalo-Gobernado, R., Reimers, D., Herranz, A.S., Paíno, C.L., Bazán, E., 2007. Kainic acid triggers oligodendrocyte precursor cell proliferation and neuronal differentiation from striatal neural stem cells. *J. Neurosci. Res*. 85, 1170-1182.
- Reeder, S.B., Holmes, A.A., McVeigh, E.R., Forder, J.R., 1999. Simultaneous noninvasive determination of regional myocardial perfusion and oxygen content in rabbits: toward direct measurement of myocardial oxygen consumption at MR imaging. *Radiology*. 212(3), 739-747.
- Roskams, A.J.I., Connor, J.R., 1994. Iron, transferrin, and ferritin in the rat brain during development and aging. *J. Neurochem*. 63(2), 709-716.
- Rumboldt, Z., Camacho, D.L.A., Lake, D., Welsh, C.T., Castillo, M., 2006. Apparent diffusion coefficients for differentiation of cerebellar tumors in children. *Am. J. Neuroradiol*. 27, 1362-1369.
- Satin, A., Rall, T.W., 1970. The effect of adenosine and adenine nucleotides on the cyclic adenosine 3':5'-monophosphate content of guinea pig cerebral cortex slices. *Mol. Pharmacol*. 6, 13-23.
- Schalekamp, M., Harrison, P.R., Paul, J., 1975. Iron incorporation and haemoglobin synthesis in erythropoietic cells during the ontogenesis of the mouse. *J. Embryol. Exp. Morph*. 34(2), 355-371.

- Schmitt, M., Potthast, A., Sosnovik, D.E., Polimeni, J.R., Wiggins, G.C., Triantafyllou, C., Wald, L.L., 2008. A 128-channel receive-only cardiac coil for highly accelerated cardiac MRI at 3 Tesla. *Magn. Reson. Med.* 59(6), 1431-1439.
- Schoeniger, J.S., Aiken, N., Hsu, E., Blackband, S.J., 1994. Relaxation-time and diffusion NMR microscopy of single neurons. *J. Magn. Reson. Ser. B.* 103, 261-273.
- Schwob, J.E., Fuller, T., Price, J.L., Olney, J.W., 1980. Widespread patterns of neuronal damage following systemic or intracerebral injections of kainic acid: a histological study. *Neurosci.* 5, 991-1014.
- Sekino, M., Sano, M., Ogiue-Ikeda, M., Ueno, S., 2006. Estimation of membrane permeability and intracellular diffusion coefficients. *Magn. Reson. Med. Sci.* 5(1), 1-6.
- Serbus, L.R., Cha, B.-J., Theurkauf, W.E., Saxton, W.M., 2005. Dynein and the actin cytoskeleton control kinesin-driven cytoplasmic streaming in *Drosophila* oocytes. *Development.* 132, 3743-3752.
- Shapiro, E.M., Skrtic, S., Sharer, K., Hill, J.M., Dunbar, C.E., Koretsky, A.P., 2004. MRI detection of single particles for cellular imaging. *Proc. Natl. Acad. Sci.* 101(30), 10901-10906.
- Shapiro, E.M., Sharer, K., Skrtic, S., Koretsky, A.P., 2006. In vivo detection of single cells by MRI. *Magn. Reson. Med.* 55, 242-249.
- Shen, S-H, Chiou, Y-Y., Wang, J-H., Yen, M-S., Lee, R-C., Lai, C-R., Chang, C-Y., 2008. Diffusion-weighted single-shot echo-planar imaging with parallel technique in assessment of endometrial cancer. *Am. J. Roentgenol.*
- Shepherd, T.M., Blackband, S.J., Wirth, E.D., 2002. Simultaneous diffusion MRI measurements from multiple perfused rat hippocampal slices. *Magn. Reson. Med.* 48, 565-569.
- Shepherd, T.M., Ozarslan, E., King, M.A., Mareci, T.H., Blackband, S.J., 2006a. Structural insights from high-resolution diffusion tensor imaging and tractography of the isolated rat hippocampus. *NeuroImage.* 32(4), 1499-1509.
- Shepherd, T.M., Scheffler, B., King, M.A., Stanisz, G.J., Steindler, D.A., Blackband, S.J., 2006b. MR microscopy of rat hippocampal slice cultures: A novel model for studying cellular processes and chronic perturbations to tissue microstructure. *NeuroImage.* 30(3), 780-786.
- Shepherd, T.M., Thelwall, P.E., Stanisz, G.J., Blackband, S.J., 2009. Aldehyde fixative solutions alter the water relaxation and diffusion properties of nervous tissue. *Magn. Reson. Med.* 61 <http://www3.interscience.wiley.com/cgi-bin/fulltext/122310076/HTMLSTART> last accessed 6/15/09.
- Shimizu, T., Sekine, H., Yang, J., Isoi, Y., Yamato, M., Kikuchi, A., Kobayashi, E., Okano, T., 2006. Polysurgery of cell sheet grafts overcomes diffusion limits to produce thick, vascularized myocardial tissues. *FASEB J.* 20(6), 708-710.

- Shinozaki, H., Konishi, S., 1970. Actions of several anthelmintics and insecticides on rat cortical neurons. *Brain Res.* 24, 368-371.
- Silva, A.C., Lee, J.H., Aoki, I., Koretsky, A.P., 2004. Manganese-enhanced magnetic resonance imaging (MEMRI): methodological and practical considerations. *NMR Biomed.* 17, 532-543.
- Singh, N., Pillay, V., Choonara, Y.E., 2007. Advances in the treatment of Parkinson's disease. *Prog. Neurobiol.* 81, 29-44.
- Sirotnin, Y.B., Das, A., 2009. Anticipatory haemodynamic signals in sensory cortex not predicted by local neuronal activity. *Nature.* 457(22), 475-480.
- Skolnik, J., Takacs, L., Szende, E., 1966. *In vitro* oxygen consumption of slices from kidney, brain, cortex and liver in hypoxia. *J. Cereb. Blood Flow Metab.* 209, 305.
- Stanisz, G.J., Li, J.G., Wright, G.A., Henkelman, R.M., 1998. Water dynamics in human blood via combined measurements of T_2 relaxation and diffusion in the presence of gadolinium. *Magn. Reson. Med.* 39, 223-233.
- Stanisz, G.J., Szafer, A., Wright, G.A., Henkelman, R.M., 1997. An analytical model of restricted diffusion in bovine optic nerve. *Magn. Reson. Med.* 37, 103-111.
- Stroman, P.W., Lee, A.S., Pitchers, K.K., Andrew, R.D. 2008. Magnetic resonance imaging of neuronal and glial swelling as an indicator of function in cerebral tissue slices. *Magn. Reson. Med.* 59, 700-706.
- Szafer, A., Zhong, J., Anderson, A.W., Gore, J.C., 1995a. Diffusion-weighted imaging in tissues: theoretical models. *NMR Biomed.* 8, 289-296.
- Szafer, A., Zhong, J., Gore, J.C., 1995b. Theoretical model for water diffusion in tissues. *Magn. Reson. Med.* 33, 697-712.
- Takahashi, S., Shibata, M., Fukuuchi, Y., 1997. Effects of increased extracellular potassium on influx of sodium ions in cultured rat astroglia and neurons. *Dev. Brain Res.* 104,111-117.
- Thelwall, P.E., Shepherd, T.M., Stanisz, G.J., Blackband, S.J., 2006. Effects of temperature and aldehyde fixation on tissue water diffusion properties, studied in an erythrocyte ghost tissue model. *Magn. Reson. Med.* 56(2), 282-289.
- Tilapur, U.K., König, K., Peuckert, C., Krieg, R., Halhuber, K.J., 2001. Femtosecond near-infrared laser pulses elicit generation of reactive oxygen species in mammalian cells leading to apoptosis-like death. *Exp. Cell Res.* 263, 88-97.
- Turner, M.R., Kiernan, M.C., Leigh, P.N., Talbot, K., 2009. Biomarkers in amyotrophic lateral sclerosis. *Lancet Neurol.* 8, 94-109.

- Tyszka, J.M., Fraser, S.E., Jacobs, R.E., 2005. Magnetic resonance microscopy: recent advances and applications. *Curr. Opin. Biotechnol.* 16, 93-99.
- Vafaee, M.S., Gjedde, A., 2004. Spatially dissociated flow-metabolism coupling in brain activation. *NeuroImage*. 21, 507-515.
- Vajda, Z., Pedersen, M., Doczi, T., Sulyok, E., Nielsen, S., 2004. Studies of MDX Mice. *Neurosci.* 129, 993-998.
- Vicente, J., Ramírez-Camacho, R., Trinidad, A., Ramón, G-B.J., Lobo, D., Pinilla, M., 2006. Anti-adhesive properties of polytetrafluoroethylene (Gore-Tex®) in middle ear surgery. An experimental study. *Acta Otolaryngol.* 126(2), 144-148.
- Wachowicz, K., Snyder, R.E., 2005. A continuous-flow perfusion system for the maintenance and NMR study of small tissue samples in vitro. *MAGMA*. 18, 35-40.
- Wang, J.K.T., Portbury, S., Thomas, M.B., Barney, S., Ricca, D.J., Morris, D.L., Warner, D.S., Lo, D.C., 2006. Cardiac glycosides provide neuroprotection against ischemic stroke: Discovery by a brain slice-based compound screening platform. *Proc. Natl. Acad. Sci. USA.* 103(27), 10461-10466.
- Wang, L., Yuanzong, L., Han, H., Liu, G., Osborne, P.G., 2003. Perfusate oxygen and carbon dioxide concentration influence basal microdialysate levels of striatal glucose and lactate in conscious rats. *Neurosci. Lett.* 344(2), 91-94.
- Wang, X.S., Ong, W.Y., Connor, J.R., 2002. Increase in ferric and ferrous iron in the rat hippocampus with time after kainite-induced excitotoxic injury. *Exp. Brain Res.* 143, 137-148.
- Watanabe, T., Radulovic, J., Spiess, J., Natt, O., Boretius, S., Frahm, J., Michaelis, T., 2004. In vivo 3D MRI staining of the mouse hippocampal system using intracerebral injection of MnCl₂. *NeuroImage*. 22, 860-867.
- Westbrook, C., 2005. *MRI In Practice*, 3rd ed. Blackwell Publishing, Oxford.
- Woermann, F.G., Barker, G.J., Birnie, K.D., Meencke, H.J., Duncan, J.S., 1998. Regional changes in hippocampal T₂ relaxation and volume: a quantitative magnetic resonance imaging study of hippocampal sclerosis. *J. Neurol. Neurosurg. Psychiatry.* 65, 656-664.
- Wolf, G.L., Burnett, K.R., Goldstein, E.J., Joseph, P.M., 1985. Contrast agents for magnetic resonance imaging. *Mag. Reson. Annu.* 231-266.
- Wolke, U., Jezuit, E.A., Priess, J.R., 2007. Actin-dependent cytoplasmic streaming in *C. elegans* oogenesis. *Development.* 134, 2227-2236.
- Wu, S., Suzuki, Y., Ejiri, Y., Noda, T., Bai, H., Kitada, M., Kataoka, K., Ohta, M., Chou, H., Ide, C., 2003. Bone marrow stromal cells enhance differentiation of cocultured neurosphere cells and promote regeneration of injured spinal cord. *J. Neurosci. Res.* 72, 343-351.

- Yamada, K., Gonzalez, R.G., Østergaard, L., Komili, S., Weisskoff, R.M., Rosen, B.R., Koroshetz, W.J., Nishimura, T., Sorensen, A.G., 2002. Iron-induced susceptibility effect at the globus pallidus causes underestimation of flow and volume on dynamic susceptibility contrast-enhanced MR perfusion images. *Am. J. Neuroradiol.* 23, 1022-1029.
- Yamada, M., Momoshima, S., Masutani, Y., Fujiyoshi, K., Abe, O., Nakamura, M., Aoki, S., Tamaoki, N., Okano, H., 2008. Diffusion-tensor neuronal fiber tractography and manganese-enhanced MR imaging of primate visual pathway in the common marmoset: preliminary results. *Radiology.* 249(3), 855-864.
- Yasuda, Y., Shinagawa, R., Yamada, M., Mori, T., Tateishi, N., Fujita, S., 2007. Long-lasting reactive changes observed in microglia in the striatal and substantia nigral of mice after 1-methyl-4-phenyl-1,2,3,6-tetrahydropyridine. *Brain Res.* 1138, 196-202.
- Zhong, J., Petroff, O.A., Prichard, J.W., Gore, J.C., 1993. Changes in water diffusion and relaxation properties of rat cerebellum during status epilepticus. *Magn. Reson. Med.* 30(2), 241-246.
- Zijl, P.C.M.v., Moonen, C.T.W., Faustino, P., Pekar, J., Kaplan, O., Cohen, J.S., 1991. Complete separation of intracellular and extracellular information in NMR spectra of perfused cells by diffusion-weighted spectroscopy. *Proc. Natl. Acad. Sci. USA.* 88, 3228-3232.
- Zorov, D.B., Filburn, C.R., Klotz, L.O., Zweier, J.L., Sollott, S.J., 2000. Reactive oxygen species (ROS)-induced ROS release: A new phenomenon accompanying induction of the mitochondrial permeability transition in cardiac myocytes. *J. Exp. Med.* 192(7), 1101-1104.
- Zuckermann, E.C., Glaser, G.H., 1968. Hippocampal epileptic activity induced by localized ventricular perfusion with high-potassium cerebrospinal fluid. *Exp. Neuro.* 20(1), 87-110.

BIOGRAPHICAL SKETCH

Jeremy J. Flint was born in Webster, Texas in September 1980. At the age of three, he entered the pre-kindergarten program offered by Trinity Lutheran School of Marysville, Ohio and attended classes there until graduation from second grade. After this, he transferred to the Ohio public school system entering Richard Avenue Elementary in Grove City. From third to fourth grade, he was enrolled in the districts enrichment program for academically gifted students. He attended Perry Middle School in Worthington, Ohio and, for a brief period, Coral Springs Middle School following a move to Florida. He completed high-school in 1998 after graduating from Marjory Stoneman Douglass in Parkland, Florida. It was during this period that Jeremy discovered his interest in and made the decision to commit his life to the study of medicine. He graduated summa cum laude from the University of Florida in 2002 with a bachelor's degree in cell and molecular neurobiology. His undergraduate thesis focused on the role of alpha-spectrin protein as a potential biomarker for injury severity following neurotrauma. In 2004, he entered graduate school at the University of Florida's Interdisciplinary Program in Biomedical Sciences. Since then, he has pursued studies focusing on the ways in which neural tissue structure and function can be measured at the cellular level using magnetic resonance microscopy. He received his Ph.D. from the University of Florida in the summer of 2009.